KEK Proceedings 95-9
November 1995
R/D

Proceedings of the Fifth EGS4 Users' Meeting in Japan

July 23 - 25, 1995.

KEK, Tsukuba, Japan

Edited by

H. Hirayama, Y. Namito and S. Ban

NATIONAL LABORATORY FOR
HIGH ENERGY PHYSICS

National Laboratory for High Energy Physics, 1995

KEK Reports are available from:

Technical Information & Library
National Laboratory for High Energy Physics
1-1 Oho, Tsukuba-shi
Ibaraki-ken, 305
JAPAN

Phone: 0298-64-1171
Telex: 3652-534 (Domestic)
(0)3652-534 (International)
Fax: 0298-64-4604
Cable: KEK OHO
E-mail: LIBRARY@JPNKEKVX (Bitnet Address)
library@kekvax.kek.jp (Internet Address)

FOREWARD

The Fifth EGS4 Users' Meeting in Japan was held at the National Laboratory for High Energy Physics (KEK) from July 23 to 25. The meeting has been hosted by the Radiation Safety Control Center, KEK. Nearly 100 participants attended the meeting.

The meeting was divided into two parts. Lectures concerning the EGS4 System, Mortran, User code, HOWFAR, how to use PEGS4, how to write source routine and the EGS4 shower display system on PC were given at the first half. Practices to install the EGS4 system on the UNIX workstation or PC and to run PEGS4 or user code were also performed. In the later half, 15 talks related EGS4 were presented. The talks covered the wide fields, like the medical application and the calculation of various detector response etc. These talks were very useful to exchange the information between the researchers in the different fields.

Finally, we would like to express our great appreciation to all authors who have prepared manuscript quickly for the publication of this proceedings.

Hideo Hirayama
Yoshihito Namito
Syuichi Ban
Radiation Safety Control Center
KEK, National Laboratory for High Energy Physics

CONTENTS

CALCULATIONS OF ENERGY DEPOSITION BY LOW ENERGY ELECTRON BEAMS

N. NARIYAMA

Ship Research Institute
6-38-1, Shinkawa, Mitaka, Tokyo 181, JAPAN

Abstract

In the EGS4 code, too small or large step sizes violate the limits of the electron multiple scattering theory used. The limits are stricter with decreasing the electron energy so that the relation of the step size and the multiple scattering theory in the low energy region was examined with PRESTA. Energy deposition in water irradiated by electron beams of 30 to 200 keV was calculated. The parameters chosen to change the step sizes were the geometric mesh width, ESTEPE, and AE. Too small mesh width and ESTEPE turned off the multiple scattering simulation, which resulted in widely different curves from those with the full simulation of the multiple scattering. For large AE, the energy deposition obtained became zero at the shallower depth than the electron range since the energy straggling for the electrons of the energy below 2AE is not considered in the EGS4.

1. Introduction

At the third EGS4 user's meeting, interface doses irradiated with low energy photons were discussed[1]. Under such a condition that electron equilibrium does not exist, the validity of electron transport calculations becomes important even for the photon irradiation. The EGS code was originally developed for high energy electron and photon transport, followed by the addition of the algorithm of ESTEPE[2] and PRESTA[3] to establish the validity for low energy electron transport. The PRESTA algorithm decreased the task of users by removing the ESTEPE dependence of the calculation, but it does not change the condensed history technique itself that a step size is used for the electron multiple scattering simulation. In the treatment, too small step sizes cannot be applied owing to the violation of the limits of the multiple scattering theory used in the EGS4, which become stricter with decreasing the electron energy[3]. In the study, hence, the relation of the step size and the multiple scattering the ory was examined using PRESTA by calculating energy deposition by low energy electron beams. The parameters chosen to change the

step sizes were the geometric mesh width, ESTEPE, and AE.

2. Calculation Methods and Results

The energy deposition distributions in one-dimensional slabs irradiated by the electron beams of 30 keV to 200 keV were calculated with PRESTA. The slabs are 1.5 times thicker than the electron ranges, which are divided into 75 meshes for the energy scoring. Materials of the slabs were water, aluminum, and copper. In PRESTA, the default ESTEPE was used. The values of AE and ECUT used were 1 keV and 10 keV, respectively. Figures 1 to 3 show the results of the calculations. For aluminum and copper, the positions of the peaks agree with each other for all the energies, respectively, and the curves change gradually with the energy. For water, however, the curve for 30 keV is much different from those of the other energies in that the energies deposited at the shallow depths are smaller than those for 40 keV and the peak is situated deeper at the 0.52 electron ranges.

3. Discussion

The Molière multiple scattering theory is valid under the conditions that the scattering angles are not large and the scattering numbers in the step are more than 20 or the natural logarithm e[3]. With decreasing the electron energy, the upper limit becomes smaller because of the larger scattering angles. On the other hand, for low-Z material, the number of the scattering in the step is less so that the lower limit becomes larger. In this context, it is assumed that too short steps turned off the multiple scattering and produced the curve in Fig. 1. To confirm the assumption, the same calculation was made for 30 meshes which make the step sizes used larger. Figure 4 shows the result. The peak of the curve calculated is situated at the same position as those for the other energies. Using NOSCAT in COMMON/MISC/, the percentage of the counts of the multiple scattering skipped was calculated for 75 and 30 meshes. The results showed that the 32% multiple scattering was skipped for 75 meshes and 6 % for 30 meshes, which confirmed the assumption described above.

The use of ESTEPE is assumed to produce the same effect as the geometric mesh width since it also change the step sizes. Then, with the default EGS4, the energy deposition for 75 meshes was calculated for ESTEPE=0.8%, 2%, and default. As shown in Fig. 5, the same curve as that in Fig. 1 was obtained for ESTEPE=0.8%. The percentage of the multiple scattering skipped was 37% for ESTEPE=0.8% and 9% for ESTEPE=2%, which reconfirmed that the curve in Fig. 1 was produced owing to the skip of the multiple scattering by the short steps. In the figures, the total number of the multiple scattering for ESTEPE=2% is 1.5 times more than that for PRESTA , while the number of multiple scattering skipped is less. The contradiction was caused because the different lower limits

of the number of the multiple scattering are set in PRESTA and the default EGS4; the former is e and the latter unity.

In the EGS4, the inelastic interactions of electrons are treated as discrete when the secondary electrons have the energies over AE, and as continuous when below AE. Hence the electron mean free path depends on AE, that is, the electron step length depends on AE. To confirm the effect, the energy deposition in water was calculated for 30 meshes on the condition of AE=10 keV. As shown in Fig. 6, the calculated curve for AE=10 keV exceeds that for AE=1 keV from the depth of the 0.4 electron ranges and goes down to zero at the depth of the 0.8 electron ranges without energy straggling, which showed the widely different tendency from the curve for AE=1 keV. The values of NOSCAT, however, showed that the skipped multiple scattering for AE=10 keV was less. In the EGS4 code, the energy-loss straggling is neglected in the continuous interactions, while simulated with the random nature of the energy loss in the discrete interactions. As a result, the electrons of the energies below 2AE have only the continuous interaction since those can produce no secondary electrons of the energies over AE. Therefore, the effects are assumed to reveal themselves for 30 keV at the depth where the electrons of the energies below 2AE are dominant, which was verified by the additional spectrum calculation. The assumption is also supported by the results that AE dependence decreases with increasing the incident energies as shown in Fig. 6.

4. Conclusions

It was proved that appropriate mesh widths and AE needed setting for the low energy electron transport even with PRESTA. As also mentioned by Rogers[2], each user needs to monitor such a parameter as NOSCAT and diagnose the condition of the executed program. Another Monte Carlo code for electron and photon transport, ITS[5], does not produce the same influence described above. Figure 7 shows the calculated energy deposition in water for 75 meshes, which agreed with those for 30 meshes with PRESTA. This is because the ITS code was originally developed for low energy electron transport so that subregions can be used besides the ordinary regions for the energy scoring, which eliminate the effect on the electron step lengths. The multiple scattering theory used can be applied for large angle scattering and small size steps. Moreover, the energy straggling is applied independent of the electron cutoff energies because the energy losses are sampled using Landau fluctuation. In the case where low energy electron transport is important, comparison with ITS code is considered an option for greater reliability of the calculations.

References

[1] N. Nariyama, et al., *The influence of interface effect on the photon absorbed dose measurements with TLDs*, KEK Proceedings, 93-15, 62-67 (1993) (in Japanese).

[2] D. W .O. Rogers, *Low energy electron transport with EGS4*, Nucl. Instru. Meth., **227**, 535-548 (1984).

[3] A .F. Bielajew and D. W. O. Rogers, *PRESTA: the parameter reduced electron-step transport algorithm for electron Monte Carlo transport*, Nucl. Instru. Meth., **B18**, 165-181 (1987).

[4] International Commission on Radiation Units and Measurements, *Stopping powers for electrons and positrons*, ICRU Report 37 (1984).

[5] J. A. Halbleib, et al., *ITS Version 3.0: the integrated TIGER series of coupled electron/photon Monte Carlo transport codes*, SAND91-1634 (1992).

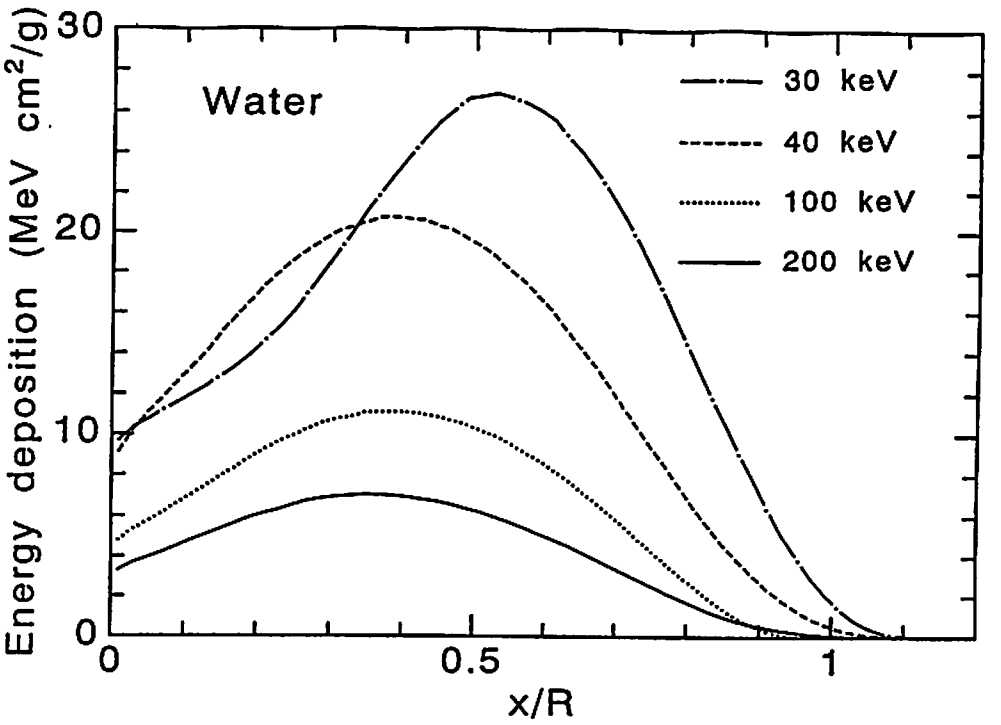

Fig. 1 Energy deposition in water

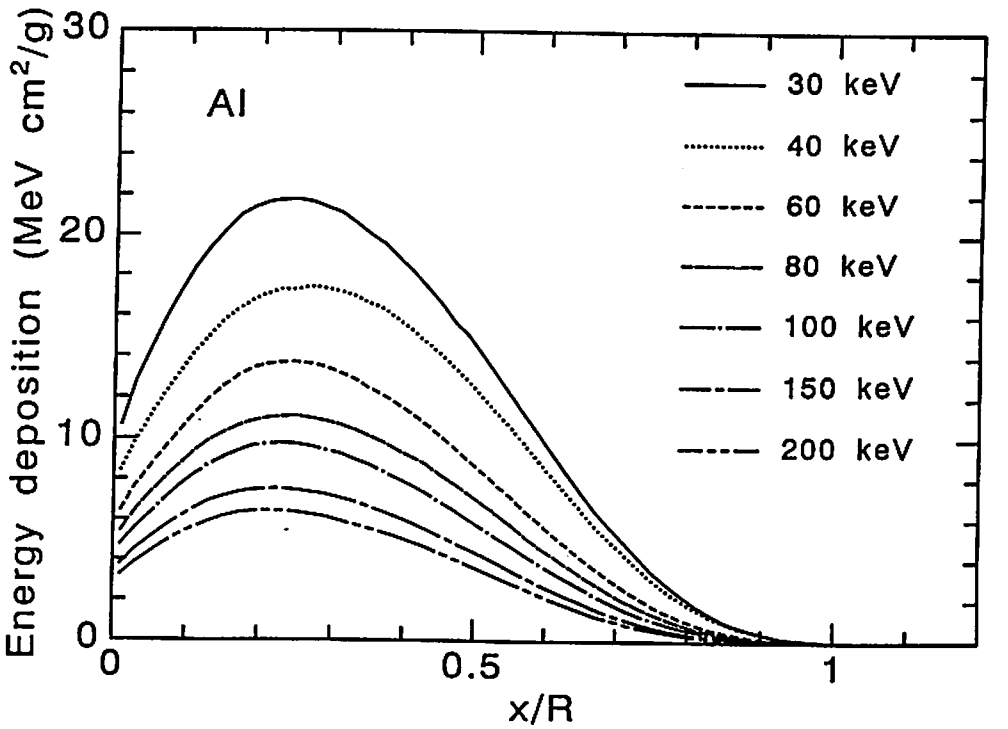

Fig. 2 Energy deposition in aluminum

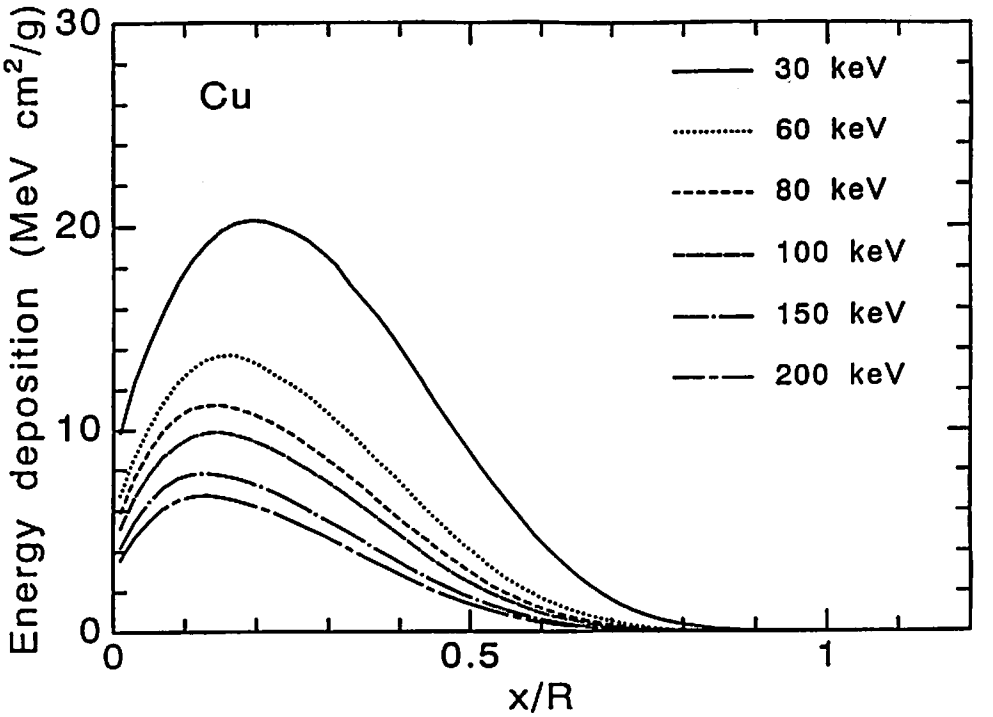

Fig. 3 Energy deposition in copper

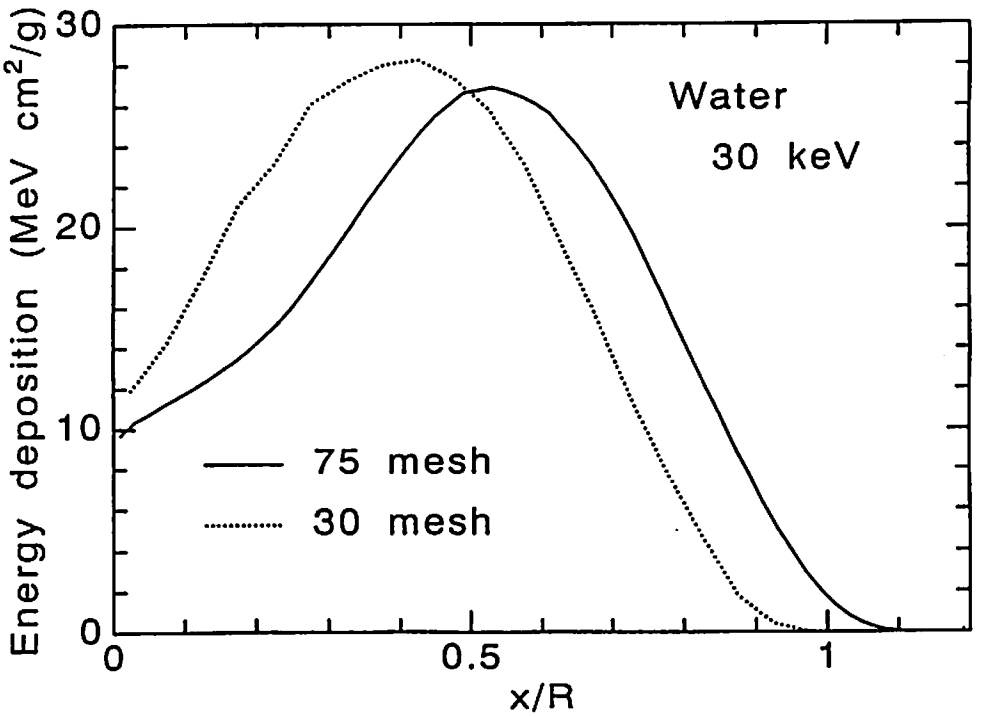

Fig. 4 Dependence of energy deposition in water on the mesh width

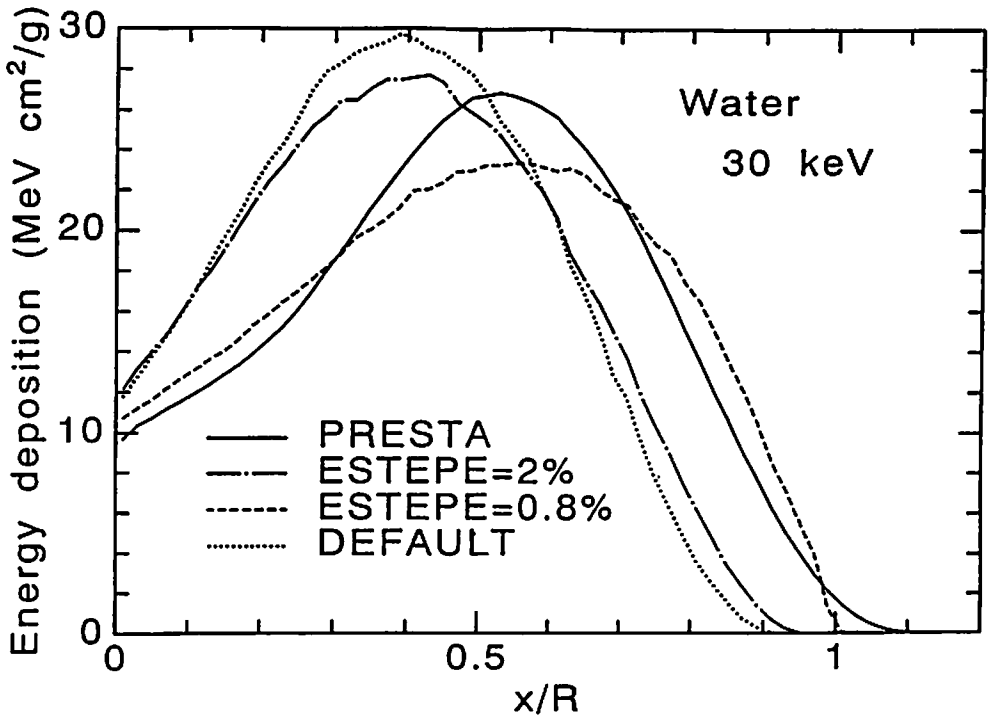

Fig. 5 Dependence of energy deposition in water on ESTEPE

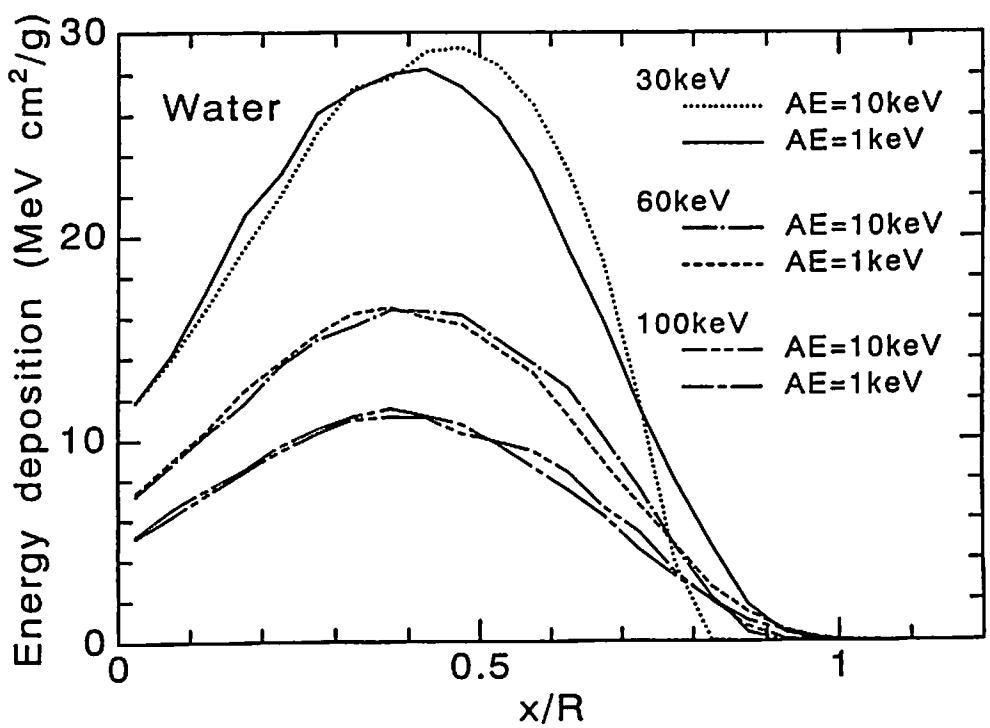

Fig. 6 Dependence of energy deposition in water on AE

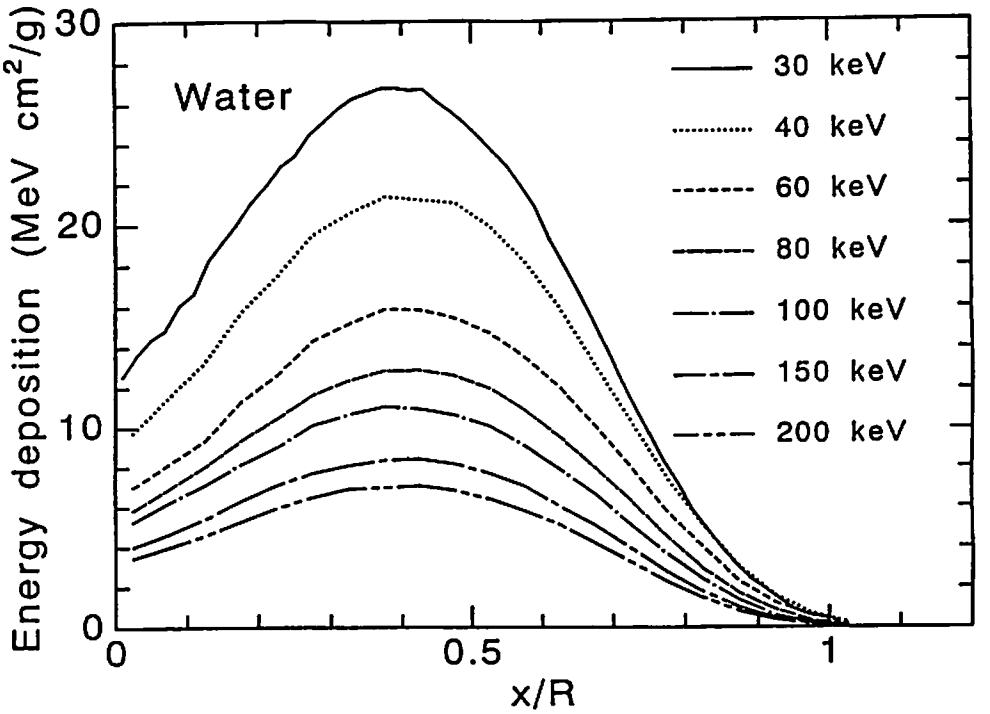

Fig. 7 Energy deposition in water calculated with ITS

APPLICATION OF ADJOINT MODE TO SHIELDING ANALYSIS WITH MONTE CARLO METHOD

K. UEKI

Ship Research Institute
6-38-1 Shinkawa, Mitaka, Tokyo 181, JAPAN

1. Introduction

Today, multi-group Monte Carlo code MORSE-CG and continuous energy Monte Carlo code MCNP-4A are used extensively. Both the codes have the adjoint mode functions, adjoint mode calculation is available only with multi-group constants in the MCNP-4A. However, the adjoint mode is few applied to the shielding analysis.

In the adjoint mode calculation, the source is the response function and the response is the source of the forward mode. Accordingly, the adjoint mode is good at the large source geometry and the plural source problems. Furthermore, the treatment of the scattering is the up-scattering, so that the energy spectrum obtained by the adjoint mode has good accuracy in the high energy region. Otherwise, adjoint flux is indispensable in the sensitivity analysis and the flux is available as an importance function of a forward mode calculation to reduce the variance of the Monte Carlo.

Even in the continuous Monte Carlo code MCNP-4A, the adjoint mode calculation is limited to the multi-group, the Boltzmann transport equation is described by the multi-group in this paper.

2. Multi-group Boltzmann Transport Equation

2.1 Multi-group Transport Equation for Forward Mode

The time-independent integral emergent particle density equation is written as[1]

$$X_g(\bar{r},\bar{\Omega}) = S_g(\bar{r},\bar{\Omega}) + \sum_{g'} \int d\bar{\Omega}' \frac{\Sigma_s^{g'\to g}(\bar{r},\bar{\Omega}'\to\bar{\Omega})}{\Sigma_t^{g'}(\bar{r})} \times \int dR \Omega_t^{g'}(\bar{r}) e^{-\beta_{g'}(\bar{r},R,\bar{\Omega})} X_{g'}(\bar{r}',\bar{\Omega}'). \quad (1)$$

where, $S_g(\bar{r},\bar{\Omega})$ = Distribution of source particles for g − th group

$\beta_{g'}(\bar{r},R,\bar{\Omega})$ = Optical thickness

$\Sigma_t^g(\bar{r})$ = Energy averaged total cross section for g − th group (cm^{-1})

$\Sigma_s^{g'\to g}(\bar{r},\bar{\Omega}'\to\bar{\Omega})$ = Group g′ to g scattering cross section (cm^{-1} st^{-1})

$X_{g'}(\bar{r}',\bar{\Omega}')$ = Density of particles leaving a source or emerging from a real collision with phase space coordinates (group g,$\bar{r},\bar{\Omega}$).

2.2 Multi-group Transport Equation for Adjoint Mode

The integral point-value equation modified by defining the direction $\hat{\Omega} = -\bar{\Omega}$ and considering the change in phase space coordinates in the reverse sense is written as [2]

$$X_g^*(\bar{r},\hat{\Omega}) = P_g^*(\bar{r},\hat{\Omega}) + \int dR\Sigma_t^g(\bar{r})e^{-\beta_g(\bar{r},R,\hat{\Omega})}\left[\frac{\Sigma_t^g(\bar{r}')}{\Sigma_t^g(\bar{r})}\right]\times \left[\sum_{g'}\int d\bar{\Omega}'\frac{\Sigma_s^{g\to g'}(\bar{r}',\hat{\Omega}\to\hat{\Omega}')}{\Sigma_t^{g(\bar{r}')}}\right]X_{g'}^*(\bar{r}',\hat{\Omega}'). \quad (2)$$

where, $X_g^*(\bar{r},\hat{\Omega})$ = Point value, corresponding to $X_g(\bar{r},\bar{\Omega})$ in forward mode,

$P_g^*(\bar{r},\hat{\Omega})$ = Response function of effect of interest due to a particle which emerges from a collision having phase space coordinates (group g,$\hat{\Omega}$).

In order to solve the adjoint mode equation (2) by the same logic of the forward mode, some substitutions are required.

1. Arrangement of the scattering matrix is altered :
   from $\Sigma_s^{g'\to g}(\bar{r},\bar{\Omega}'\to\bar{\Omega})$ to $\Sigma_s^{g\to g'}(\bar{r},\hat{\Omega}\to\hat{\Omega}')$.
2. Source term $S_g(\bar{r},\bar{\Omega})$ is altered to response function $P_g^*(\bar{r},\hat{\Omega})$.
3. Effect of interest λ (flux, dose equivalent rate, reaction rate, etc.) is as follows:
   (a) Forward Mode

$$\lambda = \sum_g \int\int P_g(\bar{r},\bar{\Omega})X_g(\bar{r},\bar{\Omega})d\bar{r}d\bar{\Omega} \quad (3)$$

   where, $P_g(\bar{r},\bar{\Omega})$=Response function.

   (b) Adjoint Mode

$$\lambda = \sum_g \int\int S_g(\bar{r},\bar{\Omega})X_g^*(\bar{r},\hat{\Omega})d\hat{r}d\hat{\Omega} \quad (4)$$

So as to correspond the result of the adjoint mode to the forward mode, following normalization factor F is multiplied to the adjoint mode.

$$F = \sum_g \int \int P_g(\bar{r}, \bar{\Omega}) d\bar{r} d\bar{\Omega} \tag{5}$$

3. Example 1

A simple example is shown in Fig. 1[3]. Source particles of 3 energy groups incident vertically in the slab of 2-cm-thick. The scattering direction is forward ($\cos\theta = 1$), and the particles are detected on the opposite side surface. Table 1 indicates source energy distribution, response function, macroscopic total cross sections, non-absorption probability rate and probability distribution. In the forward mode, energy group g=1 is the highest ; on the contrary, g=3 is the highest in the adjoint mode. The track-length l is calculated with the random number ξ

$$l = -\frac{1}{\Sigma_t^g} l_n \xi \tag{6}$$

Table 2-(a) and Table 2-(b) are the results of Fig.1 by hand calculation in forward and adjoint mode, respectively.

4. Example 2

Another example problem is shown Fig.2. This problem is a neutron penetration through a water cylinder. Neutrons are emitted from the disk on the bottom surface of the cylinder and a point detector is located in front of the cylinder.

This problem is analyzed by the forward and the adjoint mode of the MCNP 4A. The input date mainly on the source term of the forward mode is indicated in Table 3 ; adjoint mode is in Table 4. The difference of the input data between the forward and the adjoint mode is as follows.

1. Source term of the adjoint mode, sp1 in Table 4, is the response function of the forward mode.

2. Response function of the adjoint mode, em0 in table 4, is the neutron source spectrum of the forward mode.

3. In this calculation, source neutrons are emitted to the forward direction (2π(st)) in each mode. Accordingly, there is no correct on the direction. However, it has to consider the source emitting direction, in general.

4. Normalization factor F in Eq.(5) to this problem is ;

$$
\begin{aligned}
F &= \frac{\text{Forward ModeEnergy Density}}{\text{Adjoint Mode Energy Density}} \times \frac{\text{Forward Mode Energy Response}}{\text{Adjoint Mode Energy Response}} \times \\
&\quad \frac{\text{Forward Mode Direction Density}}{\text{Adjoint Mode Direction Density}} \times \frac{\text{Forward Mode Direction Response}}{\text{Adjoint Mode Direction Response}} \\
&= \frac{\sum^{P_g} P_g}{\sum^{R_{g'}} R_{g'}} \times \frac{R_{g'}}{P_g} \times \frac{\frac{1}{2\pi}}{\frac{1}{2\pi}} \times \frac{1}{1} \\
&= \frac{\sum \mathrm{em0}_g}{\sum \mathrm{sp1}_g} \times 1 = 30.0 = \mathrm{wgh} \text{ in the adjoint mode}
\end{aligned}
$$

5. In the forward mode, the detector is the point, so that the point detector tally is used in the MCNP 4A code. On the other hand, the detector is the surface, the surface crossing tally is employed in the adjoint mode.

In the forward mode calculation, the energy flux is indicated in each "tally ○○" part of the MCNP 4A output. on the other hand, the energy flux is shown in the "total" part of each "tally ○○" part. Table 5 shows the comparison of MCNP 4A calculated energy flux between the forward and the adjoint mode. The total fluence of the forward and the adjoint mode is 1.6678×10^{-4} (n /source neutron) (fsd : 0.0189) and 1.7168×10^{-4} (n /source neutron) (fsd : 0.0397), respectively. Both the results are indicated good agreement with in each fsd. The fsd (fractional standard deviation) of the forward mode is better than that of the adjoint mode by a factor of 2. However, the discrepancy is almost due to the thermal neutrons. Thermal neutrons are not so contribute to the dose equivalent rate and the most of reaction rates, and it is clear that the fsd's of the high energy fluxes are much better than that of the forward mode. This reason is that the neutrons are down-scattering in the forward mode and up-scattering in the adjoint mode. Accordingly, it is expected to obtain the desired Monte Carlo results to take those characteristics of each mode.

References

[1] M. B. Emmett, *The MORSE Monte Carlo Radiation Transport Code System*, ORNL -4972, Oak Ridge National Laboratory (1975).

[2] J. F. Briesmeister, Ed., MCNP-A General Monte Carlo N-Particle Transport Code, Version 4A, Los Alamos National Laboratory report, LA-12625 (1993).

[3] K. Ueki, *Correspondence between Adjoint Monte Carlo Method and Forward Monte Carlo Method,* J. Atomic Ener. Soc. Japan, **20**, 509(1978), in Japanese.

Table 1. Calculating conditions for forward and adjoint mode in Fig 1.

Forward Mode	Adjoint Mode
$S_g = \begin{pmatrix} S_1 \\ S_2 \\ S_3 \end{pmatrix} = \begin{pmatrix} 0.3 \\ 0.7 \\ 0 \end{pmatrix}$	$\dot{S}_{g'} = \begin{pmatrix} \dot{S}_1 \\ \dot{S}_2 \\ \dot{S}_3 \end{pmatrix} = R_{g'} = \begin{pmatrix} R_3 \\ R_2 \\ R_1 \end{pmatrix} = \begin{pmatrix} 3.0 \\ 2.0 \\ 1.0 \end{pmatrix}$
$R_g = \begin{pmatrix} R_1 \\ R_2 \\ R_3 \end{pmatrix} = \begin{pmatrix} 1.0 \\ 2.0 \\ 3.0 \end{pmatrix}$	$\dot{R}_{g'} = \begin{pmatrix} \dot{R}_1 \\ \dot{R}_2 \\ \dot{R}_3 \end{pmatrix} = S_{g'} = \begin{pmatrix} S_3 \\ S_2 \\ S_1 \end{pmatrix} = \begin{pmatrix} 0 \\ 0.3 \\ 0.7 \end{pmatrix}$
$\sum_t^g = \begin{pmatrix} \sum_t^1 \\ \sum_t^2 \\ \sum_t^3 \end{pmatrix} = \begin{pmatrix} 1.0 \\ 1.0 \\ 2.0 \end{pmatrix}$	$\dot{\sum}_t^{g'} = \begin{pmatrix} \sum_t^3 \\ \sum_t^2 \\ \sum_t^1 \end{pmatrix} = \begin{pmatrix} 2.0 \\ 1.0 \\ 1.0 \end{pmatrix}$
$\sum_s^{g' \to g} = \begin{pmatrix} \sum_s^{1\to1} & \sum_s^{1\to2} & \sum_s^{1\to3} \\ 0 & \sum_s^{2\to2} & \sum_s^{2\to3} \\ 0 & 0 & \sum_s^{3\to3} \end{pmatrix} = \begin{pmatrix} 0.5 & 0.2 & 0.2 \\ 0 & 0.2 & 0.3 \\ 0 & 0 & 1.0 \end{pmatrix}$	$\dot{\sum}_s^{g \to g'} = \begin{pmatrix} \sum_s^{3\to3} & \sum_s^{2\to3} & \sum_s^{1\to3} \\ 0 & \sum^{2\to2} & \sum^{1\to2} \\ 0 & 0 & \sum^{1\to1} \end{pmatrix} = \begin{pmatrix} 1.0 & 0.3 & 0.2 \\ 0 & 0.2 & 0.2 \\ 0 & 0 & 0.5 \end{pmatrix}$
$P_{n-ab} = \begin{pmatrix} P_{n-ab}^1 \\ P_{n-ab}^2 \\ P_{n-ab}^3 \end{pmatrix} = \begin{pmatrix} 0.9 \\ 0.5 \\ 0.5 \end{pmatrix}$	$\dot{P}_{n-ab} = \begin{pmatrix} \dot{P}_{n-ab}^3 \\ \dot{P}_{n-ab}^2 \\ \dot{P}_{n-ab}^1 \end{pmatrix} = \begin{pmatrix} 0.75 \\ 0.4 \\ 0.5 \end{pmatrix}$
$P_r^{g \to g'} = \begin{pmatrix} P_r^{1\to1} & P_r^{1\to2} & P_r^{1\to3} \\ 0 & P_r^{2\to2} & P_r^{2\to3} \\ 0 & 0 & P_r^{3\to3} \end{pmatrix} = \begin{pmatrix} 5/9 & 2/9 & 2/9 \\ 0 & 0.4 & 0.6 \\ 0 & 0 & 1.0 \end{pmatrix}$	$\dot{P}_r^{g' \to g} = \begin{pmatrix} P_r^{3\to3} & P_r^{2\to3} & P_r^{1\to3} \\ 0 & P_r^{2\to2} & P_r^{1\to2} \\ 0 & 0 & P_r^{1\to1} \end{pmatrix} = \begin{pmatrix} 2/3 & 1/5 & 2/5 \\ 0 & 0.5 & 0.5 \\ 0 & 0 & 1.0 \end{pmatrix}$

Table 2-(a). Forward mode

Particle Number	Group	Initial Weight	g→g' (Last Group)	Range (≧2cm)	Weight (Last Weight)	Rg'	λ g
1	1	1.0	1→1	0.65	0.9		
			1→3	1.22	0.9		
			3→③	0.15 (≧2)	0.5 (0.405)	3	1.215
2	1	1.0	1→2	0.79	0.9		
			2→2	0.22	0.5		
			2→3	0.86	0.5		
			3→③	0.16 (≧2)	0.5 (0.1125)	3	0.3375
3	1	1.0	1→①	2.58 (≧2)	0.9 (0.9)	1	0.9
4	2	1.0	2→3	1.75	0.5		
			3→③	0.42 (≧2)	0.5 (0.25)	3	0.75
5	2	1.0	2→③	2.56 (≧2)	0.5 (0.5)	3	1.5
6	2	1.0	2→3	0.23	0.5		
			3→3	0.24	0.5		
			3→3	1.49	0.5		
			3→③	0.03 (≧2)	0.5 (0.0625)	3	0.1875
7	2	1.0	2→3	0.26	0.5		
			3→3	1.08	0.5		
			3→③	0.84 (≧2)	0.5 (0.125)	3	0.3375
8	2	1.0	2→2	0.66	0.5		
			2→3	0.86	0.5		
			3→③	0.53 (≧2)	0.5 (0.125)	3	0.3375
9	2	1.0	2→3	0.11	0.5		
			3→3	0.50	0.5		
			3→3	1.02	0.5		
			3→3	0.21	0.5		
			3→③	0.42 (≧2)	0.5 (0.03125)	3	0.09375
10	2	1.0	2→2	0.81	0.5		
			2→②	1.58 (≧2)	0.5 (0.25)	2	0.50
					$\sum_g \lambda_g$ = 6.159		
					λ = 6.159 / 10 = 0.616		

Table 2-(b). Adjoint mode

Particle Number	Group	Initial Weight	g→g' (Last) (Group)	Range (≧2cm)	Weight (Last) (Weight)	R_g^*	Normalization F	λ_g^*
1	1	1.0	1→2	0.11	0.75			
			2→3	0.84	0.4			
			3→3	0.75	0.5			
			3→③	0.95 (≧2)	0.5 (0.075)	0.3	6	1.135
2	1	1.0	1→1	0.24	0.75			
			1→1	0.05	0.75			
			1→1	0.09	0.75			
			1→②	2.86 (≧2)	0.75 (0.3164)	0.7	6	1.329
3	1	1.0	1→1	0.865	0.75			
			1→1	0.23	0.75			
			1→1	0.36	0.75			
			1→②	0.62 (≧2)	0.75 (0.3164)	0.7	6	1.329
4	1	1.0	1→1	0.36	0.75			
			1→3	0.04	0.75			
			3→3	0.20	0.5			
			3→③	1.69 (≧2)	0.5 (0.1406)	0.3	6	0.253
5	1	1.0	1→3	0.54	0.75			
			3→3	0.86	0.5			
			3→3	0.19	0.5			
			3→③	1.01 (≧2)	0.5 (0.09375)	0.3	6	0.169
6	1	1.0	1→1	1.10	0.75			
			1→3	0.45	0.5			
			3→③	1.51 (≧2)	0.5 (0.1875)	0.3	6	0.3375
7	2	1.0	2→3	1.78	0.4			
			3→③	3.41 (≧2)	0.5 (0.2)	0.3	6	0.36
8	2	1.0	2→③	2.70 (≧2)	0.4 (0.5)	0.3	6	0.72
9	2	1.0	2→3	0.34	0.4			
			3→③	4.96 (≧2)	0.5 (0.2)	0.3	6	0.36
10	2	1.0	2→②	3.17 (≧2)	0.4	0.7	6	1.68

11	3	1.0	3→3	0.90	0.5			
			3→③	1.65 (≧2)	0.5 (0.25)	0.3	6	0.45
12	3	1.0	3→3	0.23	0.5			
			3→3	0.88	0.5			
			3→3	0.27	0.5			
			3→3	0.54	0.5			
			3→③	1.01	0.5 (0.03125)	0.3	6	0.056
					$\sum_{g'} \lambda_{g'} = 7.1785$			
					$\dot{\lambda} = 7.1785 / 12 = 0.598$			

EGS4 BENCHMARK PROGRAM

Y. YASU, H. HIRAYAMA, Y. NAMITO and S. YASHIRO

KEK, Oho 1-1, Tsukuba 305, Japan

Abstract

This paper proposes EGS4 Benchmark Suite which consists of three programs called UCSAMPL4, UCSAMPL4I and XYZDOS. This paper also evaluates optimization methods of recent RISC/UNIX systems, such as IBM, HP, DEC, Hitachi and Fujitsu, for the benchmark suite. When particular compiler option and math library were included in the evaluation process, system performed significantly better. Observed performance of some of the RISC/UNIX systems were beyond some so-called Mainframes of IBM, Hitachi or Fujitsu. The computer performance of EGS4 Code System on an HP9000/735 (99MHz) was defined to be the unit of EGS4 Unit. The EGS4 Benchmark Suite also run on various PCs such as Pentiums, i486 and DEC alpha and so forth. The performance of recent fast PCs reaches that of recent RISC/UNIX systems. The benchmark programs have been evaluated with correlation of industry benchmark programs, namely, SPECmark.

1. Introduction

We pointed out that SPECmark and High Energy Physics benchmark programs such as CERN Benchmark Suite & SSC Benchmark Suite could not be a good evaluation standard for a computer performance of the EGS4 Code System[1,2]. Therefore, we propose to use the EGS4 Benchmark Suite we developed. UCSAMPL4 program is one in the suite. The program is included in the distribution kit of the EGS4 Code System. An incident particle is an electron of 1 GeV energy and the particle penetrates into an iron wall of 3 cm thickness. UCSAMPL4I program has the same incident particle as in the UCSAMPL4, but the penetrated material is an infinitely thick iron. This means all the incident energy will be deposited in the iron. The program was developed by us. The XYZDOS program was developed by A.F.Bielajew at NRCC[3]. The incident particle is an electron that has 20 MeV energy and the medium is water in a form of a 19 cm cube. The "BENCHE" program in the XYZDOS has run. The history numbers of UCSAMPL4, UCSAMPL4I and XYZDOS are 10000, 10000 and 100000, respectively.

The sizes of instruction codes in the three programs are approximately a few hundred KB, but the data sizes are not the same. The data size of UCSAMPL4 and UCSAMP4I are several hundred KB, but that of XYZDOS is over 1 MB. We analyzed the benchmark programs by using analysis tools of "prof" and/or "pixie" and found that there was no hot spot in the benchmark program codes. Hot spot means a local section of program codes that consumes significant portion of CPU time. Execution time for arithmetic functions such as "SQRT" and "LOG" occupied approximately 10 execution time, but the ratio of the occupancy depended on which CPU architecture and which Operating System with FORTRAN compiler were selected.

We have evaluated a correlation between the incident energy and the execution time of the benchmark programs in Fig. 1. The energy was varied between 200 MeV and 8 GeV. The execution time of UCSAMPL4 was not linear to the incident energy, but that of UCSAMPL4I was linear to the incident energy. On UCSAMPL4I, all the incident energy was deposited into the medium, but all the energy on UCSAMPL4 was not. This means that the execution time of EGS4 Code System is linear to the incident energy if the ratio of the energy deposition and the total energy is kept constant.

CPU time is a measure of computer performance and we will measure this CPU time for EGS4 Code System here. The CPU time is different from an "elapsed time". The elapsed time depends on the other workload because multiple processes on single CPU with a time-sharing operation share the CPU time. The used system function for measuring the CPU time is either "times" function in library of C Language or "etime" function in library of FORTRAN Language. Those functions are usually used for measuring CPU time.

When the benchmark program run several times on a computer, the measured CPU time varied. Fig. 2 shows the distribution of the execution time of UCSAMPL4. The fluctuation reaches up to 10 % of the average execution time. We think that the fluctuation was due to other workload with I/O. The CPU time should not depend on other workload, but we have no way to measure the CPU time without those system functions. Therefore, we have carefully measured CPU time with as low workload as possible to minimize the fluctuation on the measurement. The "execution time" used in the followings is equivalent to the CPU time.

2. Optimization Method on RISC/UNIX Systems for EGS4 Code System

In order to improve the performance of the systems, we decided not to modify the source code of the benchmark program because there was no hot spot and many modifications of the code might change physics results. Instead, we chose the best compiler option of FORTRAN and selected math library. The specifications of computers used for the evaluation are listed in Table 1.

First, we discuss the results from two IBM computers (model 590 and 390). Both CPUs had identical POWER2 architecture, but the cache size and the memory bandwidth were different. The results are shown in Fig. 3. Both computers have almost the same execution time on the benchmark programs. We should investigate the reason why both computers had the same performance with the EGS4 benchmark program although the model 590 had larger size of the cache and higher memory bandwidth than the model 390 (CERN SP). The compiler option "Opt6" in the Fig. 3 is listed in Table 2. The math library of IBM Austin Lab. was effective in shortening the execution time.

The results from HP computers are shown in Fig. 4. Latest HP model J210 computer and the fastest version of HP model 735 were used for the evaluation. In the figures, the model J210 and the model 735 were named as PA7200-120 and PA7150-125 respectively. The execution time with compiler option "Opt5" was the best. The option requires two execution cycles of the program to run beforehand. This means that the first execution of the EGS4 benchmark program makes the profile of the execution. Then, the second compilation makes best optimization code by using the execution profile. This option makes best performance, but the compiler option in Table 2 were used instead for the evaluation. It is because the compiler option in the Table 2 is more likely to be used and is almost as fast.

DEC computers used in this test were AlphaSever 8400 5/300 and AlphaStation 200/233. The Server has the best performance in all of the computers evaluated with the EGS4 benchmark programs. Fig. 5 shows the results. The compiler option "Opt0" means the option "-O0" and the "Opt1" means the default optimization " -O", which corresponds to "-O4". The best options are listed in Table 2. The option "- non_shared" was effective and "math_library fast" flag was useful in some cases. In case of the XYZDOS, the "math_library fast" flag made the physics result change.

A Hitachi workstation 3500/540 is similar to an HP workstation because both uses the same PA-RISCs for its CPU. But, the performance are not the same because the memory/bus architecture and the Operating System/ FORTRAN compiler are different. The default optimization "O3" flag was effective in executing the UCSAMPL4 and the XYZDOS programs while the best optimization flag "s" is effective on the UCSAMPL4I. Fig. 6 shows results on the Hitachi workstation. The default optimization yields excellent performance.

A Fujitsu workstation had SuperSPARC(60 MHz). Fig. 7 shows the results from the Fujitsu workstation. The four types of the optimizations were always effective on the

benchmark programs. The compiler option for the best performance is listed in Table 2.

3. EGS4 UNIT

We have chosen the HP9000/735(99MHz) as the standard computer for evaluating EGS4 benchmark programs. The geometry used with the UCSAMPL4I is very simple while that with the XYZDOS is complicated. These programs represent typical programs of an EGS4 Code System. The execution times of the UCSAMPL4I and of the XYZDOS were measured. The UCSAMPL4I and the XYZDOS took 30.1 sec and 301 sec respectively. The geometric mean of both execution times was used as a normalization value. In contrast to an arithmetic mean, the geometric mean is consistent regardless of the computer used for the reference. Defining the EGS4 Unit of HP9000/735 (99MHz) to be 1, a computer with larger value of the EGS4 Unit will have better performance.

Fig. 8 shows the EGS4 Unit of all computers evaluated (including PCs). The EGS4 Unit does not include the evaluation of the UCSAMPL4. It is convenient for a user of the EGS4 Code System to know the correlation between a EGS4 Unit and corresponding execution time of the UCSAMPL4 since the program is included in an EGS4 distribution kit and the execution did not take much time. We defined UCSAMPL4 ratio as a value normalized by the execution time of the program on the standard computer, HP9000/735 (99MHz). The UCSAMPL4 took 15.1 sec.

Fig. 9 shows the UCSAMPL4 ratio for all computers tested. The results show that UCSAMPL4 ratio is close but not the same as EGS4 Unit. The performance of a Pentium CPUs is less than that of the RISC/UNIX systems, but that of the fastest Pentium PC reaches 0.8 EGS4 Unit. The Windows/NT on DEC 200 4/233 had the same performance of the OSF/1, reaching 1.6 EGS4 unit.

Fig. 10 shows clock dependency of the EGS4 Unit on Pentium CPUs. The result shows that the performance does not increase proportionally to the clock frequency and it depends on cache size and memory architecture. When the clock is over 100 MHz, the clock ratio for a Pentium (a EGS4 Unit times inverse of the clock frequency of a Pentium at particular frequency divided by the same at 60MHz) decreases.

The 133MHz Pentium (Delta) has a synchronized SRAM cache while Cygnus has an asynchronized SRAM cache. In addition, the Cygnus has high speed DRAM called EDO while Delta does not have. However, Delta has higher performance over Cygnus even if both have the same clock frequency for the CPU. Fig. 11 shows cache dependency of EGS4 Unit on a Pentium CPU. The result shows that the L1 cache improves the performance.

4. Correlation Between the EGS4 UNIT and SPECint92 & SPECfp92

Figs. 12 and 13 show the correlation. In EGS4 Unit versus SPECfp92 graph, SPARC20

and IBM590 have almost the same EGS4 Unit although they have different SPECfp92 values. This means that the SPECfp92 is not adequate for indexing of EGS4 Code System. Figs. 14 and 15 plot SPECint92 ratio and SPECfp92 ratio, respectively. The SPECint92 ratio of the standard computer is set to 1. Where the EGS4 Unit times SPECint92 value of an evaluated computer divided by that of the standard computer is the SPECint92 ratio. The SPECfp92 of an evaluated computer was also calculated in the same fashion. The result shows that SPECint92 is a better index than SPECfp92.

5. Coclusion

The EGS4 Benchmark Suite is appropriate to evaluate the computer performance for EGS4 Code System and hence EGS4 Unit became an index when one compares computer performances.

The optimization method of recent RISC/UNIX systems for the benchmark programs was evaluated. The best compiler option and an addition of particular math library made their performance higher.

The benchmark programs run on various PCs. The EGS4 Units of Pentium PCs was not very high, but the Pentium PCs may have better cost performance.

The correlation between the EGS4 Unit and SPECint92 & SPECfp92 was investigated. The SPECfp92 was found to be inadequate for the indexing.

We are planning to distribute the EGS4 Benchmark Suite.

We will investigate the correlation between a EGS4 Unit and a new benchmark suite, SPEC95.

5. Acknowledgment

We would like to thank High Performance Computing group of IBM at Kawasaki, HP Marketing group at Fuchu, System Engineers at DEC Ogikubo and at Tsukuba, System Engineer of Hitachi at KEK and System Engineer of Fujitsu at KEK for their help to run EGS4 benchmark programs. We appreciate Prof. Sverre Jarp of CERN, Dr. Atsushi Manabe and Dr. Takashi Sasaki of KEK for their help during our EGS4 benchmark project. We are grateful to the staff of KEK on-line group and KEK computing center for their support.

References

[1] Y. Yasu et al., *High Energy Physics (HEP) Benchmark Program*, Proceedings of the Third EGS4 User's Meeting in Japan, KEK Proceedings 93-15(1993), pp.83-104.

[2] W. R. Nelson, H. Hirayama and D. W. O. Rogers, *The EGS4 Code System*, SLAC-Report-265, (1985).

[3] A. F. Bielajew and D. W. O. Rogers, *A standard timing benchmark for EGS4 Monte Carlo Calculations*, Medical Physics, **19**, 303-304(1992).

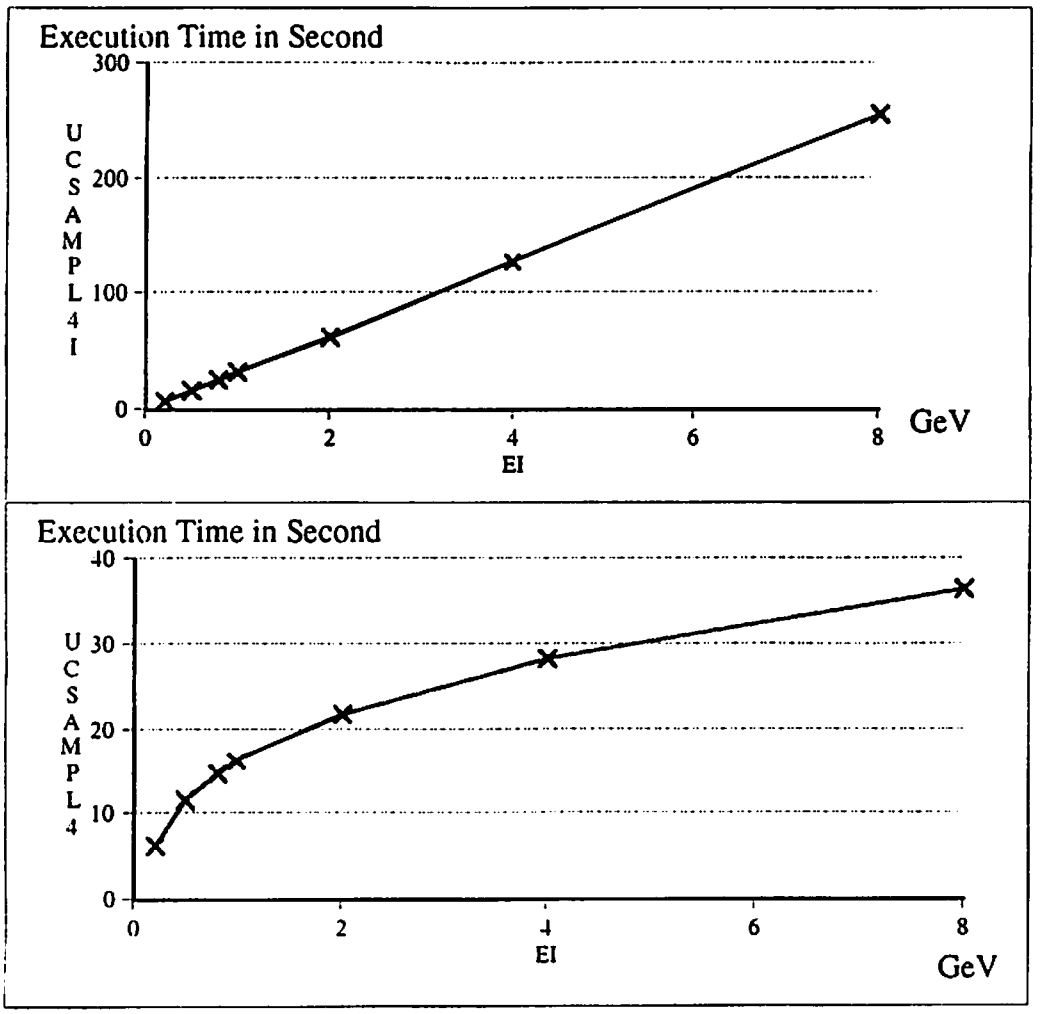

Fig.1 Correlation of EGS4 Execution Time and Incident Energy

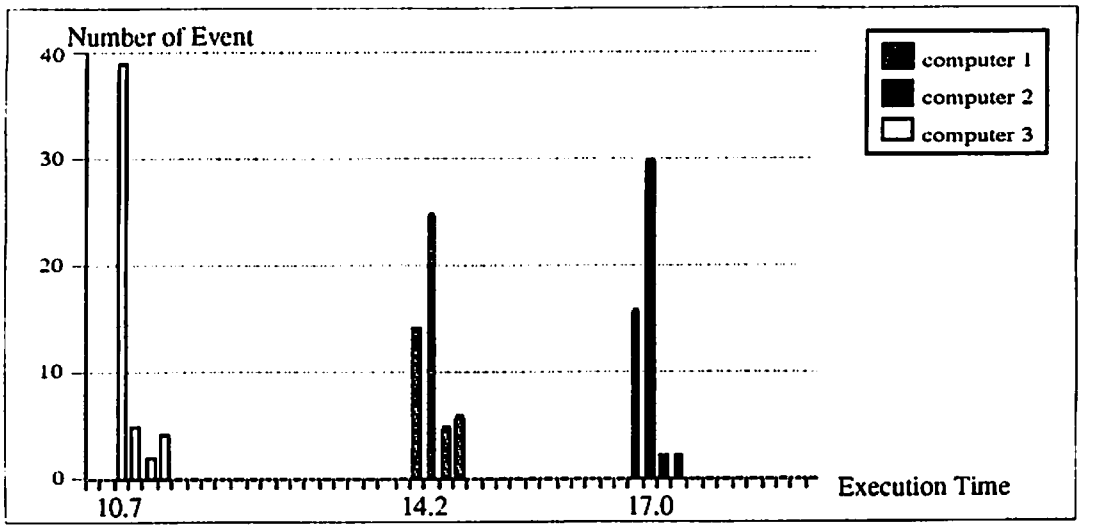

Fig. 2 Fluctuation of Execution Time by Workload

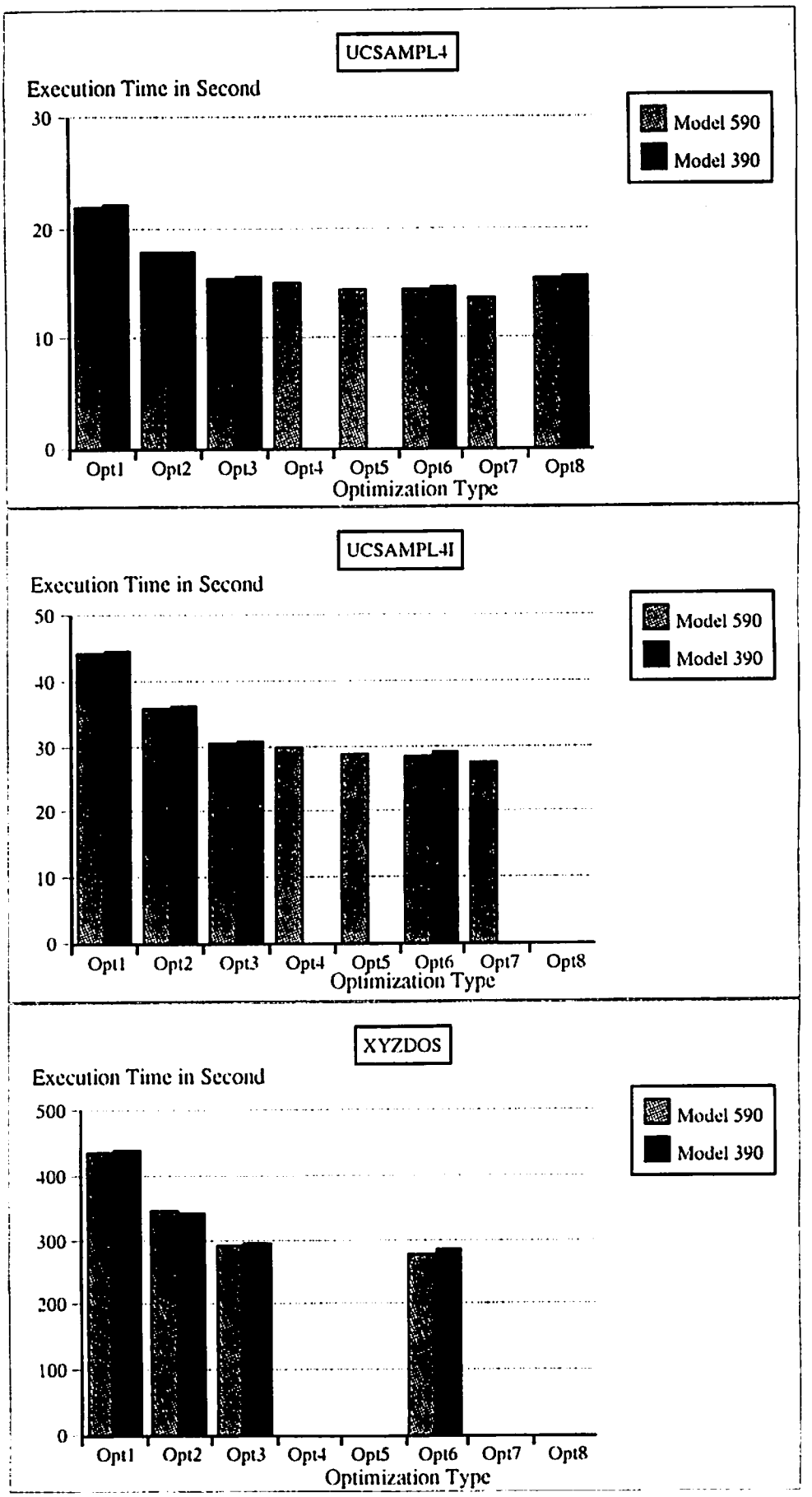

Fig. 3 EGS4 Benchmark Results on IBM Computers

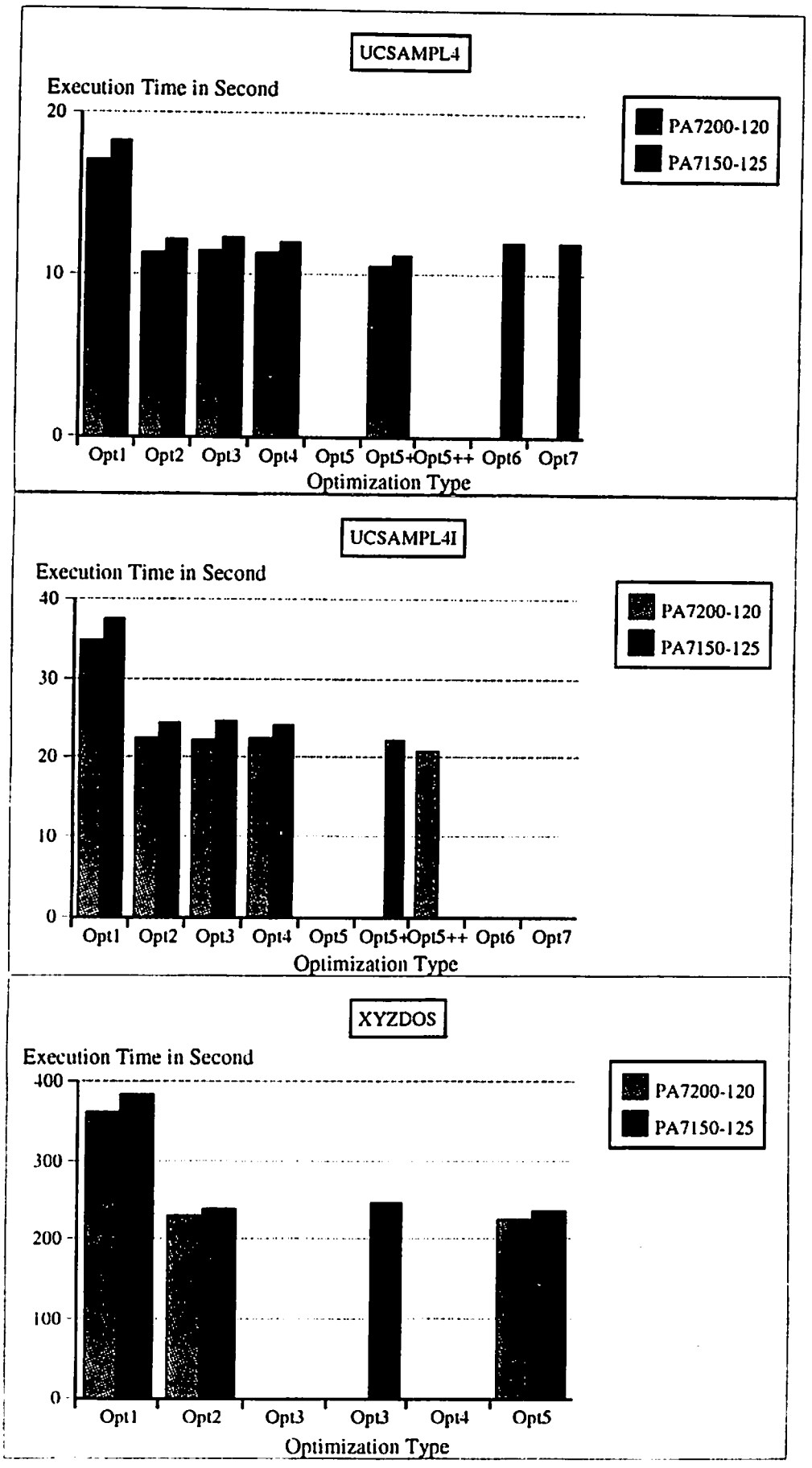

Fig. 4 EGS4 Benchmark Results on HP Computers

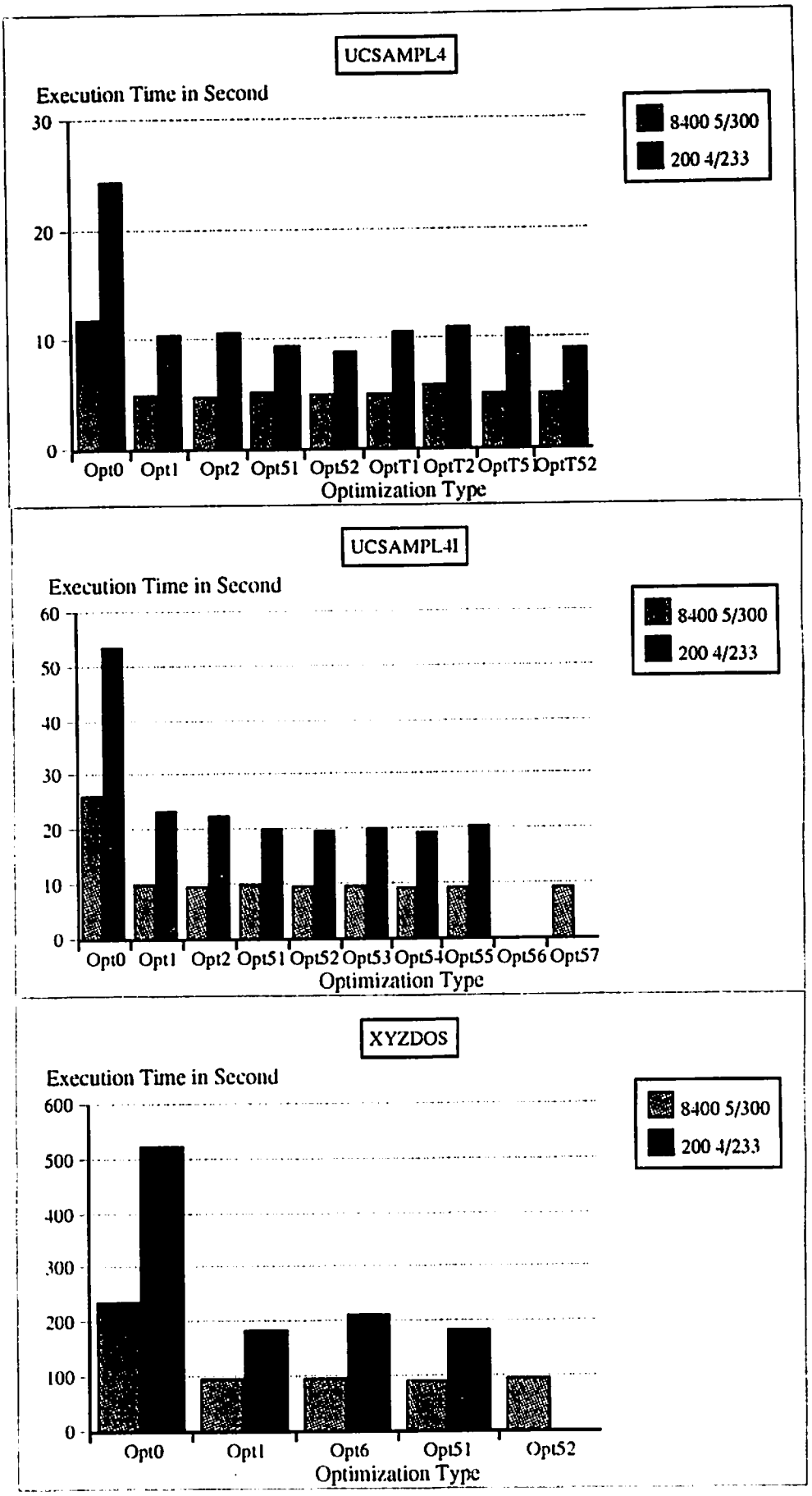

Fig. 5 EGS4 Benchmark Results on DEC Computers

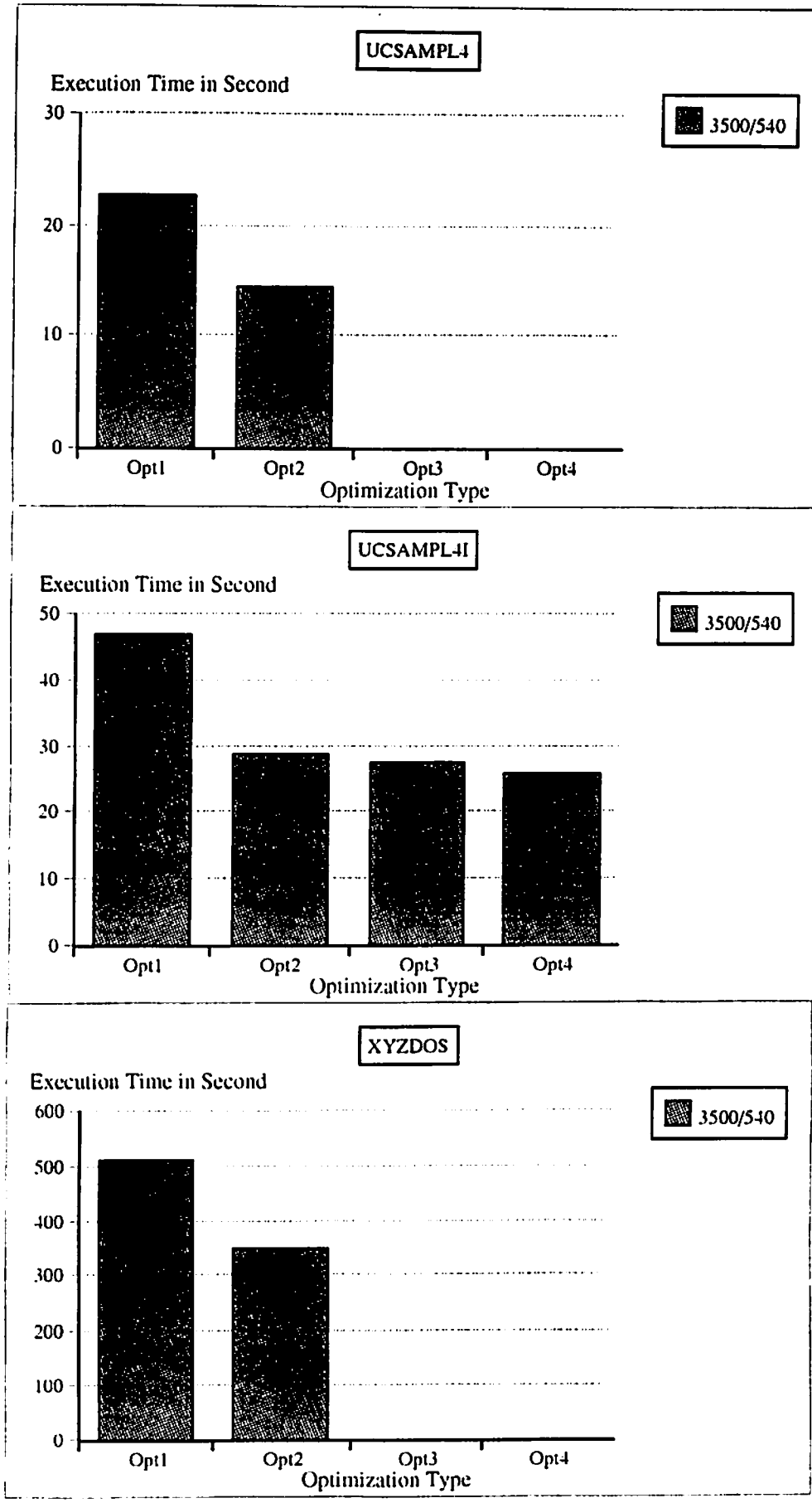

Fig. 6 EGS4 Benchmark Results on Hitachi Computer

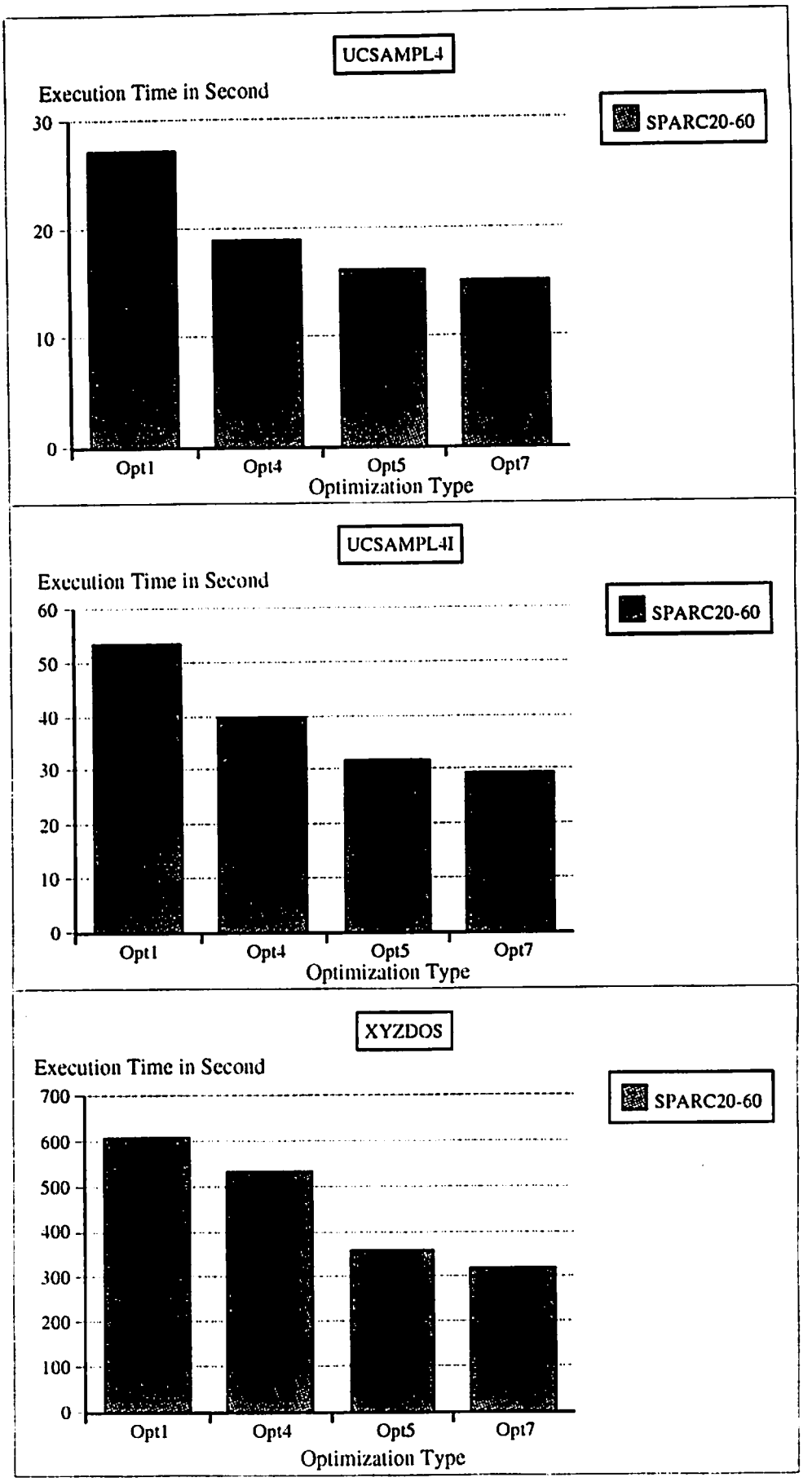

Fig. 7 EGS4 Benchmark Results on Fujitsu Computer

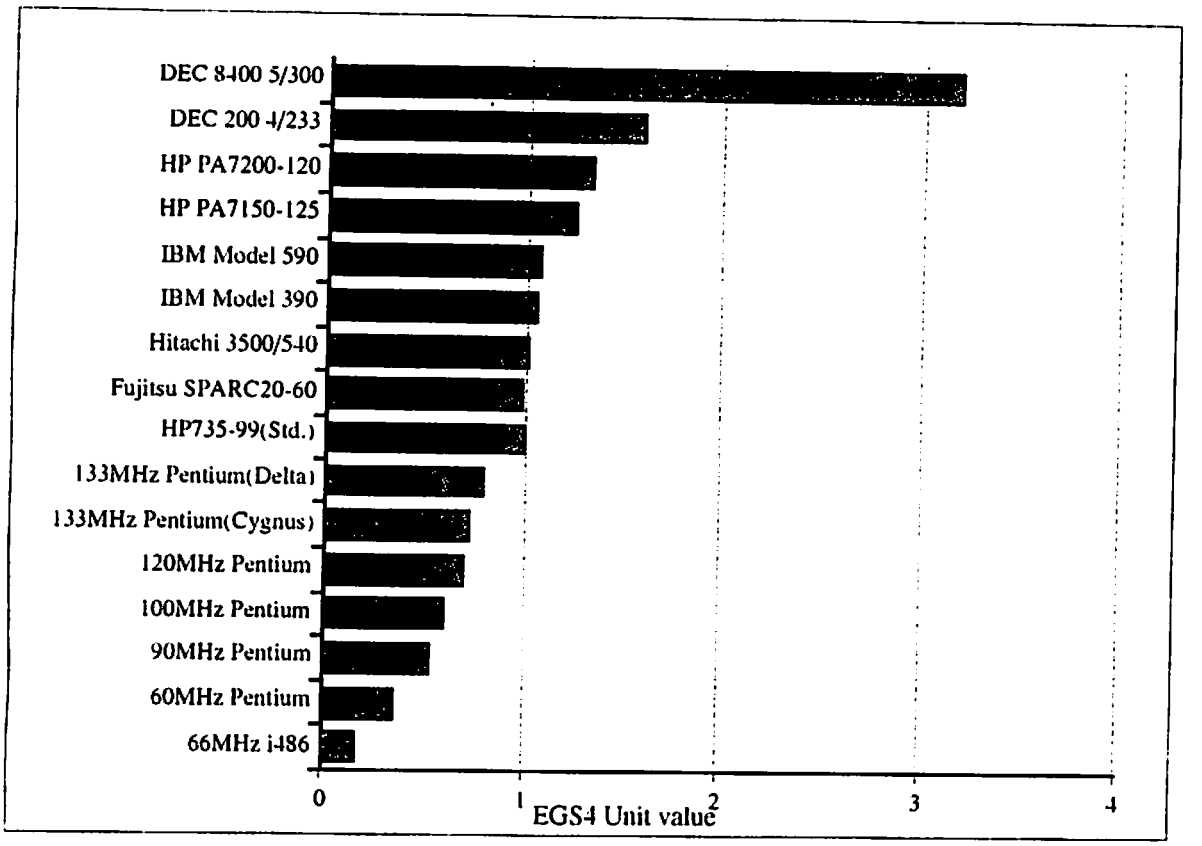

Fig. 8 EGS4 Unit

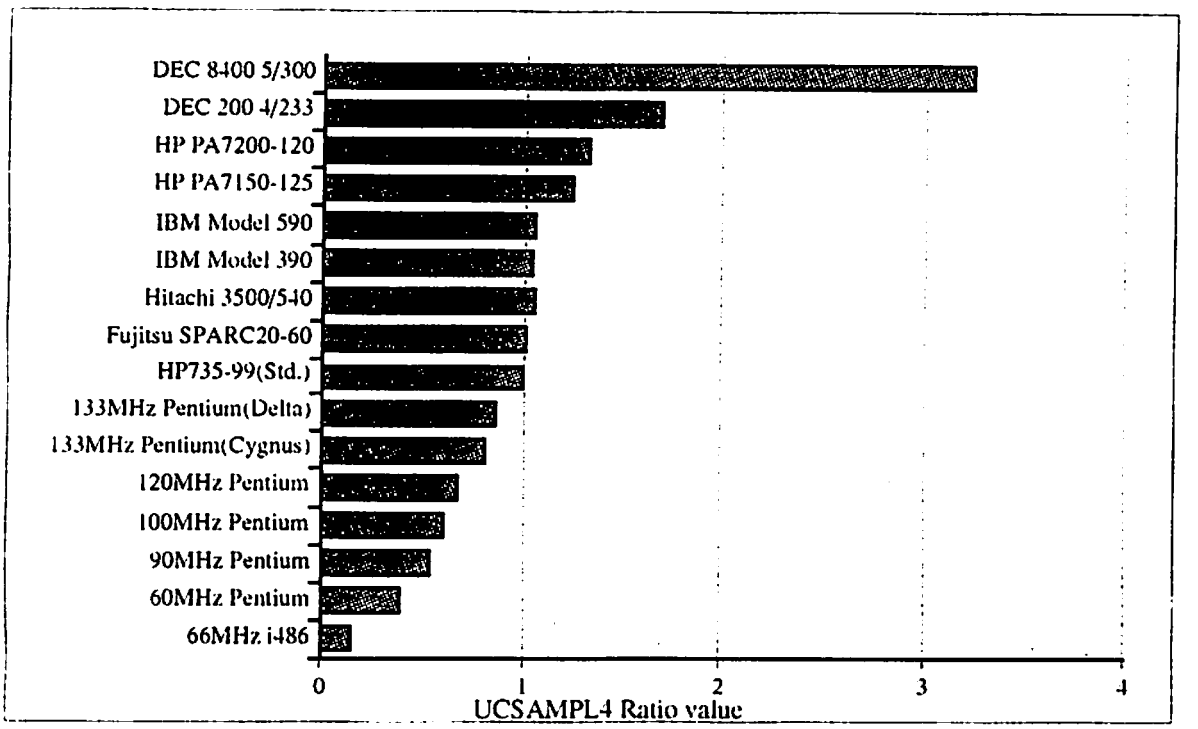

Fig. 9 UCSAMPL4 Ratio

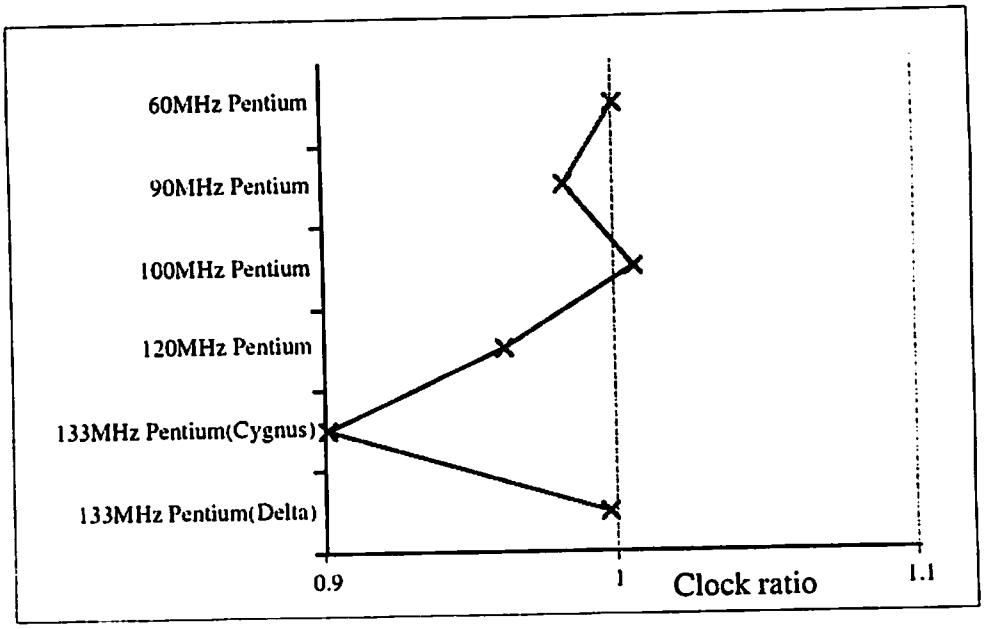

Fig. 10 Clock Dependency of EGS4 Unit on Pentium PCs

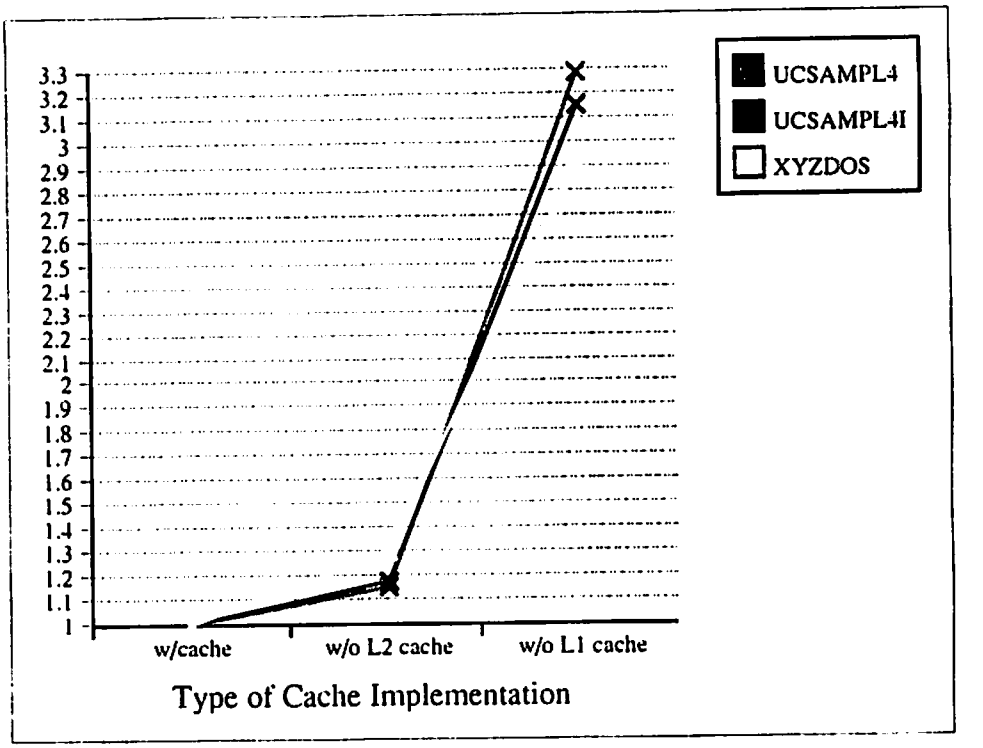

Fig. 11 Cache Dependency of EGS4 Unit on Pentium PC

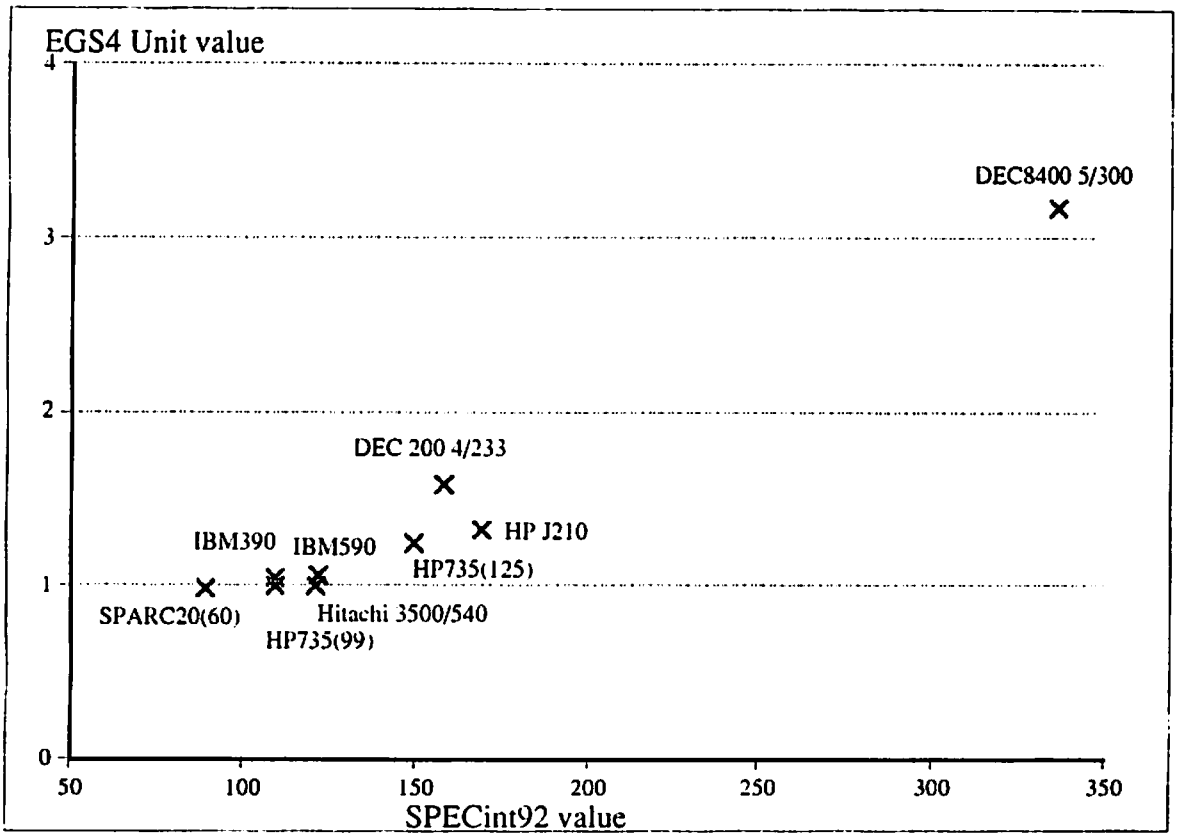

Fig. 12 Correlation of EGS4 Unit and SPECint92

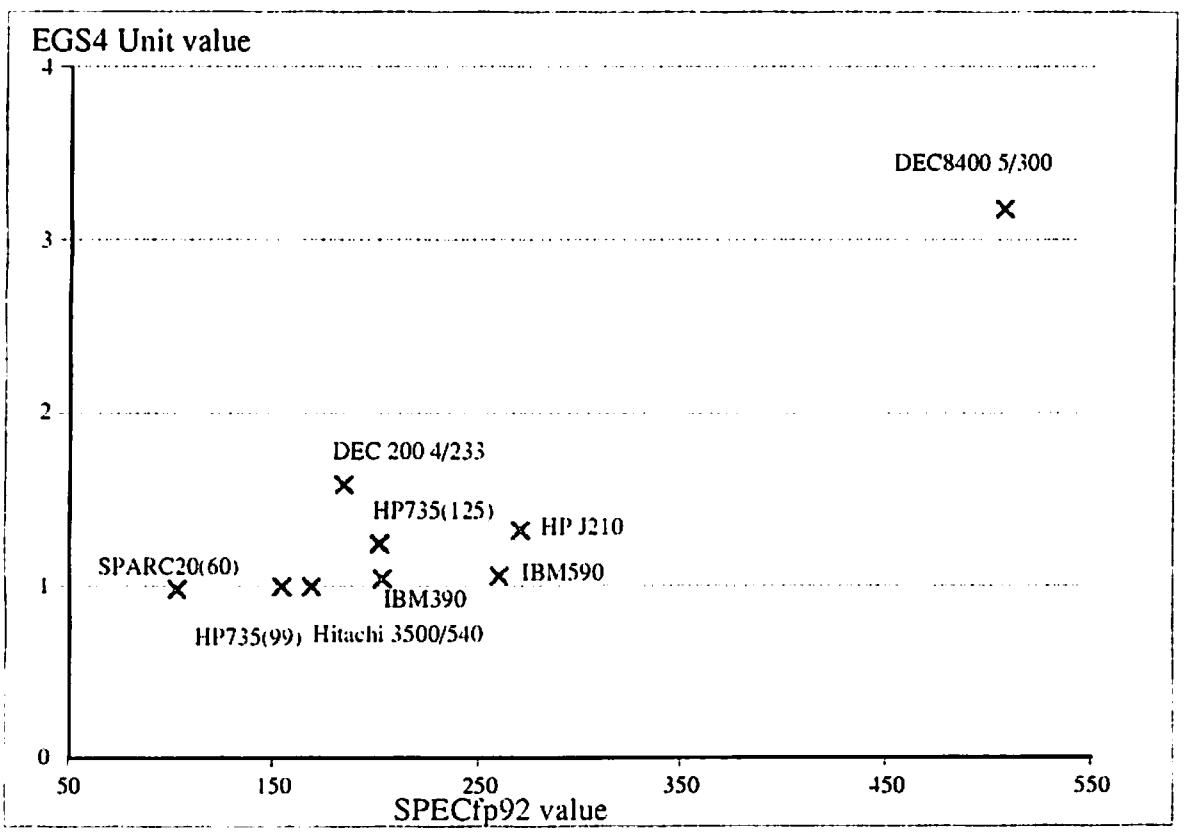

Fig. 13 Correlation of EGS4 Unit and SPECfp92

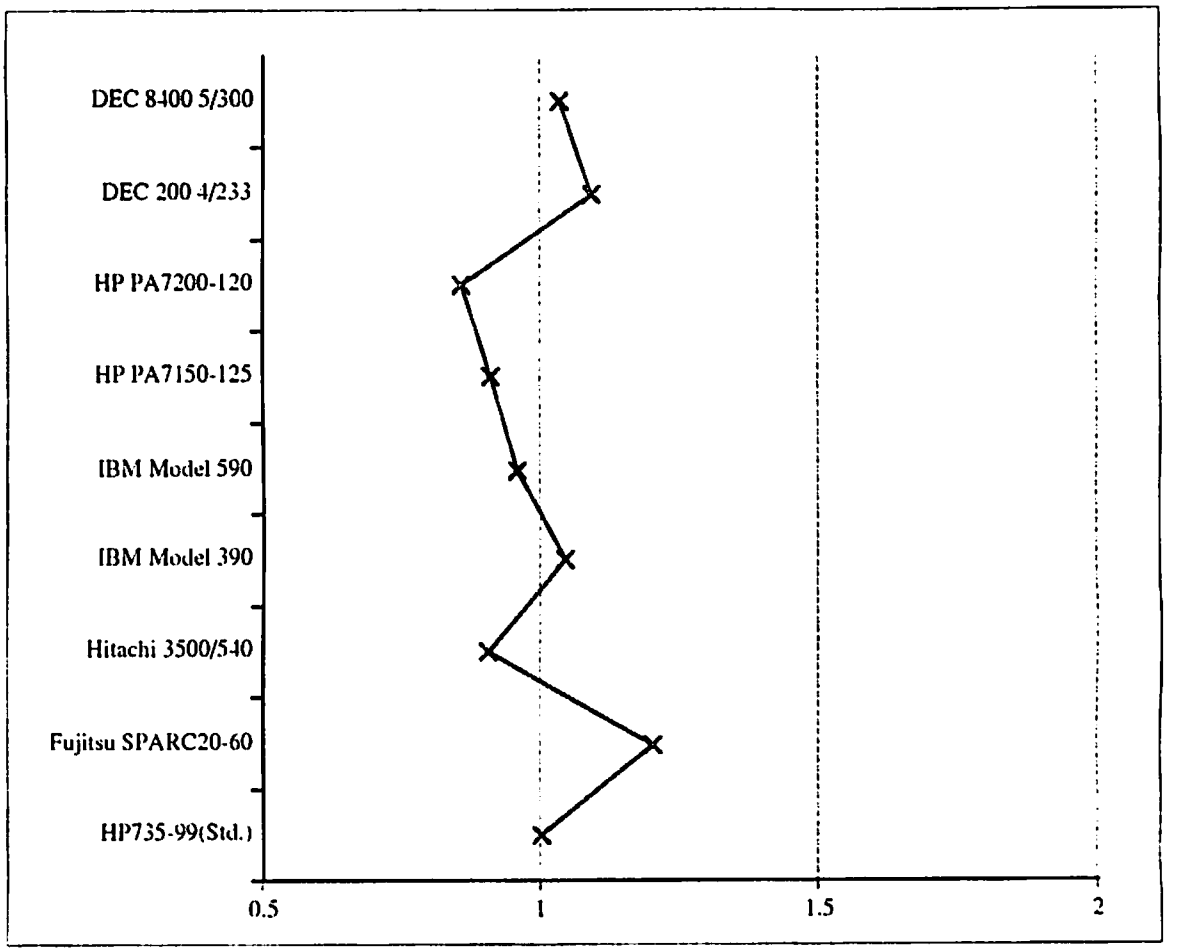

Fig 14 SPECint92 ratio of EGS4 Unit

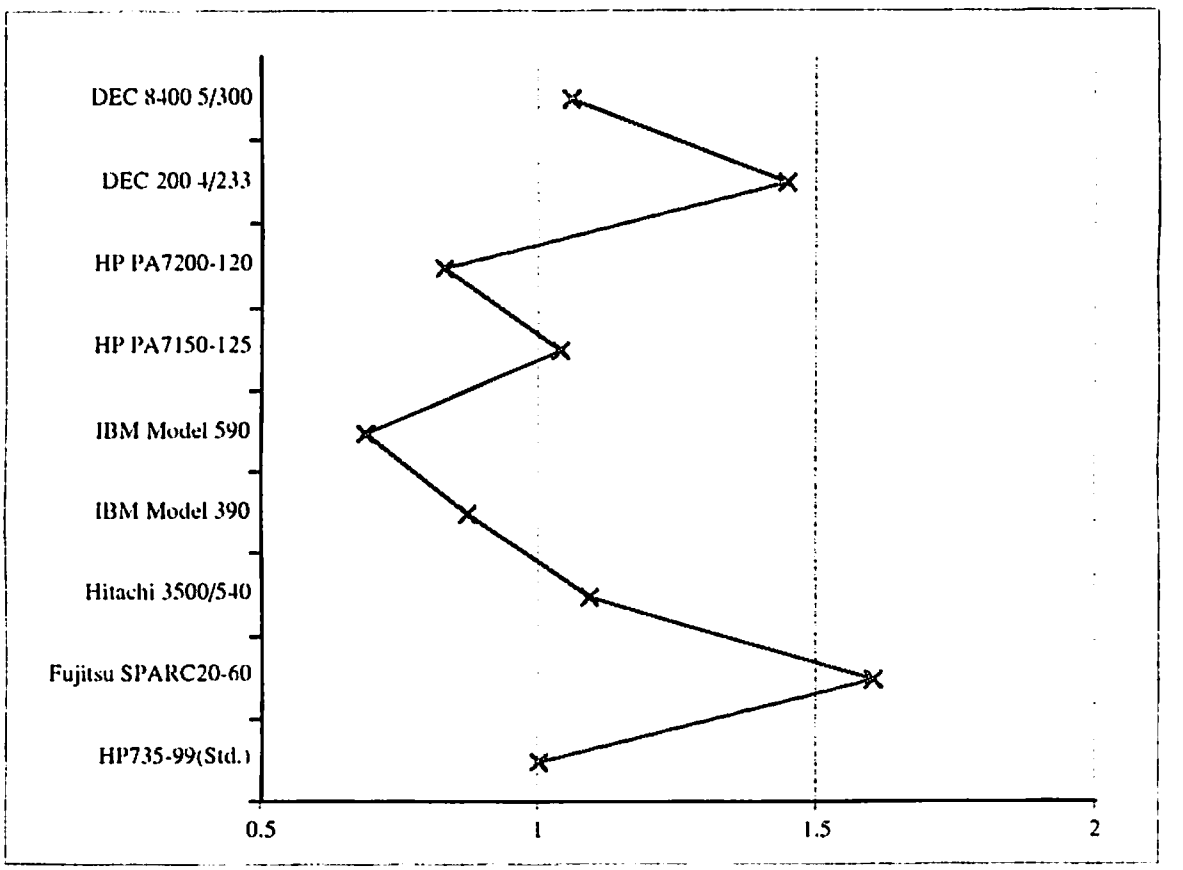

Fig 15 SPECfp92 ratio of EGS4 Unit

SIMULATION OF COMPTON SCATTER IN SINGLE-PHOTON EMISSION-COMPUTED TOMOGRAPHY

H. IIDA, Y. NARITA, and S. EBERL†

Department of Radiology and Nuclear Medicine
Research Institute for Brain and Blood Vessels-Akita
6-10 Senshu-kubota machi, Akita City, Akita 010 JAPAN

†*Department of Nuclear Medicine*
Royal Prince Alfred Hospital
Missenden NSW 2050, Australia

1. Introduction

Single-photon emission-computed tomography (SPECT) provides non-invasive determination of tomographic images of radio-labeled ligands in the body. With a help of a mathematical model that describes a kinetic behavior of the tracer in vivo, the measured radioactivity distribution may be converted to parametric images of several physiological functional processes. These parameters include regional blood flow, metabolism and neuro-receptor density, etc. in a quantitative manner.

In SPECT, however, the quantitative measurement of radioactivity distribution suffers from errors associated with the Compton scatter and/or attenuation processes of photons in the object. The photon absorption in the object has a large contribution, and often reaches 80% in typical brain studies and probably more in the thorax area. Several techniques have been proposed to correct for the attenuation.

The scatter is another source of errors, and known to cause a low-frequency artifact over the object in the reconstructed images, resulting in reduction in image contrast and quantitative accuracy. Several techniques were also proposed by several workers to correct for the artifacts due to scatter; e.g., scatter estimation from multiple-energy windows[1,2,3], model-based scatter prediction in the projection data using a convolution integral[4], scatter estimation using a transmission scan[5]. All these techniques are based on empirical assumptions, and therefore it has been desired to validate these technique in realistic settings that simulate clinical studies. Most techniques were however tested only for simplified phantom configurations such as circular or elliptical cylinders containing hot or cold spots. This is mainly because of complexity of the two error sources of attenuation and scatter, which need to be considered simultaneously.

A Monte Carlo simulation technique was proposed for evaluating accuracy of scatter and attenuation correction techniques[6,7]. Each physical process of photons in the object can be traced by a simulation code, and thus non-scattered true and/or scattered event distributions can be referred to the empirical correction techniques for any phantom configurations.

The present study was intended with the following two objectives:

(1) To establish a computer code to simulate the scatter process in SPECT using a EGS4 Monte Carlo simulation code.

(2) To validate the simulation code as a tool for evaluating the scatter correction techniques.

The scatter processes are generated by EGS4 simulation code, and the simulated energy spectra and spatial distributions are compared with those obtained by physical experiments using a conventional SPECT camera for several simplified phantom configurations.

2. Methods

2.1 EGS4 Simulation

Simulations were performed for 2 phantom configurations as described below.

1. Line source in a cylindrical phantom.

In the first simulation, a Tc-99m line source (141 keV) of 29.8 cm in length was placed in a water-filled cylindrical phantom (diameter; 20 cm, length; 30 cm). Photons were emitted randomly and uniformly from the line source. A simulated rectangular detector plate was placed at 2 cm distant from the surface of the phantom (see Fig. 1). The sensitivity of the detector was adjusted as a function of energy of the detected gamma ray by assuming a 9.5 mm thick NaI(Tl) crystal.

The photon trajectories were simulated by the EGS4 simulation code including the Rayley scattering processes. The trajectories of the photons emitted from the phantom were projected onto the detector surface without allowing further interactions outside the phantom. The position, incident direction, energy and history (number of Compton scattering) were recorded. Only events with incident angle $< \pm 2.1$ degree at the detector surface were accepted, corresponding to the collimator for a typical commercial SPECT camera. The line source was placed at the center and off center laterally and also radially with respect to the detector (Fig 3). This simulation was also performed for an uncollimated detector. The energy resolution of the detector was assumed to be 12 keV (8.5%). Energy spectra were recorded for each of the line source positions in the detector. Line spread functions on the

projection data were also recorded, assuming a ±10% energy window centered on 140 keV.

2. Scatter phantom

The second simulation assumed a cylindrical cold water-filled area in a radioactive (Tc-99m; 141 keV) cylindrical water-filled uniform phantom (see Fig. 2). Assuming the same collimator geometry as described above, projection data were recorded for 90 views in 4 degree steps for scattered, non-scattered true, and total events, with an energy window of 140 keV ±10%. A 2-dimensional sinogram was generated from this, and tomographic images were reconstructed for the scatter, non-scatter and total events.

2.2 Experiment by SPECT Camera

An experiment was performed using a physical phantom with the same geometrical configuration as the simulated phantom shown in Fig. 1 (Line Phantom). Water was filled in an acrylic phantom (20 cm diameter and 30 cm long, wall thickness of 5 mm), and a Tc-99m line source was placed in the phantom at various different positions (see Fig. 3). Energy spectra and the line-spread functions were then measured using a commercial gamma cameras (Trionix Triad XLT and Siemens ZLC-7500), and were compared with those obtained by the simulation study described above.

A further experiment was performed using a water-filled phantom (PVE Phantom) with the same geometry as shown in Fig. 2. The wall of the phantom is 0.5 mm thick and made by Vinyl chloride. Tc-99m water was filled in the outer compartment of the phantom, and cold water in the inner compartment. Using the ZLC-7500 camera, an energy spectrum was recorded. Projection data were also acquired with an energy window of 140 keV ±10% for 64 views in 5.625 degree steps. Tomographic images were then reconstructed with a correction for attenuation.

3. Results and discussion

Figure 4 shows a comparison of an energy spectrum for a line source in a uniform phantom obtained by the EGS4 simulation with those measured by the experiment . Energy spectra were also compared in Fig. 5 for the PVE phantom (Fig. 2). It should be noted that, in the simulation, each photon emission process can be classified into non-scattered true, 1-st order scatter, 2nd-order scatter etc. For both phantoms, spectra were in good agreement between the simulation and the experiment except for an energy range around 75 keV. The peaks observed at 75 keV and 88 keV in the experiment are due to K shell x-rays from the lead collimator (74.97 keV and 88.01 keV). The relatively larger

number of Pb K x-rays for the PVE phantom (Fig 5) is probably responsible for the somewhat worse agreement between simulated and experimental spectrum compared with the Line phantom results (Fig 4).

Figure 6 shows comparisons of line spread functions in the projection data for the line source experiment for various line-source positions. Energy window was set to be 140 keV ±10% in this experiment. Good agreement was observed between the simulation and the experiment for all conditions. The discrepancy between the measured and simulated results observed with the line source close to the detector (Fig 6 top left) can be explained by septal penetration becoming a significant factor in this low scatter configuration. It was also observed in the simulation study that change of the photon-incident acceptance angle at the detector (i.e., collimator acceptance angle) caused only small change in the relative spectrum, although the absolute counts were highly dependent on the change. This suggests that the collimator geometry mainly affects the detector sensitivity and spatial resolution, but not the scatter-to-true fraction.

Figure 7 shows a result of the scatter phantom experiment. Significant counts were observed in the non-radioactive area. This is considered to be mainly due to the scatter, as this is well reproduced by the EGS4 simulation as shown in Fig. 8. It can be seen in Fig. 8 that the absolute counts are greater in the total event image by approximately 20% compared with the true distribution.

Energy spectra are compared in Fig. 9 with and without a collimator for both of the Monte Carlo simulations and the experiments. Removing the collimator increased the sensitivity by a factor of approximately 10. However, spectra appeared to be rather insensitive to the exact type of collimator used and the assumed photon acceptance angle.

It should be mentioned that the phantom experiment provided the energy spectrum that had a significant peak around E = 75 keV. This is considered to be caused by K x-rays from the lead collimator and/or lead shield of other detector heads. It should also be noted that significant contamination was observed even after removing the collimators. This may not be problematic for Tc-99m studies, as the energy window can avoid this energy range. However, this might provide significant artifacts in Tl-201 and Xe-133 studies, as the energy window is likely to include this energy range around 80 keV. Further study is needed in order to investigate effects of this.

Both the energy spectra and the projection data generated from EGS4 simulation code were found to be in good agreement with the observations from conventional SPECT cameras. Scatter processes are thus considered to be well reproduced by the EGS4 simulation code, allowing the validation of several scatter correction techniques in quantitative SPECT.

References

[1] K. Ogawa et al., *A Practical Method for Position-Dependent Compton-Scatter Correction in Single Photon Emission CT*, IEEE TMI, **10**, 409-412(1991).

[2] M. A. King et al., *A dual-photopeak window method for scatter correction*, J. Nucl. Med., **33**, 605-612(1992).

[3] R. J. Jaszczak et al., *Improved SPECT quantification using compensation for scatter photons*, J. Nucl. Med., **25**, 893-900(1984).

[4] B. Axellson et al., *Subtraction of Compton-scattered photons in single-photon emission computerized tomography*, J. Nucl. Med., **25**, 490-494(1994).

[5] S. R. Meikle et al., *A transmission-dependent method for scatter correction in SPECT*, J. Nucl. Med., **35**, 360-367(1994).

[6] M. Ljungberg et al., *Attenuation and scatter correction in SPECT for sources in a nonhomogeneous object: a Monte Carlo study*, J. Nucl. Med., **32**, 1278-1284(1991).

[7] M. Ljungberg et al., *Comparison of four scatter correction methods using Monte Carlo simulated source distributions*, J. Nucl. Med. **35**, 143-151(1994).

Simulation System

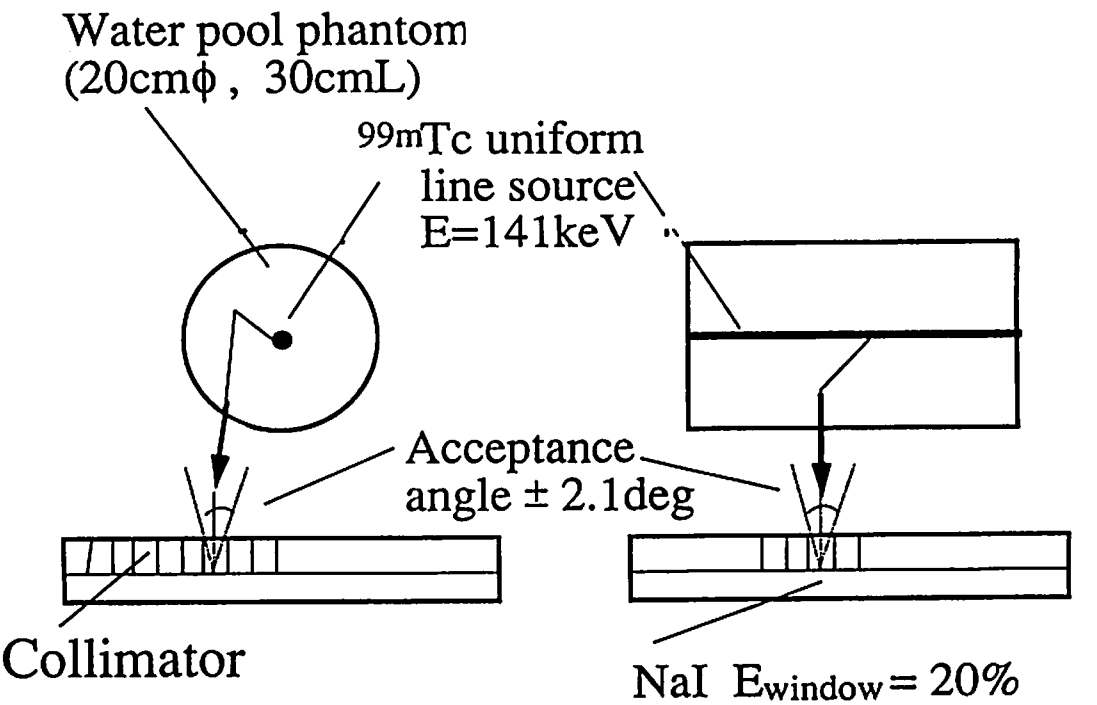

Figure 1 Simulation diagram for a line source in a water filled phantom. A line source of Tc-99m was placed in a uniform cylindrical phantom filled with water. The phantom is 20 cm in diameter and 30 cm in length. Photons (141 keV) are emitted uniformly from the line source, and the trajectories were calculated by an EGS4 simulation code. Photon interactions were stopped when the photon reached the out side of the phantom, and the trajectory was projected onto the detector surface. Assuming a collimator 40 mm thick and 3 mm in diameter, events with acceptance angles of $< \pm 2.1$ degree were recorded. The energy spectrum and spatial line-spread function were recorded for various positions of the line source.

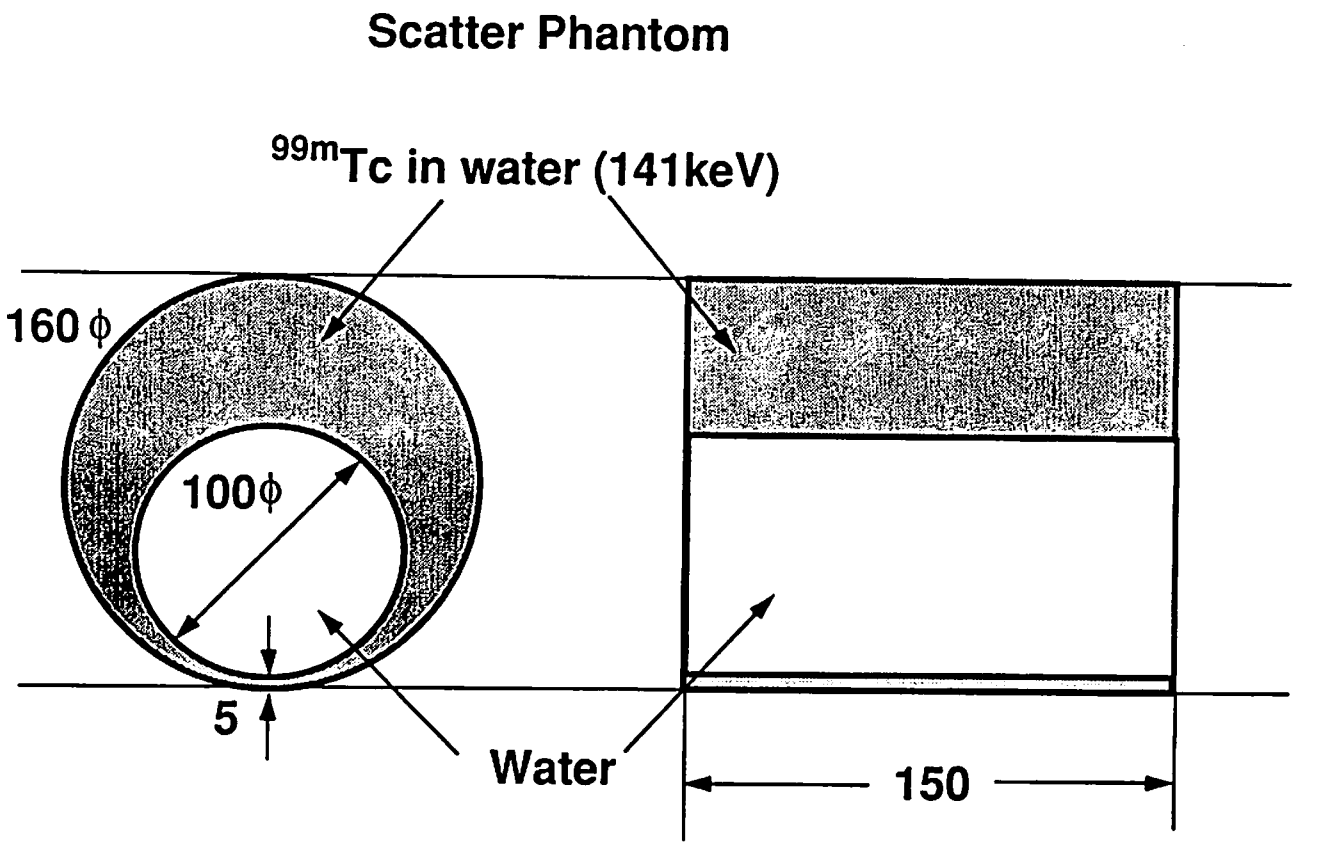

Figure 2 Simulation diagram for a scatter phantom. Tc-99m water is distributed in hatched area. Non-hatched area corresponds non-radioactive water. Photons are generated and trajectories are simulated by the EGS4 simulation code.

Experimental Setup

ZLC-7500 Gamma Camera (Siemens)

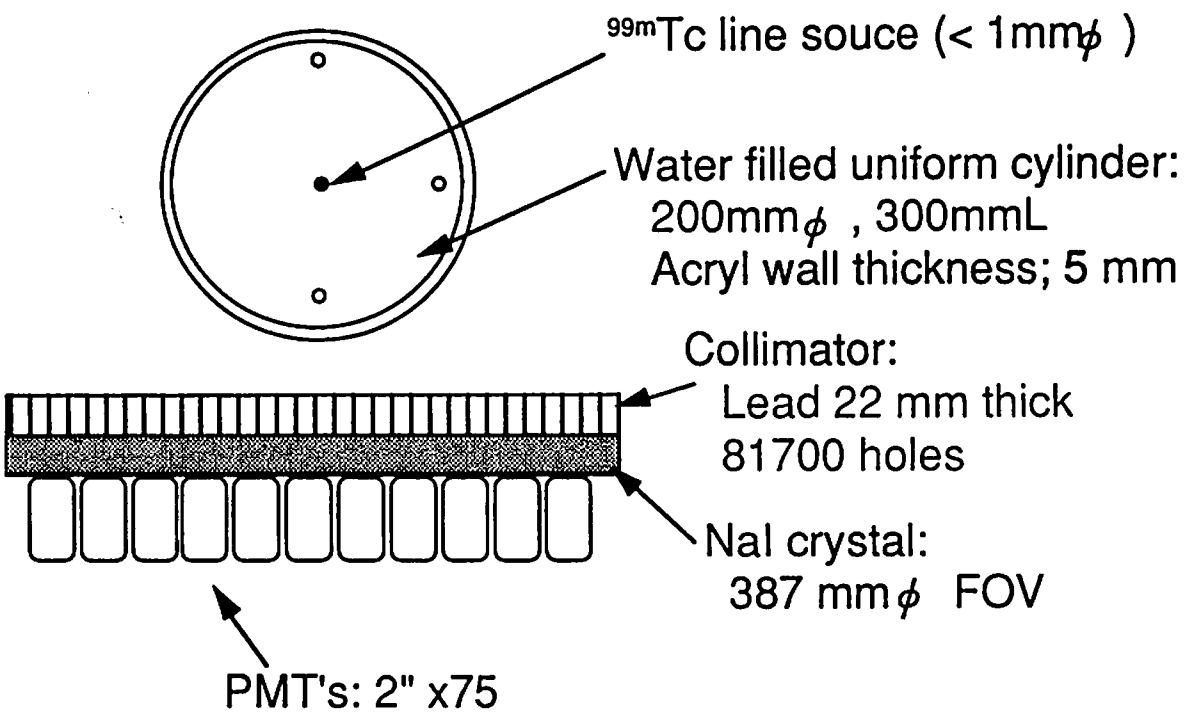

Figure 3 Experimental setup used of with a commercial SPECT camera (Siemens ZLC-7500).

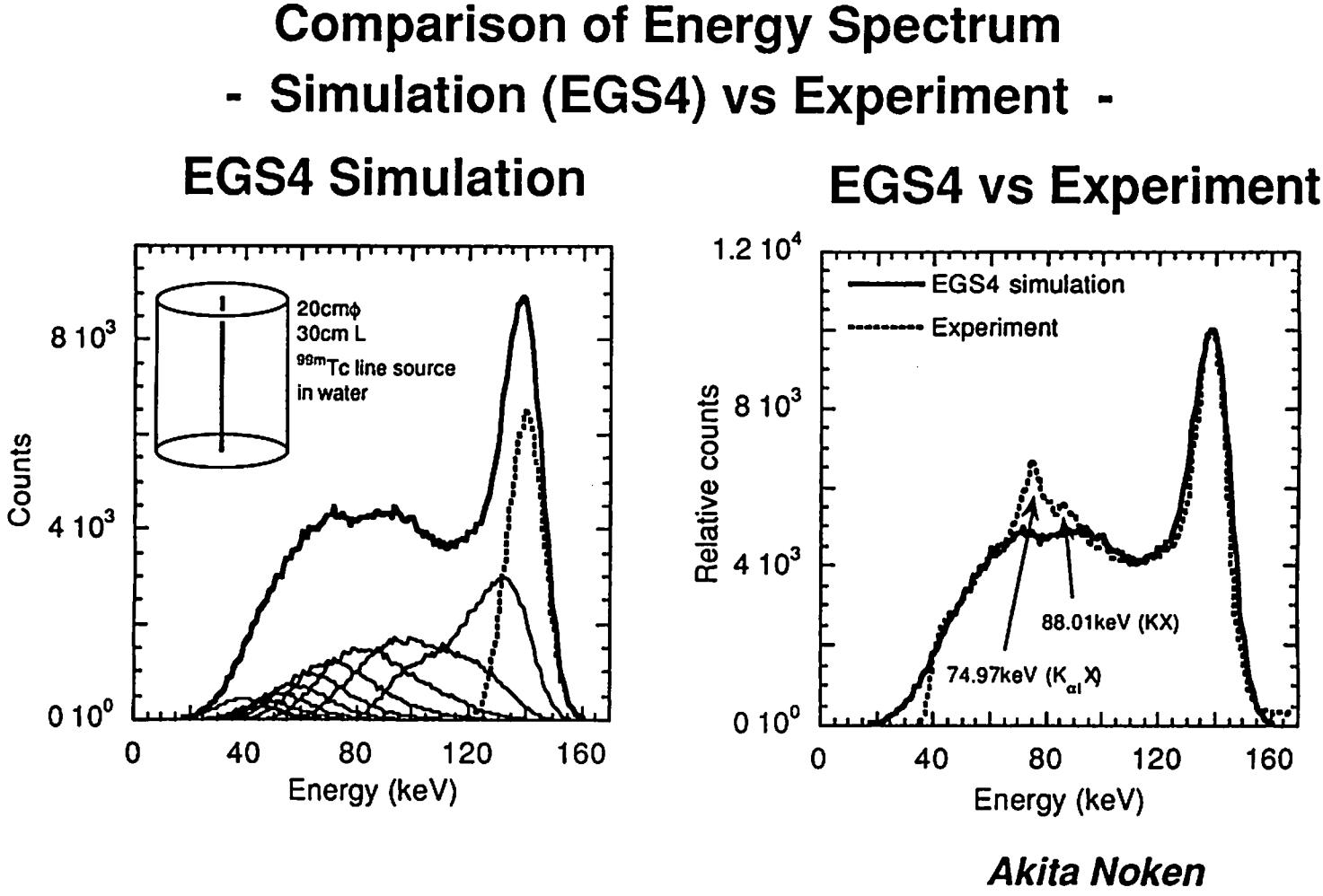

Figure 4 Comparisons of energy spectra for a line source in a water-filled cylindrical phantom. Left demonstrates results of the EGS4 simulation, showing individual spectra for non-scattered true, 1st-order and multiple scattered events. Energy spectrum for the total events are indicated by a bold solid line. Right shows a comparison of the simulated energy spectrum including both scatter and non-scattered events with that measured on the gamma camera (TRIONIX Triad XLT). Good agreement was observed except for an energy range around 75-90 keV, due to contamination with K x-rays from the lead collimator.

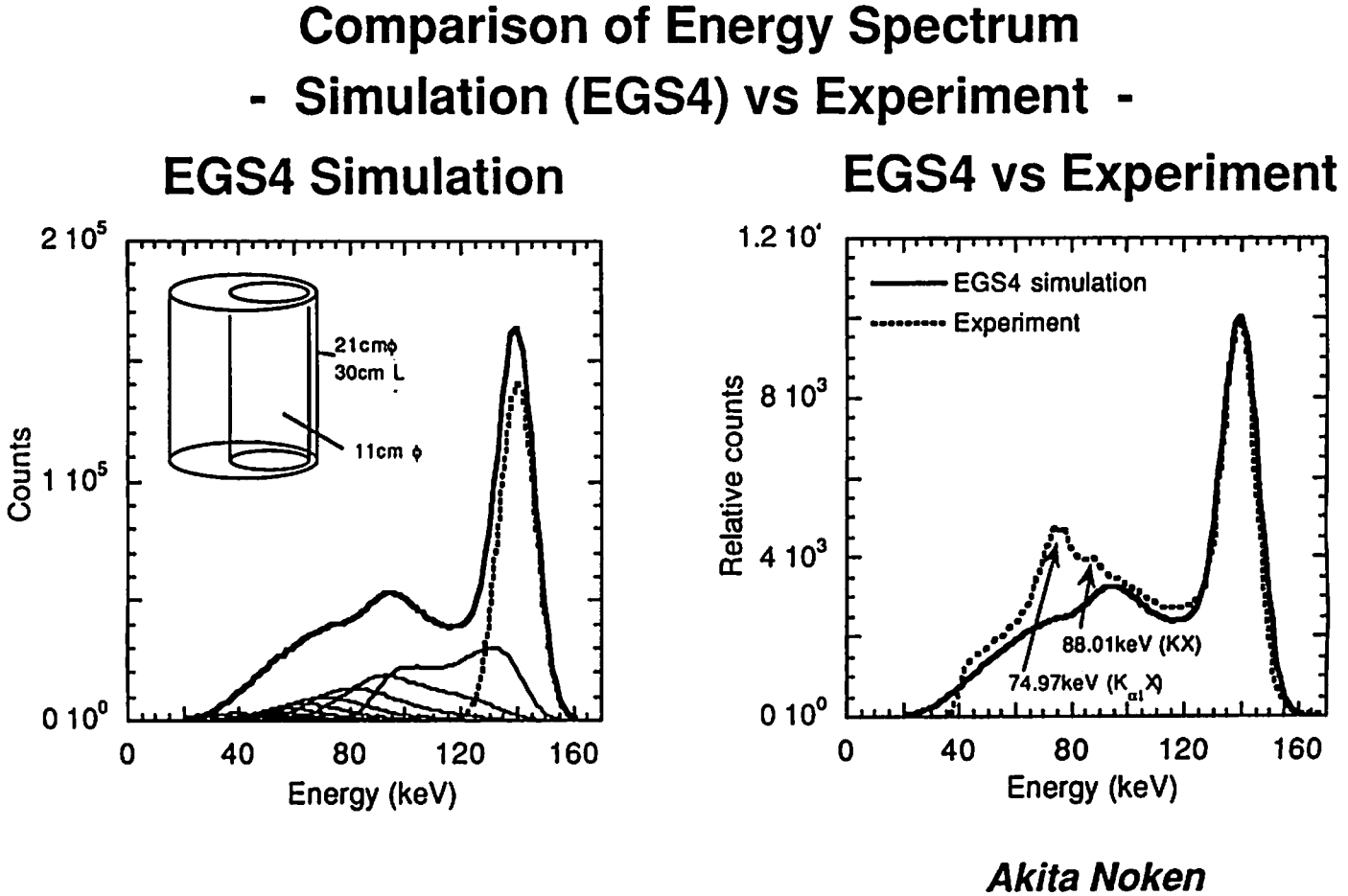

Figure 5 Comparison of energy spectra for the scatter phantom. Notations are the same as for Fig. 4. Experimental data were obtained using TRIONIX Triad XLT gamma camera.

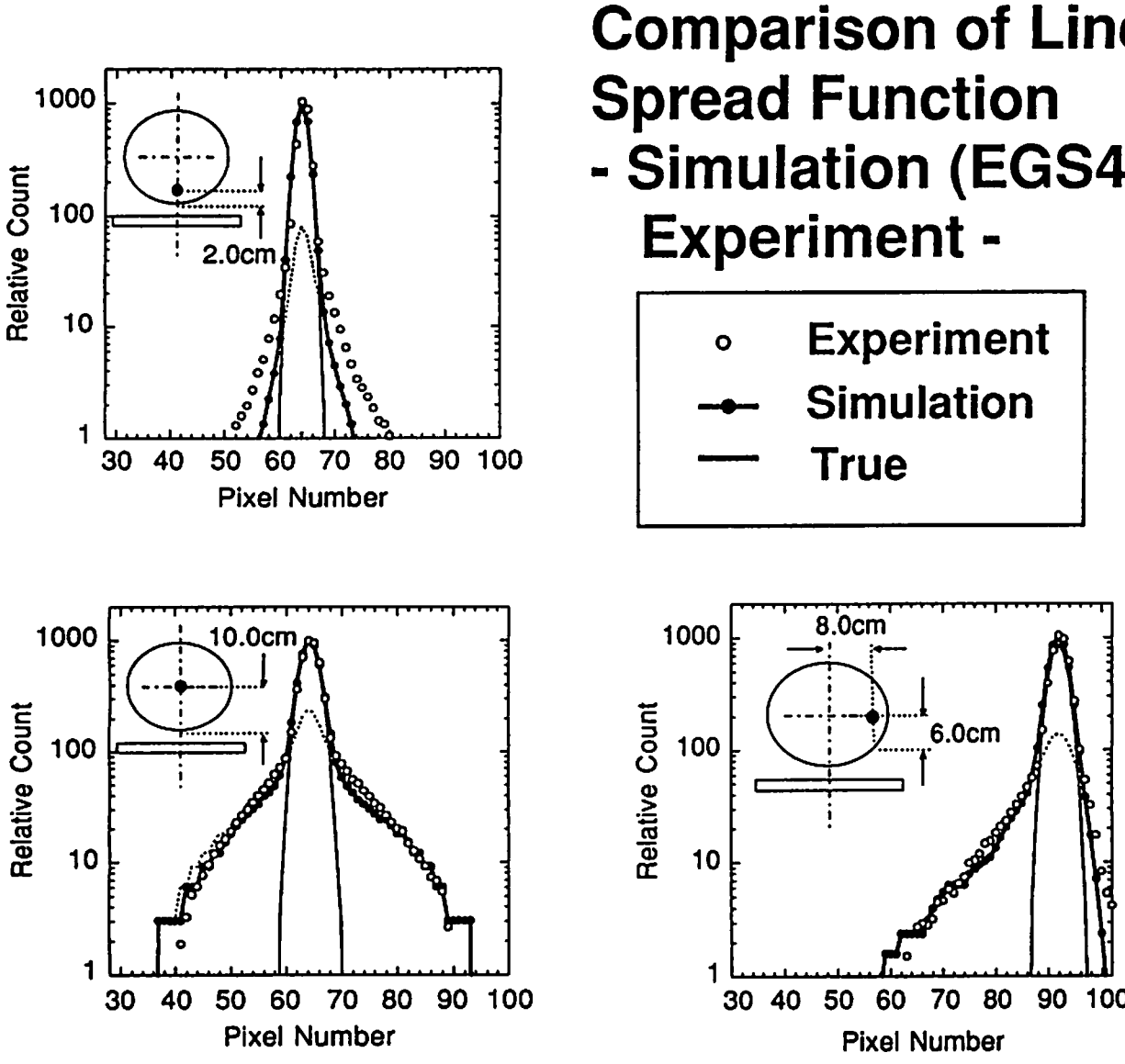

Figure 6 Comparison of spatial line spread functions in the projection data for various line source positions. Bold solid lines correspond to the simulated total events, and thin solid lines correspond to the non-scattered true events. Circles denote results of the experiment (Siemens ZLC-7500).

Effects of Retracting Collimator on Energy Spectrum

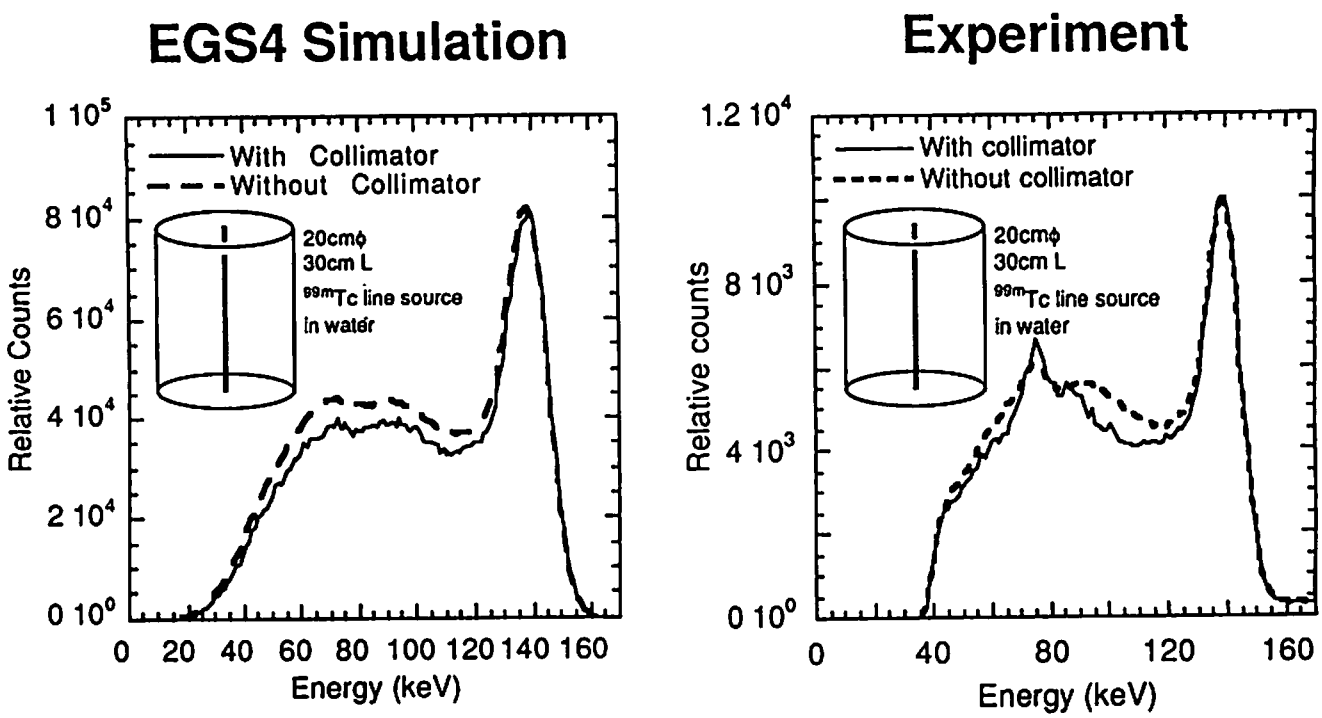

Figure 7 An tomographic image and its profile obtained from the scatter phantom experiment. Experiment was performed by use of Siemens ZLC-7500 gamma camera. Radioactivity observed in the cold area is probably due to the scatter.

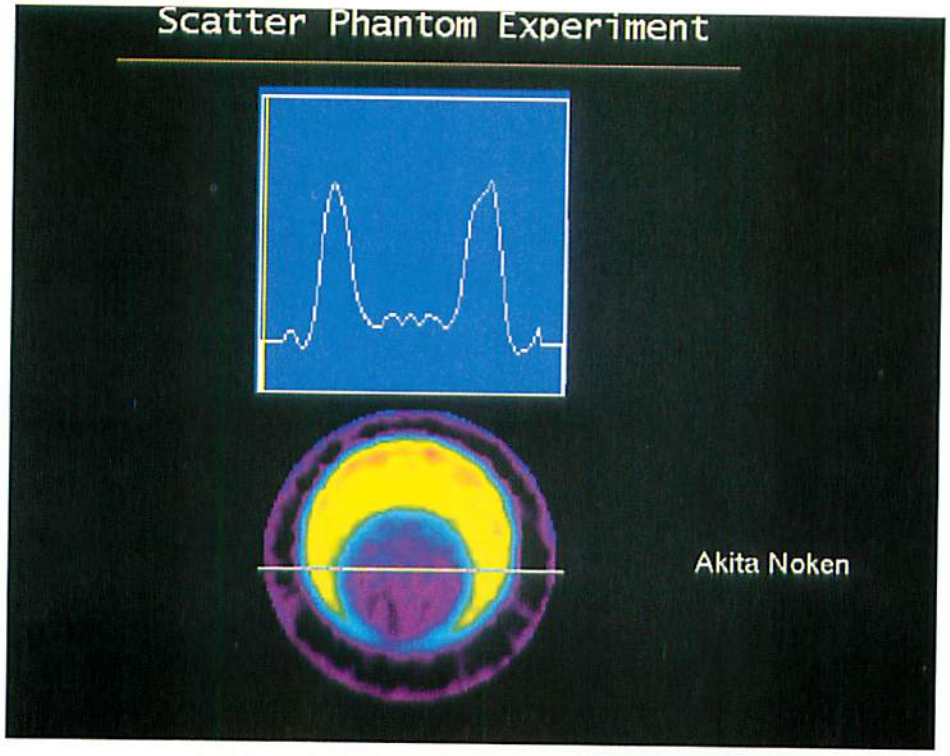

Figure 8 Results of the Monte Carlo simulation for the scatter phantom configuration. Projection data at 0 degree (top), sinogram (middle) and reconstructed images (bottom) are presented for total (scatter + true) (left), true (middle) and scatter events (right).

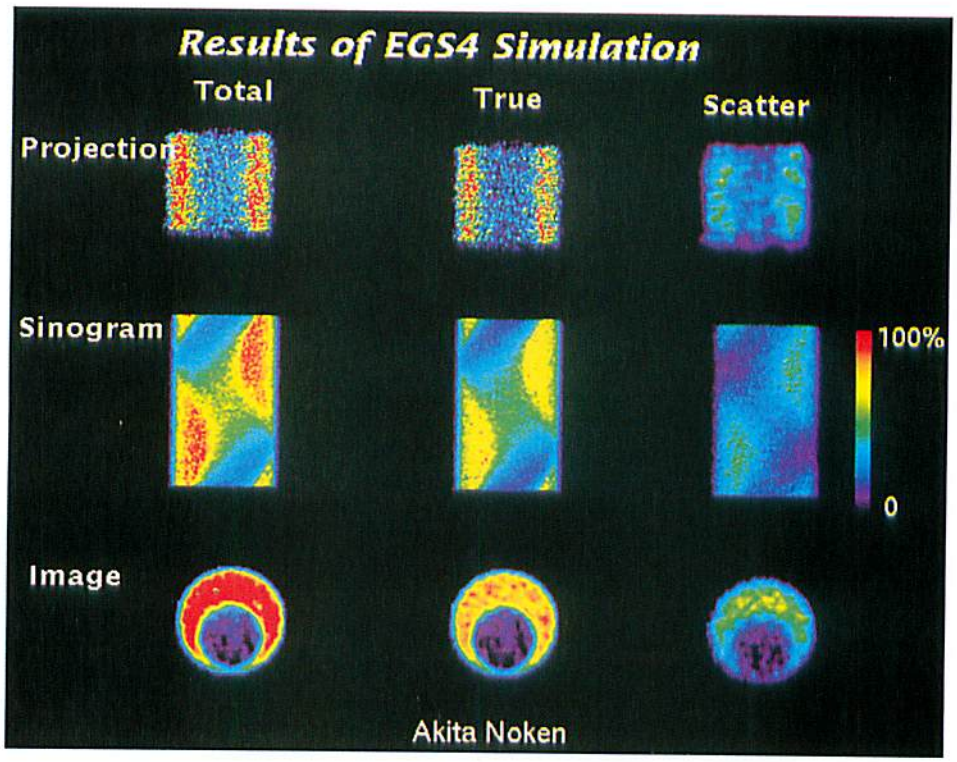

Figure 9 Effects of retracting a collimator on energy spectra. Data were displayed for the EGS4 simulation (left) and for the phantom experiment using the TRIONIX Triad XLT camera (right). Note that the peak around 75 keV still remains in the experimental data even after retracting the collimator, probably due to K-X rays from the lead collimator or the lead shield of other heads.

MONTE CARLO CALCULATIONS OF EFFECTIVE DOSES IN NON-UNIFORM BEAM EXPOSURE FOR HIGH ENERGY ELECTRONS

M. HIKOJI, M. KATAGIRI, H. TAKAHASHI, M. KITAICHI, and S. SAWAMURA

Department of Atomic Science and Nuclear Engineering, Hokkaido University, North 13, West 8, Kita-ku Sapporo, 060, Japan

I. NOJIRI

Power Reactor and Nuclear Fuel Development Corporation, Tokai-mura, Ibaraki-ken, 319-11, Japan

Abstract

In order to estimate the radiation hazards in the accidental exposure of energetic electrons, the effective doses were calculated by using the EGS4 Monte Carlo simulation code and the MIRD-5 human phantom for high energy electron beams as those from LINAC, in which non uniform exposure on a human body would be occurred. The calculation has shown that the effective doses depend not only on the incident electron energy but also on the beam size and the exposure position on the body. To investigate the difference by the sex, the effective doses with and without the breast on a body were calculated.

1. Introduction

For effective radiation protection, ICRP has recommended the various conversion factors, such as H_T (dose equivalent, equivalent dose in ICRP Publ.60) or H_E (effective dose equivalent) per unit particle fluence, in the case of photons (0.1-10 MeV) and neutrons (2.5×10^{-8} to 14 MeV). According to the ICRP Publ.60 in which some concepts and terminology of dosimetric quantities are changed, the effective dose E, formerly defined as the effective dose equivalent H_E, has been calculated for neutrons and photons. However in the case of electrons, it has not yet recommended such factors. Instead, ICRP has shown the maximum dose equivalent and the dose equivalent at 1 cm of a semi-infinite

slab of 30 cm thickness whose composition is the same as that of an ICRU sphere. And for the low energy electrons than 2 MeV, in which energy region most of beta rays are included, conversion factors from absorbed dose in air to tissue dose equivalents of skin were recommended.

In the progress of LINAC applications, radiation protection from high energy electrons of more than 2 MeV has become a great priority. For electrons of energy above 2 MeV, it would be necessary to consider the equivalent dose to organs lying deeper than the skin. Therefore, we have already calculated the conversion factors in uniform exposure of high energy electrons for several geometrical irradiation conditions such as AP, PA, and LAT. However, the geometrical irradiation condition in LINAC applications is mostly like beam exposure. Dose equivalents in non-uniform beam exposure would be depend on not only the beam intensity but also the beam size, beam position and other beam parameters.

In this study we have calculated the conversion factors in non-uniform beam exposure of high energy electrons in the energy range from 100 keV to 20 MeV, especially with regard to the beam size and beam position in AP exposure.

2. Mathematical Phantom

The mathematical anthropoid phantom used in this work is a hermaphrodite phantom and is derived from MIRD Pamphlet No.5 (revised). It has also Lewis' oesophagus. Fig.1 shows the anterior view of the MIRD phantom. The phantom consists of three types of tissue - lung, skeletal and other soft tissue. Elemental composition of different tissues of the phantom and their masses were determined by using the reference data. To obtain the effective dose absorbed dose calculation were made for bone, lungs, red bone marrow and every other organs to which the tissue weighting factors are assigned.

3. Monte Carlo Program and Model of Exposure

The EGS4 Monte Carlo Code originally developed at SLAC was used to calculate the energy deposition which was occurred through the transport of electrons, positrons, and photons in a mathematical human phantom. The EGS4 Code used in this work was slightly modified by adding the pre processor to simplify the input and output data.

Calculation were carried out for whole body exposure with monoenergetic electrons in the range of 0.1 to 20 MeV as well as non-uniform beam exposure, where the phantom is placed in a vacuum space in both type of exposure. The incident beam is square of 16.23 cm $\times$ 20.0 cm, which is as large as 1/10 of the region from shoulder to upper legs. The eight positions are irradiated on a body, 3 positions on the breast (right, left and center part of the breast), 3 on the abdomen and 1 on the neck and 1 on the ovary. Irradiation geometry is anterior-posterior(AP) for all beam exposures. Exposure positions on the

body are shown in Fig.1 where the beam size is also drawn. Fig.2(a) shows the geometry of uniform exposure on a whole body and Fig.2(b) shows the exposure positions and the smaller beam size to investigate the beam size effect.

4. Results and Discussion

4.1 Effective Dose per Unit Particle Fluence

The conversion factors defined as H_T, H_E or E per unit particle fluence were calculated by using the results of Monte Carlo Simulations. Fig.3 shows one of them for AP exposure on right side of the chest by the electron beam. For the case of exposure on chest, any remarkable differences in the conversion factors were observed in the change of an exposure position from right side of the chest to left side and center. This fact were also observed for the case of abdomen.

4.2 Uniform Exposure on a Whole Body and Non-Uniform Beam Exposure

To compare the effects of uniform exposure on a whole body with the non-uniform beam exposure on a part of a body, we calculated the effective doses in both exposures when the same number of electrons irradiated the phantom uniformly (Fig.2 (a)) and non uniformly (Fig.2(b)). The calculated result were shown in Fig.4. It has been shown that in the case of uniform exposure the effective dose increases rather smoothly with increasing the electron energy, while in the case of non-uniform exposure it increases rapidly from a certain energy depending on the exposure position, for example, from 10 MeV on the exposure on abdomen. This is due to the fact that the effective dose depends not only what organs are irradiated by the beam but where they locate in a body and what radiation weighting factors they have. To elucidate these phenomena, we have selected the organs which mainly contribute the effective dose in each exposure geometry. Fig.5 and Fig.6 show the percentages of the organ doses to the effective dose in the exposure on the chest and on the lower abdomen, respectively. It has been shown from Fig.5 that the percentage of skin dose is high at lower than 0.5 MeV while, from the 1 MeV, the percentage of breast dose is predominate, which indicates that the incident electrons of energy higher than 1 MeV begin to reach the breast and to deposit the energy on it. However, at higher than 7 MeV, the percentage of the breast dose begins to decrease. This is due to the fact that the electrons begin to reach the lung and its contribution increases. Similarly from Fig.6, it is seen that the contribution of urinary bladder increases from the energy higher than 10 MeV and the contribution of colon increases at 20 MeV. We have not investigated the effects above 20 MeV, but it would be not surprising if the effective dose above 20 MeV for the exposure of left side of the lower abdomen is higher than those for the exposure of

right side one became the colon locates left side of a body.

4.3 Dependence on the Beam Size

Figure 7 shows the effective dose which are obtained in the exposure of the chest in which the beam size is not only a unit one but also as small as 1/4 and 1/16, respectively(see Fig.2(b)). At the higher energy than 10 MeV, electrons become to reach the main organs located in abdomen of a body. Therefore, the effective dose in Fig.7 also reveals the difference due to the beam size at higher than 10 MeV. We need further calculations at much higher energy than 20 MeV to clarify the dependence of the effective dose on the beam size.

4.4 Comparison of the Effective Dose With and Without a Breast

Figure 8 has shown the effective dose with and without a breast when the right side of a chest was irradiated. Up to 0.5 MeV the most energy of an incident electron are deposited on a skin and at higher than 20 MeV a lung is the main organ to contribute to the effective dose. It is seen, therefore, that the remarkable effect with breast is eventually in the energy range of 1 MeV to 10 MeV.

Acknowledgments

The authors express deep appreciation to Dr. Y.Yamaguchi in Japan Atomic Energy Research Institute for his useful discus sion and Prof. H.Hirayama in National Laboratory for High Energy Physics for his kind help.

References

[1] ICRP Publication 51 (Annals of the ICRP Vol. 17 No. 2/3) *Data for Use in Protection Against External Radiation.*

[2] Y.Yamaguchi, *J. Nucl. Sci. Technol.*, **31**, 716 (1994). *ibid* **31**, 821 (1994).

[3] W.R.Nelson, H.Hirayama and D.W.O.Rogers, *The EGS4 Code System*, SLAC-265.

[4] T.Momose, et. al., *Improvement in the EGS4 code system - general purpose electron-photon Monte Carlo transport code system*, Proceeding of the First EGS4 User's Meeting in Japan.

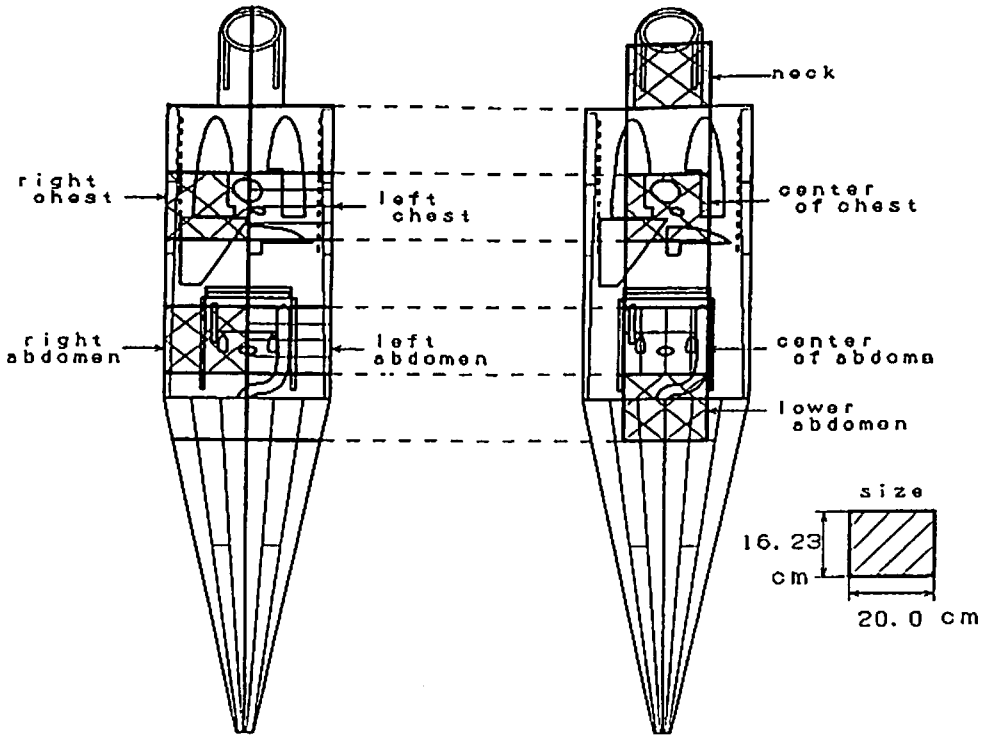

Fig.1 Anterior view of the MIRD Phantom
and the geometories of non uniform beam exposure

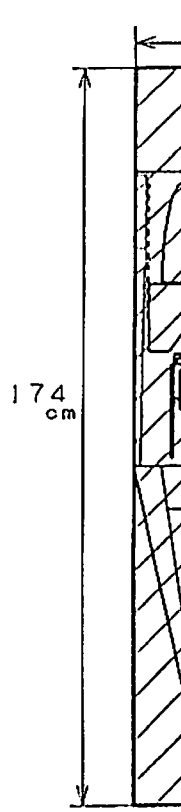

Fig.2(a) Geometory of uniform exposure on a whole body

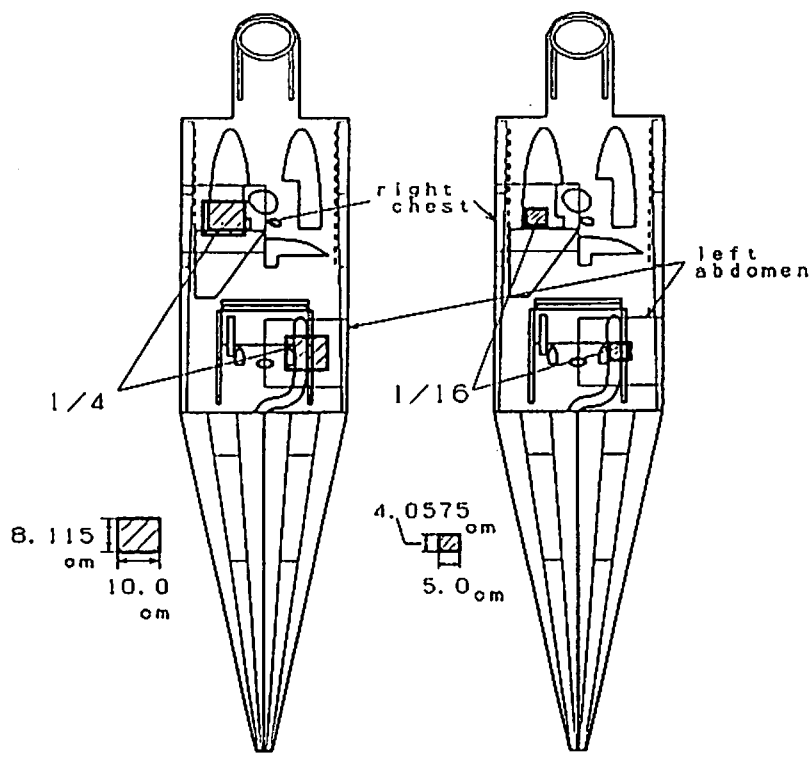

Fig.2(b) Exposure positions and the smaller size to investigete the beam size effect

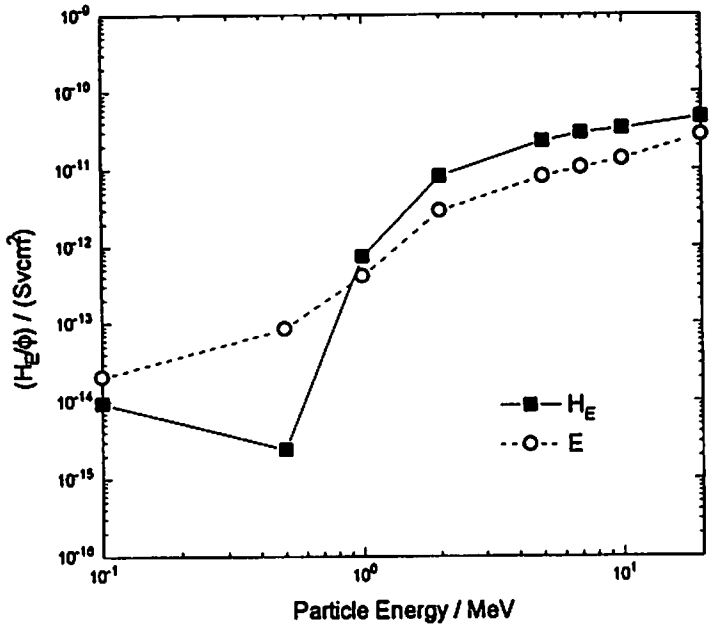

Fig.3 H_E and E per unit fluence for the non uniform beam exposure on the right side of the chest

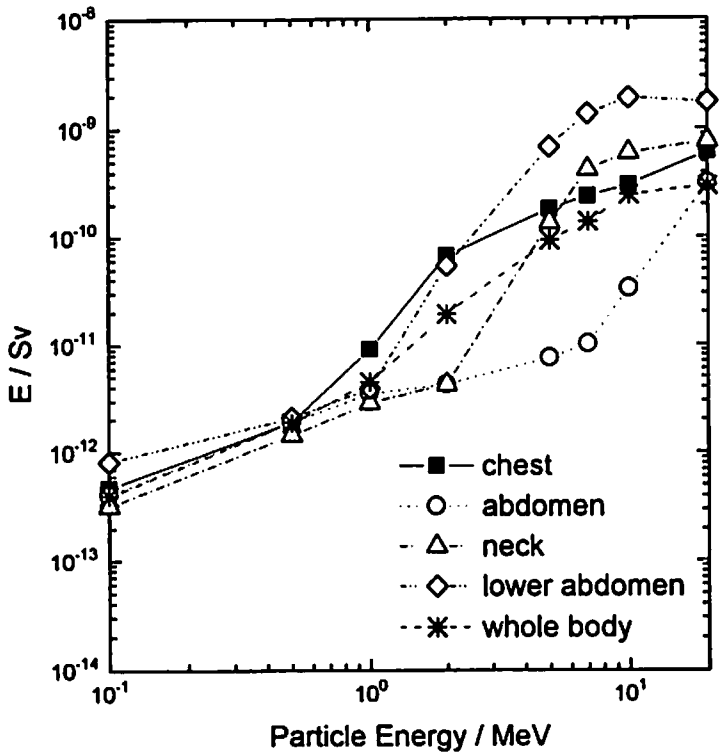

Fig.4 Effective doses for non uniform beam exposure on several parts of the body

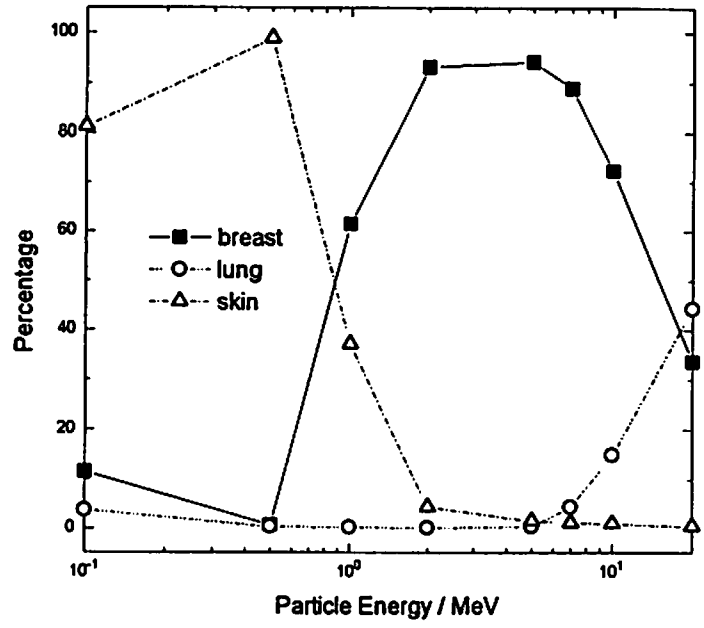

Fig.5 Percentage of organ dose to the effective dose in the case of exposure on the chest

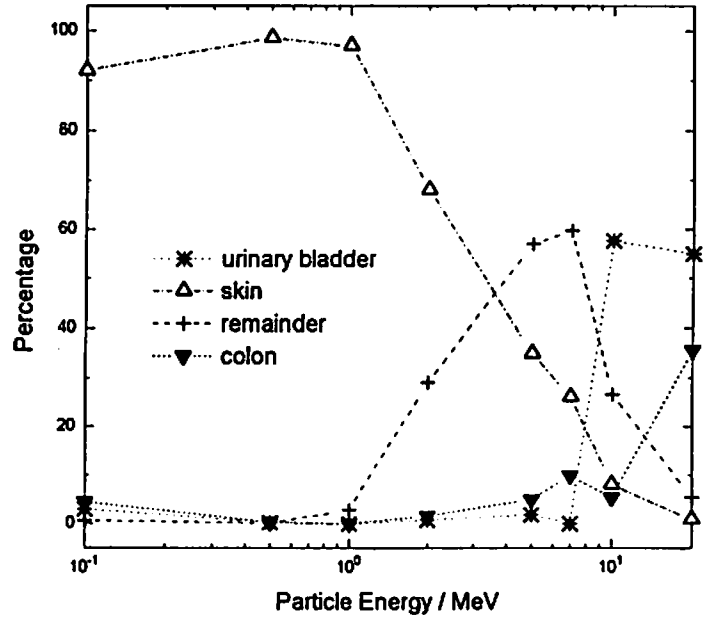

Fig.6 Percentage of organ dose to the effective dose in the case of exposure on the abdomen

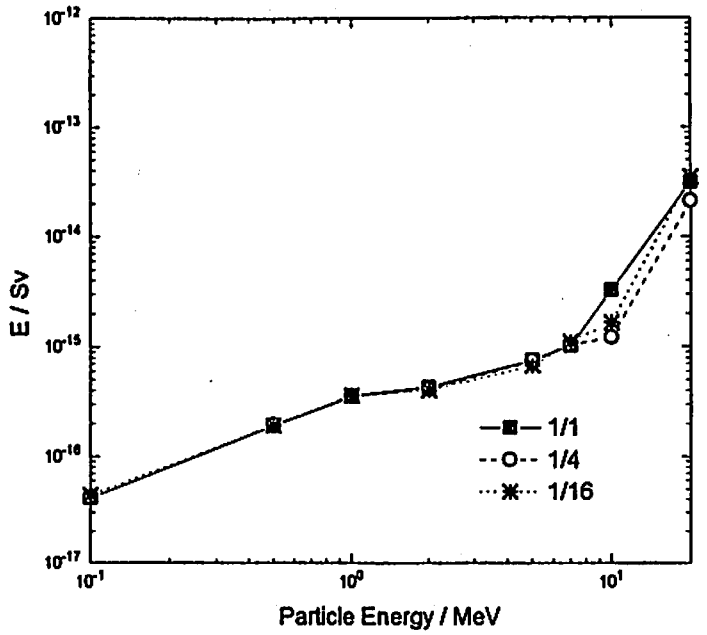

Fig.7 Effective dose for the beam exposure with different beam size (in the case of exposure on the left abdomen)

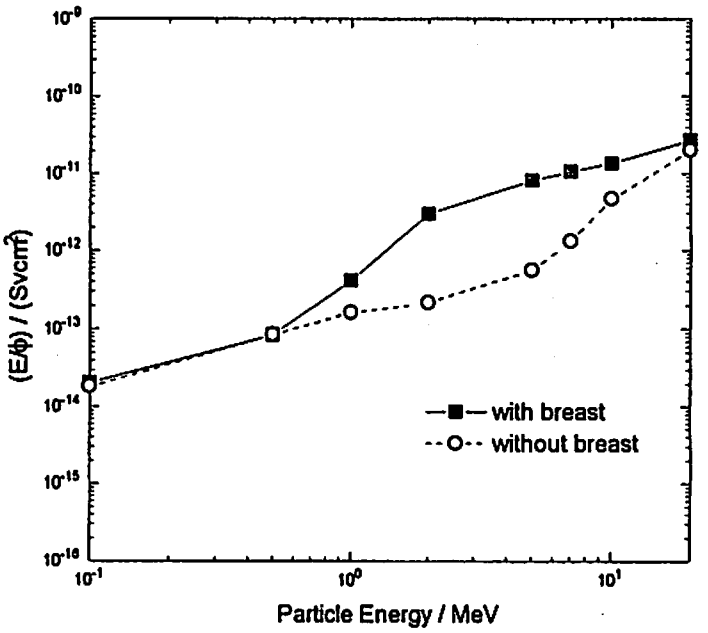

Fig.8 Effective dose with and without the breast

DESIGN OF MULTI-CHANNEL MODERATOR ASSEMBLIES FOR THE POSITRON FACTORY

H .KANEKO, S .OKADA and S .MASUNO

Takasaki Establishment,
Japan Atomic Energy Research Institute
Watanuki-machi 1233, Takasaki, Gunma 370-12, Japan

Abstract

By using a Monte Carlo simulation system, we evaluated slow positron yields in multi-channel moderator assemblies which are applied for linac-based slow positron generation. Combinations of tungsten moderator foils with various thicknesses were tested.

As far as the calculation result was concerned, the yield was maximum when the thickness was selected to be 25 μ m for all the moderator foils. A certain increase in the yield might be expected by a minor modification.

1. Introduction

The Japan Atomic Energy Research Institute, JAERI, has been promoting design studies for the Positron Factory[1], in which linac-based intense monoenergetic positron beams are planned to be applied for advanced materials characterization and new fields of basic research. A tentative goal of the beam intensity is 1010 s-1, which is assumed to be realized with an electron linac of 100 kW class with a beam energy around 100 to 150 MeV.

We have proposed a new concept of the target system from which multi-channel slow positron beams can be simultaneously extracted by using multiple moderator assemblies. A possibility of the multi-channel slow positron beam extraction has been confirmed by a demonstrative experiment[2]. In this work, we further investigated an optimum configuration of the moderator assemblies by using a Monte Carlo simulation.

2. Calculation Method

We used a Monte Carlo simulation system EGS4-SPG developed by us[3] for evaluation of the slow positron yield. In this system, the behavior of positrons with energies more

than a cut-off is traced using EGS4[4] and the calculation is switched to SPG[1] when positrons are slowed down under the cut-off.

In Fig.1 is shown a configuration of the target system which was used in the demonstrative experiment previously mentioned. The moderator part was a set of 2 channel moderator assemblies. The set was composed of 18 tungsten foil layers of 25 μ m in thickness. Slow positrons from each 9 layers were separately extracted as 2 channel beams by 2 tungsten mesh grids. Each moderator layer was divided into 3 parts, electrically separated and biased to drift emitted slow positrons by sloping the electric field toward the extraction grids. The observed intensity of slow positrons from the second channel, which was distant from the converter, was smaller only by an order of magnitude than that from the first channel, which agreed well with the simulation result with EGS4-SPG[2].

The same moderator configuration as the above was assumed in the calculation, by which we intended to find out whether a more efficient combination of the moderator foil thicknesses exists or not. We evaluated the slow positron yields for a variety of combinations of the thicknesses. Here, the yield means a ratio of the number of slow positrons to that of energetic positrons and photons injected perpendicularly onto the center of the first layer in the first moderator assembly. The tested incident energies were ranging from 0.25 to 5 MeV for positrons and from 1.5 to 5 Mev for photons, respectively.

3. Result and Discussion

The calculation result of the slow positron yields from the first and the second moderator assembly is shown in Fig.2, for the respective injection of energetic positrons and photons. In the calculation, 18 moderator foil layers were divided into 3 blocks composed of 6 layers of the same thickness. In the figure, for example, 'W.2-2-25' represents that the foil thicknesses are 2 μ m in the first block (nearest to the converter or the positron and photon injection point), 2 μ m in the second and 25 μ m in the third.

In conclusion, as far as the calculation result is concerned, it seems that the selection in the demonstrative experiment was correct, in which the thickness was selected to be 25 μ m for all the moderator foils. Because the slow positron yields from photons are much larger than the other configurations. Here, we took into account another calculation result[2] that the number of energetic photons are several orders larger than that of energetic positrons emitted from the converter onto which a 100 MeV electron beam bombards. In case of this configuration, however, Fig.2 also indicates that comparatively low energy positrons are not efficiently converted to slow positrons in the first assembly and the slow positron yields from energetic positrons in the second assembly are smaller than the other configurations. A certain increase in the yield might be expected by a minor modification. We will further try a detailed calculation, taking into account energy

and angular distributions of positrons and photons from the converter.

References

[1] S .Okada and H .Sunaga, Nucl. Instr. Meth. **B56/57** 604-609(1991).

[2] S .Okada et. al., 10th Symp. on Accelerator Science and Technology (Hitachinaka, Oct. 1995).

[3] S .Okada and H .Kaneko, Applied Surface Science **85**, 149-153(1995).

[4] W .R .Nelson, H. Hirayama and D. W. O. Rogers, SLAC-265(1985).

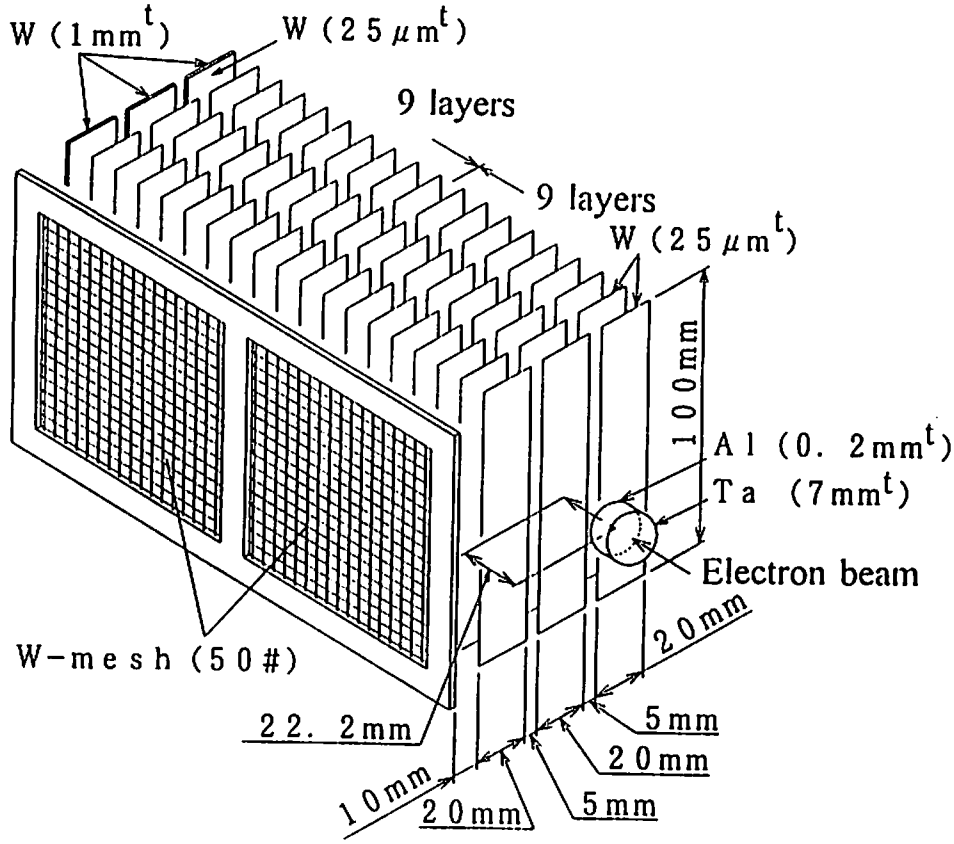

Fig.1 Geometry of 2 channel moderator assemblies.

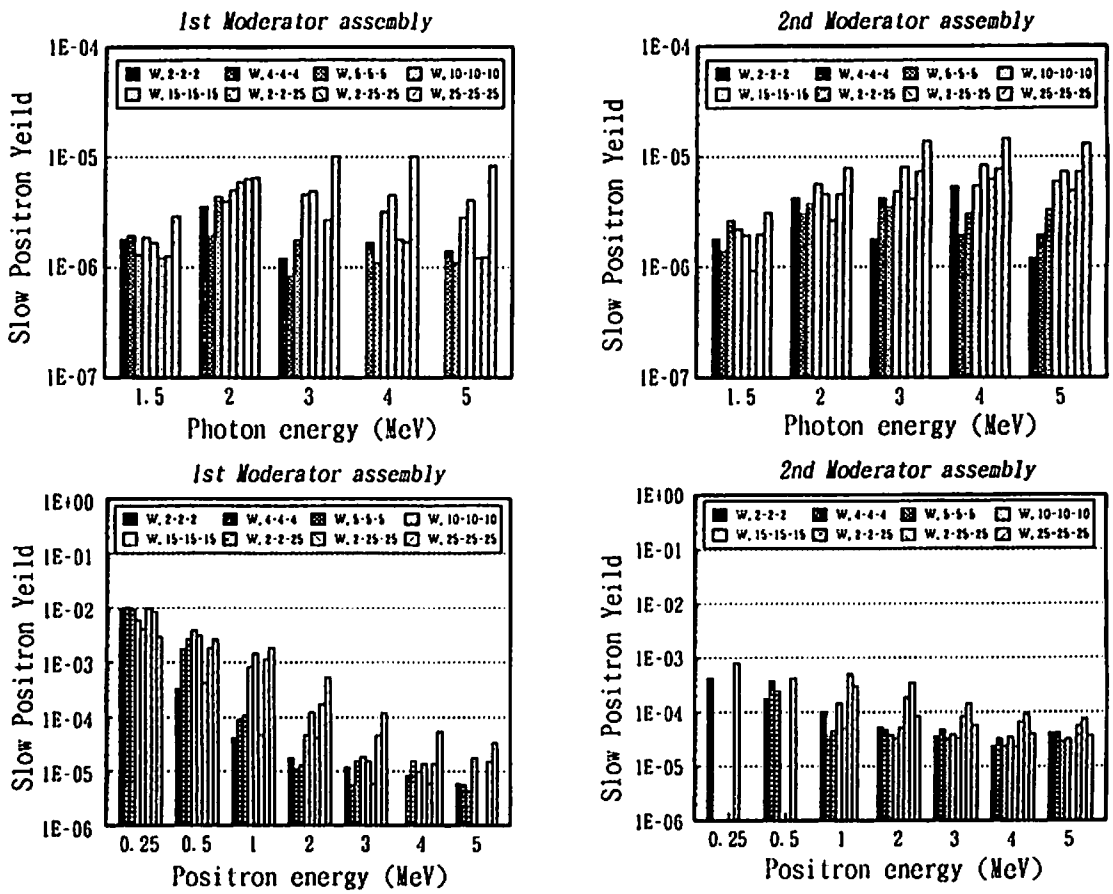

Fig.2 Calculation result.

DESIGN OF A SELF SHIELD TYPE SLOW POSITRON SOURCE USING AN ISOTOPE

S .MASUNO, H .KANEKO and S .OKADA

Japan Atomic Energy Research Institute
Takasaki Radiation Chemistry Research Establishment
Watanuki-machi 1233, Takasaki, Gunma 370-12, Japan

Abstract

We have been constructing an electrostatically transported slow positron beam line for depth profiling of ion-induced defects and others. If a usual shielding was applied, the size of the equipment would become too large in order to reduce γ-rays from a positron-emitting isotope which reach the sample. We performed design calculations for a structure of a compact and efficient slow positron source.

1. Introduction

In case of a slow positron beam extraction using an isotope, the isotope emits positrons to 4π-direction by β^+ disintegration, which have a wide energy distribution. Positrons emitted within a certain solid angle, which enter a neighboring material, are thermalized and start to diffuse. If an adequate material like tungsten is selected, a part of thermalized positrons escaping from annihilation are reemitted from the surface by the negative surface potential for positrons. Such a material and a group of the reemitted positrons are called a moderator and a slow positron beam, respectively.

The slow positron beam has a narrow energy and angular distribution. By acceleration, a monoenergetic positron beam can be obtained. On the basis of this principle, we have been constructing a variable energy positron beam line as shown in Fig.1, which is electrostatically transported, for the purpose of depth profiling of ion-induced defects and others. The tungsten foils work as moderators. Slow positrons reemitted from the tungsten foils are electrically extracted to the right hand direction in the figure. In order to increase the slow positron yield, it is more efficient to put the isotope nearer to the moderator. If the isotope was attached to the moderator foil, it would be most efficient. In this case, however, gamma rays from the isotope go straightforward in the same direction as the slow positron beam. It is necessary to deflect the positron beam in order

to prevent the gamma rays from hitting a sample. This results in enlarging the size of the outer shield and also the equipment itself. If the isotope is placed distant from the moderator and surrounded with the outer shield, on the other hand, the slow positron yield is reduced.

We carried out Monte Carlo calculations to find out an optimal shield structure, in which internal shields work as a collimator and a reflector.

2. Calculation Procedure

For the Monte Carlo calculations, we used EGS4-SPG[1], in which the behavior of positrons with energies more than a cut-off is traced using EGS4 [2] and the calculation is switched to SPG[3] when positrons are slowed down under the cut-off.

We compared the slow positron yields calculated with the EGS4-SPG for the following three structures.

1) No collimation structure (Fig.2): It has only an outer shield.

2) Collimation structure (Fig.3): The positron emitter is placed at the bottom of a cylindrical hole in a cylindrical collimator. We selected tungsten for the collimator material, taking into account that it is good for shield, sufficiently hard for scattering and suitable for use in vacuum.

3) Collimation structure with a reflector (Fig.4): A tungsten reflector is added to the above structure, in order to reflect positrons which do not enter the moderator foils and also those which pass through the foils.

We assumed a ^{22}Na point source of 370 MBq in activity as the positron emitter. In the calculations, 50, 100, 200, 300, 400 and 500 keV were selected for the energies of positrons emitted from the source because positrons from ^{22}Na have an energy distribution ranging from 0 to 546 keV. The moderator assembly was composed of four tungsten foils of 25μm in thickness and $1cm \times 1cm$ in width. The distances from the source to the nearest moderator foil were selected to be 0cm (attached), 1.4 cm, 2.4 cm, 5.4 cm and 10.4 cm.

To evaluate the slow positron yields, it would be better to trace the positron behavior until the reemission. However, it would require huge calculation time. We evaluated the thermalized positron yields in place of the slow positron ones. It had already been calculated with the SPG that a ratio of the number of reemitted positrons to that of thermalized positrons uniformly distributed in a tungsten foil of 25μm in thickness is 5.0×10^{-3} distribution is not uniform when positrons with comparatively low energies enter the foil, we used the thermalized positron yields for the purpose of relative comparison

among various shield structures.

3. Result and Discussion

3.1 Collimation Effect

Thermalized positron yields calculated for various structures and different positron energies are shown in Table 1. In case of no collimation structure (Fig.2), about 20% positrons among all β^+'s are thermalized when the emitter is attached to the nearest tungsten foil (Region 1). If the emitter is 1.4 cm distant from the nearest foil, the yields are reduced to about 1/10. The yields decrease with the increasing distance.

In case of the collimation structure (Fig.3), on the other hand, the yields are 3 or 4 times larger than the no collimation structure. The collimation effect is remarkable as shown in Fig.5. The tracking of positrons is demonstrated in Fig.6 for a collimation structure where the emitter is 1.4 cm distant from the nearest foil. It is obvious that positrons, which otherwise would fly away from the moderator foils, are scattered by the collimator wall and enter the foils.

3.2 Reflection effect

When a tungsten reflector is added to the collimation structure, the yields increase by 10 or 20% in case the distances between the emitter and the nearest foil are 1.4 cm and 2.4 cm. No reflection effect is found if the distance are larger.

The reflection effect is not so remarkable as the collimation one. It is assumed that a large part of positrons do not have sufficient energy for back-scattering because they lose the energy by the collimation. However, it is concluded that the reflector is useful because it has a shielding effect as well as a small but positive reflection effect.

3.3 Shield effect

Dose rates at the point of 1 m apart from the moderator foils in the direction of the slow positron extraction were evaluated, taking 1.275 MeV γ-rays from ^{22}Na into account. In case of no shield (Fig.2), the dose rate was 64.5 μSv/hr. If the collimation structure with a reflector (Fig.4) was applied, the dose rate was 8.97μSv/hr in case the distance between the emitter and the nearest moderat or foil was 1.4 cm. It is concluded that the harmful radiation can be reduced to 1/7 by placing the emitter at the point of only 1 cm apart from the aperture inside the collimator.

4. Conclusion

We performed Monte Carlo calculations for design of the structure surrounding the

positron emitter in an electrostatically transported slow positron beam line which is now being constructed. When the emitter was inserted into a cylindrical tungsten collimator and the distance between the emitter and the nearest tungsten moderator foil among the four foils of 25 μm in thickness surround ed with a tungsten reflector was 1.4 cm, the thermalized positron yield was about 40% of that in case the emitter was attached to the nearest foil. It was concluded that the collimation structure with a reflector is efficient because effects of collimation, reflection and shield are simultaneously expected and a compact design is possible.

We will further investigate the optimal structure by calculations and experiments.

References

[1] S .Okada and H .Kaneko, Applied Surface Science **85**, 149-153(1995).

[2] W .R .Nelson, H .Hirayama and D .W .O .Rogers, *The EGS4 Code System*, SLAC Report 265 (1985).

[3] S .Okada and H .Sunaga, Nucl. Instrum. Meth. B **56/57**, 604-609(1991).

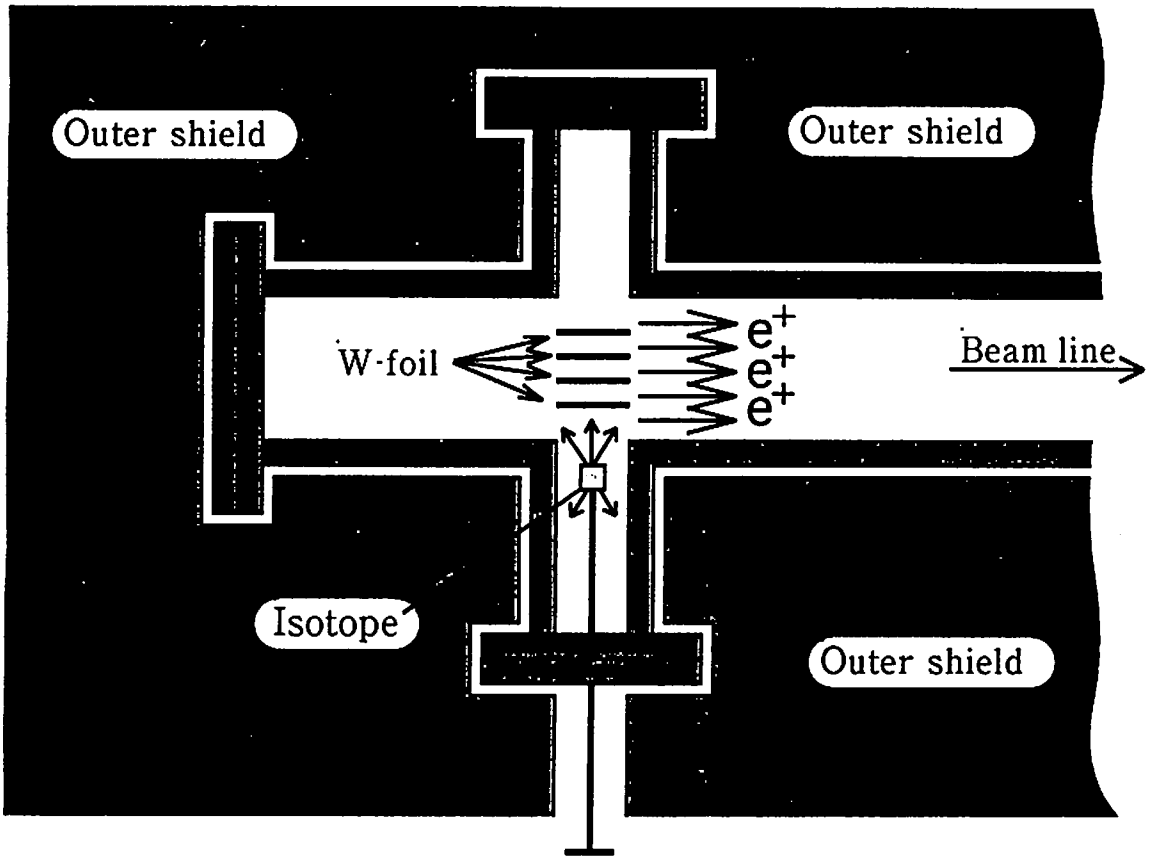

Fig.1 Schematics of a slow positron beam line.

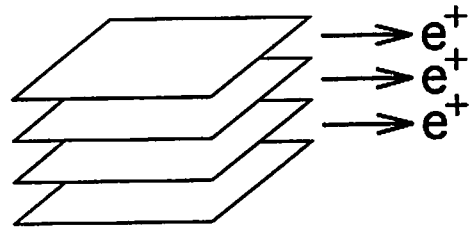

Slow positrons reemitted from tungsten foils
are extracted to the direction of arrows.

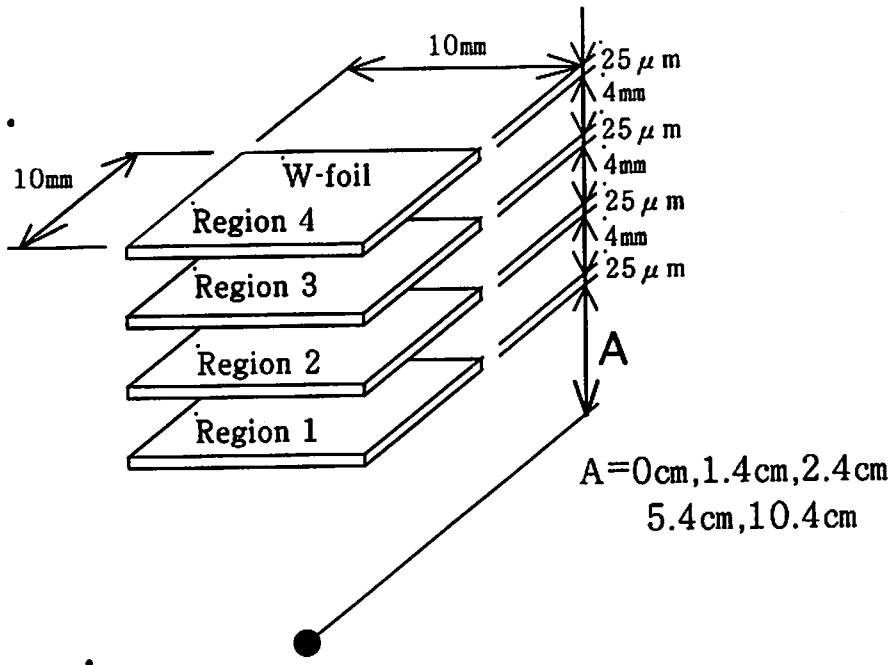

A=0cm,1.4cm,2.4cm
5.4cm,10.4cm

Disk form e+source (0.5 cm ϕ active area)

⇩

Considered as a point source

{ 4 π -direction emission
{ Energy 50,100,200,300,400,500keV

Fig.2 Calculation model of the no collimation structure.

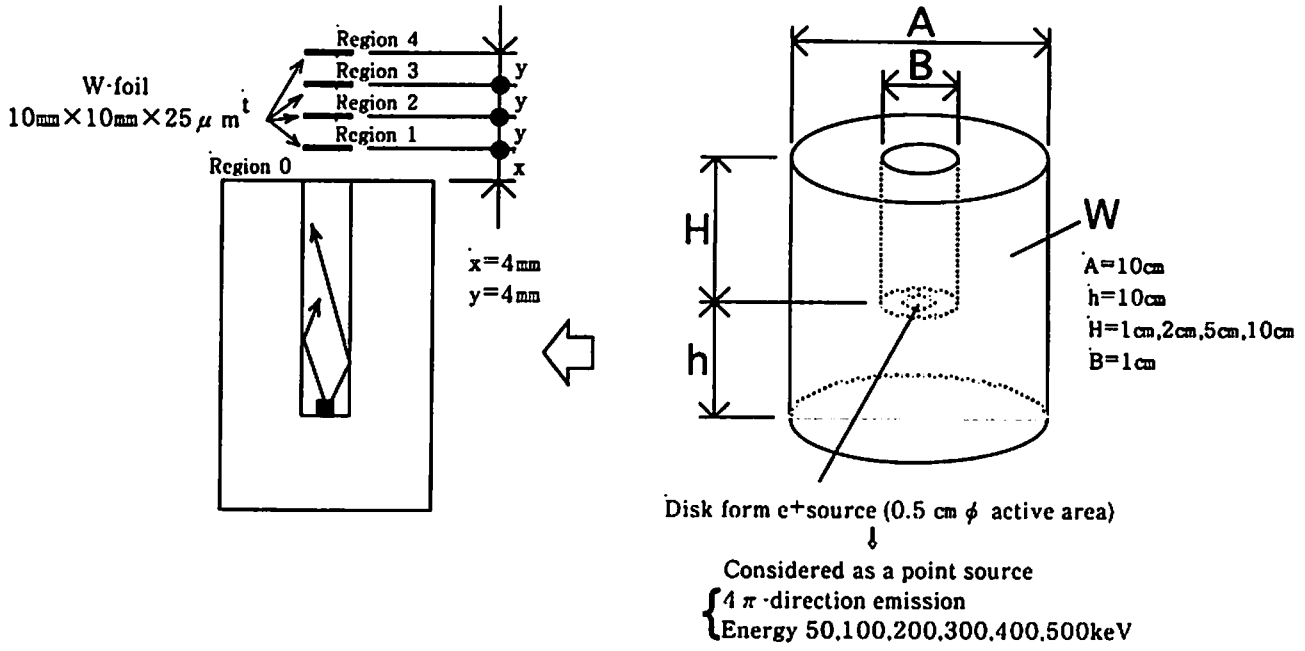

Fig.3 Calculation model of the collimation structure.

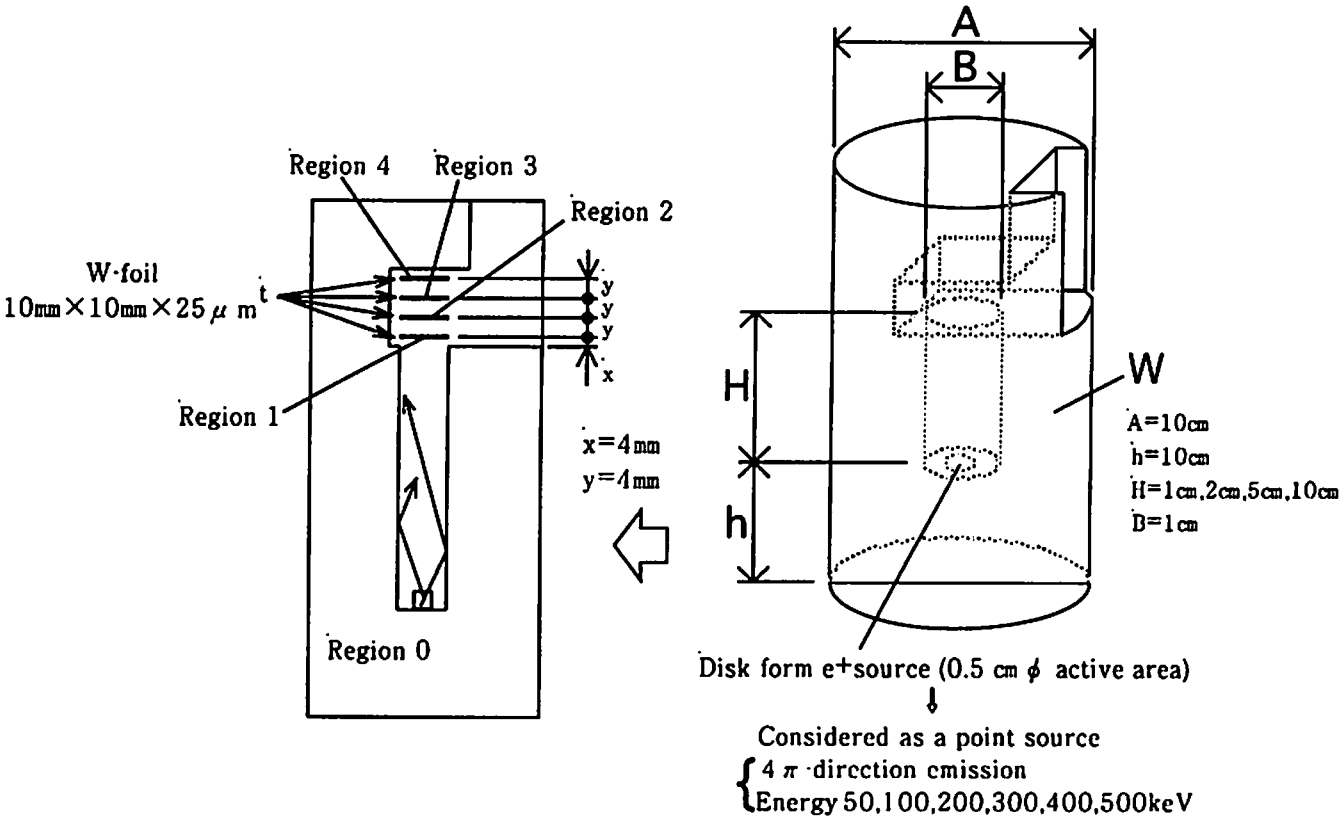

Fig.4 Calculation model of the collimation structure with a reflector.

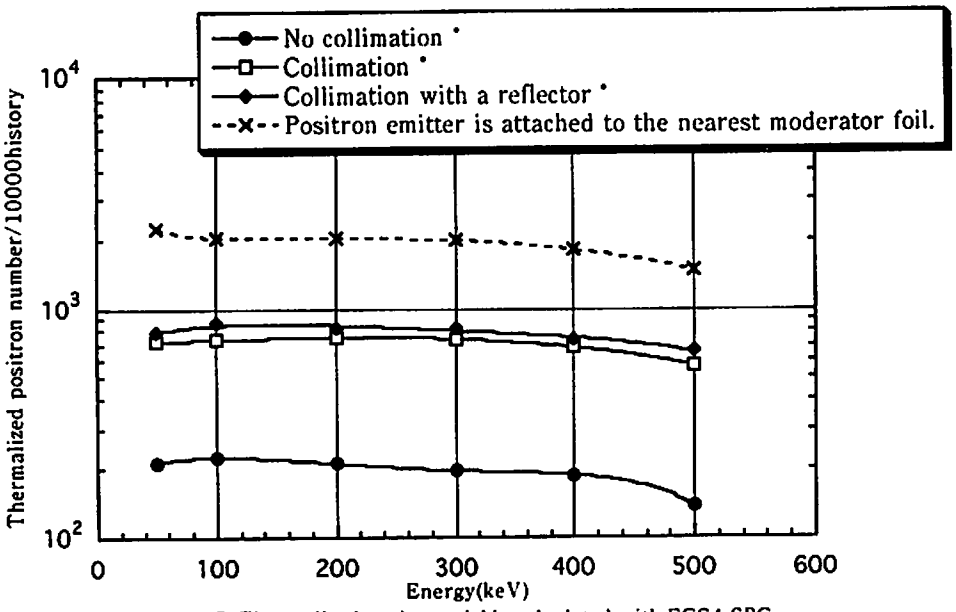

Fig5. Thermalized positron yields calculated with EGS4-SPG.
*: The distance between the positron emitter and the nearest moderator foil is 1.4 cm.

	*Isotope position	Thermalized positron/ $\beta+$(%)					
		Positron ($\beta+$) energy					
		50keV	100keV	200keV	300keV	400keV	500keV
No Collimation	0cm	22.2	20.2	20.2	19.9	18.1	14.7
	1.4cm	2.14	2.24	2.12	1.96	1.88	1.37
	2.4cm	0.88	0.82	0.73	0.66	0.62	0.58
	5.4cm	0.16	0.17	0.18	0.20	0.17	0.08
	10.4cm	0.02	0.05	0.04	0.01	0.01	0.03
Collimation	1.4cm	7.19	7.33	7.49	7.38	6.79	5.64
	2.4cm	2.97	3.03	3.00	2.87	2.85	2.76
	5.4cm	0.47	0.46	0.47	0.49	0.53	0.46
	10.4cm	0.09	0.09	0.10	0.12	0.12	0.07
Collimation with Reflector	1.4cm	7.85	8.65	8.16	8.27	7.36	6.51
	2.4cm	3.09	3.53	3.36	3.20	3.16	2.81
	5.4cm	0.47	0.48	0.49	0.55	0.54	0.45
	10.4cm	0.09	0.09	0.09	0.11	0.12	0.08

* : distance between the positron emitter and the nearest moderator foil

Table 1 . Thermalized positron yields calculated with EGS4-SPG for various structures.

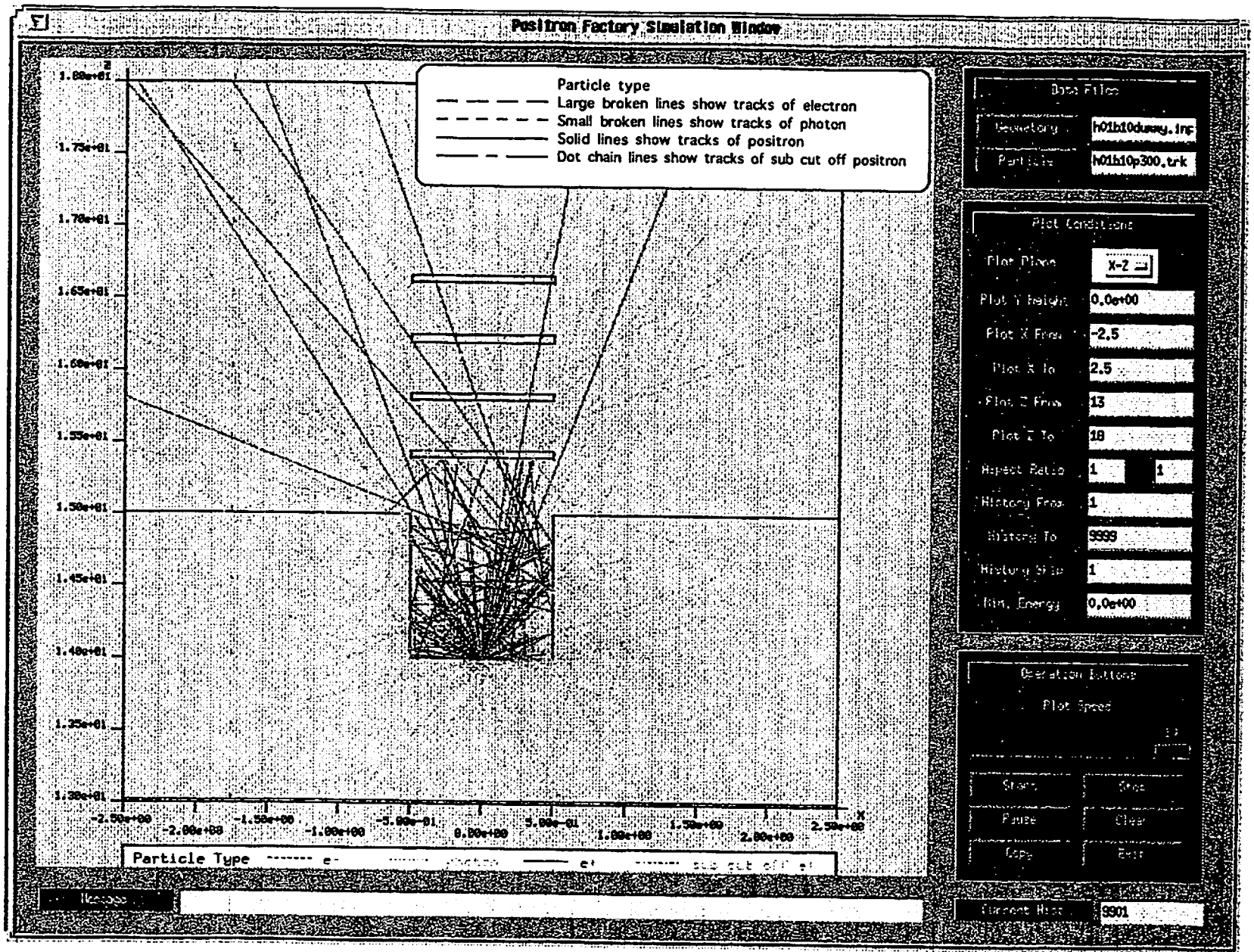

Fig.6 Tracking of 300 keV positrons for a collimation structure where the emitter is 1.4 cm distant from the nearest foil.

CALCULATION OF ENERGETIC POSITRON BEAM PRODUCED FROM A 45MeV LINAC

N. NIIKAWA, F. FUJITA, M. KITAICHI and S. SAWAMURA

Department of Nuclear Engineering, Hokkaido University
Kita-13, Nishi-8, Kita-ku, Sapporo, 060, Japan

I. NOJIRI

Power Reactor and Nuclear Fuel Development Corporation
Tokai-mura, Naka-gun, Ibaraki-ken, 319-11, Japan

Abstract

On the basis of a help of Monte Carlo Simulation Code EGS4, we calculated the yields of bremsstrahlung X-rays which was essential to produce the positron beam. We also calculated the yield of monoenergetic gamma photon formed by the annihilation of a fast positron as well as positronium. The simulation has shown that the yield of the bremsstrahlung increases in high Z materials. In the case of Pt, the yield is the largest at near of one radiation length and the total energy of bremsstrahlung amounts to about 8 MeV per incident electron of 45 MeV. The yield of the positron becomes maximum at near of 1.5 radiation length, in the case of Ta target, and the calculation shows that 6×10^8 positrons are produced by one pulse from the linac installed at Hokkaido University. Moreover, it is seen that thin Be target is available to yield the monoenergetic annihilation gamma which is one of the applications of fast positrons.

1. Introduction

Recent progress in accelerator engineering bring electron linac high efficiency and high quality. In addition to previous applications of electron linac in X-ray and neutrons, the progress in beam intensity and beam energy make it possible to use the positrons as a new tertiary particles produced from electrons[1]. A positron is formed from a bremsstrahlung by pair production reaction. Intensive positron source is very useful to develop a new science. Fast positrons are also helpful to produce a monoenergetic gamma photons of which energy is higher than those obtained from gamma photons emitted by the disintegration of isotopes.

On this study, we simulate the transport process of electrons, photons and positrons by using the EGS4 Monte Carlo code[2]. And calculate the yield of bremsstrahlung,

annihilation gamma and energetic positron in various material target and production of monoenergetic gamma-ray caused by annihilation of energetic positron in beryllium[3]. Preliminary experiment of detecting the annihilation gamma is also carried out.

2. Calculation of Bremsstrahlung Production

2.1 Calculational Geometry

Knowledge of the bremsstrahlung spectra are essential to produce positrons through pair production using a high energy linac. The extremely high intensity of photon beams for the production of positrons makes direct measurement of energy spectra virtually impossible.

In this work, we use the Monte Carlo method to simulate the energy spectra and angular distribution of photon beams produced by linear accelerators.

Figure 1 shows a calculational geometry of the simulation. Energy of an electron from a linac installed at Hokkaido University is 45 MeV. According to the real beam size and its shape 45 MeV electron source of the simulation is selected to be a circle of 2.5 mm radius. Calculations are performed for the targets made of lead, tungsten, platinum, iron and aluminum, whose thickness are 0.1, 1, 3 and 5 radiation length.

The energy spectrum is recorded in a plane of 2.5 cm square detector placed just behind the target.

2.2 Results

Figure 2 shows the spectra of bremsstrahlung produced by bombarding a Pb target with a 45 MeV electron beam. Simulation was performed with the target thickness of 0.1, 1, 3 and 5 radiation length, and the photons which was emitted to the forward direction from the target was scored. In Fig.2, the intensity of the spectrum at the higher energy region decreases while it increases at the lower energy region as the target becomes thick. It indicates that the interaction of a photon in the same target occurred heavily in a thick target. Figure 3 shows the total energy carried away to the forward direction by the photons escaped from the target. It is seen that the total energy is the largest at near of one radiation length and it amounts to about 4 MeV per incident electron of 45 MeV. We carried out the same calculation to the several target materials such as Al, Fe, W and Pt, and found that the amount of total energy become larger as atomic number of target material increase. For example, the total energy amounts to 8 MeV for Pt of one radiation length, which is nearly the double amount in comparison with these of Pb. Moreover , when a target is bombarded by a 45 MeV electron beam, the simulation shows that not only the bremsstrahlung but also the monoenergetic gamma photons by the annihiration of slow positron in the same target are emitted. Figure 4 is the spectrum including the

annihilation gamma at 0.511 MeV. This peak was confirmed by our preriminaty experiment using the gated counting method to the pulsed radiation (fig.5). The criff appeared near 100keV on the spectrum in fig.4 is due to the absorption of K shell of Pb.

3. Calculation of Energetic Positron Production

3.1 Calculational Geometry

Fig.6 shows a calculational geometry to investigate the yield of positrons from various materials. An electron source is circus of 2.5 mm radius placed in front of target. From this source, electrons perpendicularly enter into the target. The target is a semi-infinite slab of 6 radiation length. Materials of targets are aluminum, iron, cupper, silver, tantalum, tungsten, platinum, gold and lead. The planes of surface detectors in the slab are located at the thickness of 0.5, 1, 1.5, 2, 3 and 4 radiation length from the surface. The number of positrons passing through the detector toward its normal direction are recorded by the detectors as a function of its angle and energy.

3.2 Results

The number of positrons produced by bombarding a target with a 45 MeV electron depends on the atomic number Z of target material. Figure 7 shows the dependence of positron yield on atomic number Z. Thickness of all targets used in the calculation is 1.5 radiation length. The simulation has shown that the yield of the positron increases as the atomic number becomes high, but it shows the satulation at higher than Ta. The calculation shows that 1.5×10^{-2} positrons are produced by a 45 MeV electron in the positron energy range of 0.1 to 20 MeV. It corresponds to 6×10^{8} positrons per one pulse from the linac installed at Hokkaido University.

4. Calculation of Annihilation Gamma-ray Production

4.1 Calculational Geometry

Figure 8 shows the geometry in EGS4 calculation of the spectrum of photons emitted by the annihilation of a fast positron. Cylindlical detector assembly extending perpendicularly into the positron beam axis, which is consists of 4 sub-cylindical detectors of radius 5.3 cm with different length, was employed. The photons passing through the lateral area of each sub-cylinder were scored. A fast positron was injected perpendicularly onto the Be target. In this geometry, photons which are emitted from the target within the angle

$\theta = 10°$ to $\theta = 13°$ will be scored by the forth sub-cylindlical detector.

4.2 Results

Figure 9 shows the spectra of photons produced by 5 MeV positron bomberding 0.5 mm Be target.The spectra are composed of two components ; one is a peak and another is the slope.The peak is consist of annihilation gamma photons and the slope is the bremsstrahlung produced by the positron slowing down in the Be target. It is found in Fig.9 that the intensity and the half width of each peak is depend on the detector, the emitting angle θ in Fig.8. The spectrum obtained in fourth detector is most sharp. Figure 9 salso shows that the conversion factor of a 5 MeV positron to an annihilation gamma photon emitted within the angle of 10° to 13° for 0.5 mm Be target is about 2×10^{-4}. The same calculation for a 10 MeV positron shows the comversion factor is 5×10^{-5}.

We have also calculated the conversion factor of a fast positron to an annihilation gamma for Be target of thickness 0.5 , 1, 1.5 mm. From the calculation, the conversion factor in thick target is larger than those in thin target. However, the intensity of bremsstrhlung due to slowing down the same positron become large the thick target is used. Therefore, we need some ways to surpress of bremsstrahlung to use the monoenergetic gamma.

5. Conclusions

To expand the applicaiton of intensitive high energy elevtron beam from linac, using EGS4 Monte Carlo Code, we have calculated the yield of secondry and tertial particles such as bremsstrahlung, positrons and annihilaiton gamma photons.

The calculation shows that the linac installed at Hokkaido University has a possibility to produce a considerable intensitive positron source. We need further investigation to show the availability of monoenergetic gamma photon produced by a fast positron annihilation.

References

[1] H. Tanaka and T. Nakanishi, *Slow positron production using an 18 MeV electron linac* , Nucl. Instr. and Meth. B62, 259-263 (1991).

[2] W.R. Nelson, H.Hirayama and D.W.O. Rogers, *The EGS4 Code System*, SLAC-265 (1985).

[3] S.S. Dietrich and B.L. Berman, *Atlas of Photoneutron Cross Sections Obtained with Mono energetic Photons*, UCRL-94820 (1986).

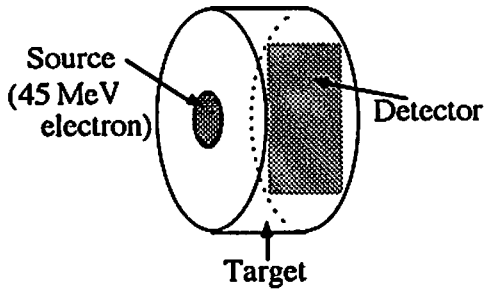

Fig. 1 Geometry of the Monte Carlo calculation of bremsstrahlung

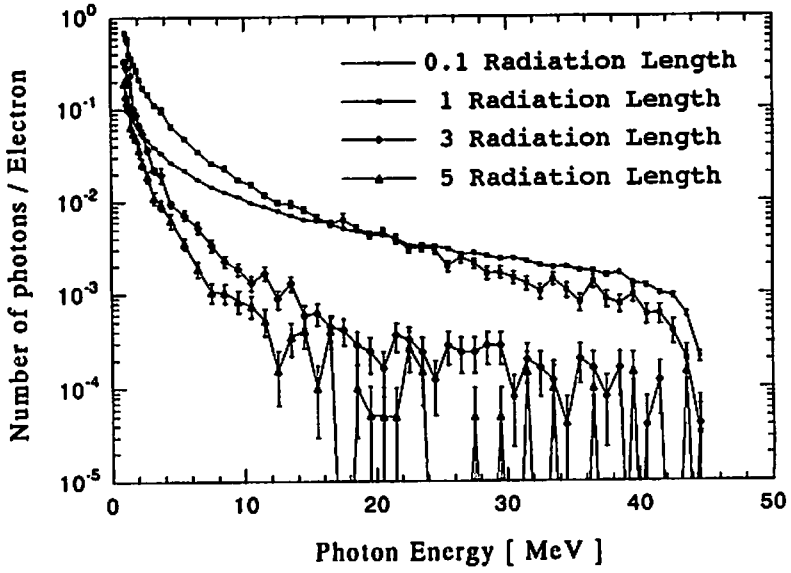

Fig. 2 Spectra of bremsstrahlung; target is lead, incident energy of electron is 45 MeV

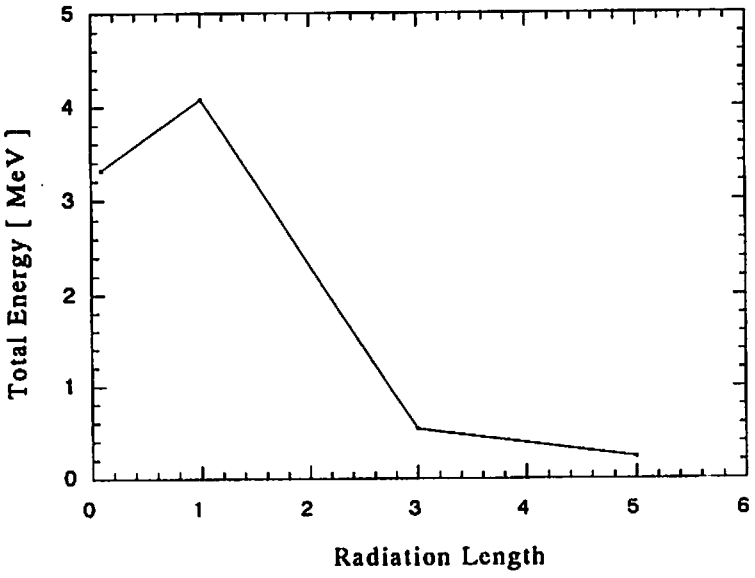

Fig. 3 Total energy of photon escaped from target; target is lead, incident energy of electron is 45 MeV

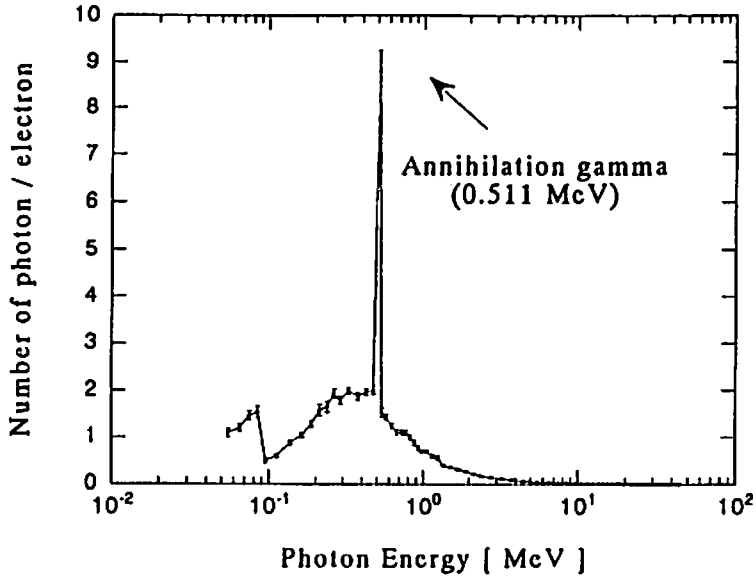

Fig. 4 Spectrum including annihilation gamma; target is Pb, thickness of the target is one radiation length , incident energy of electron is 45 MeV.

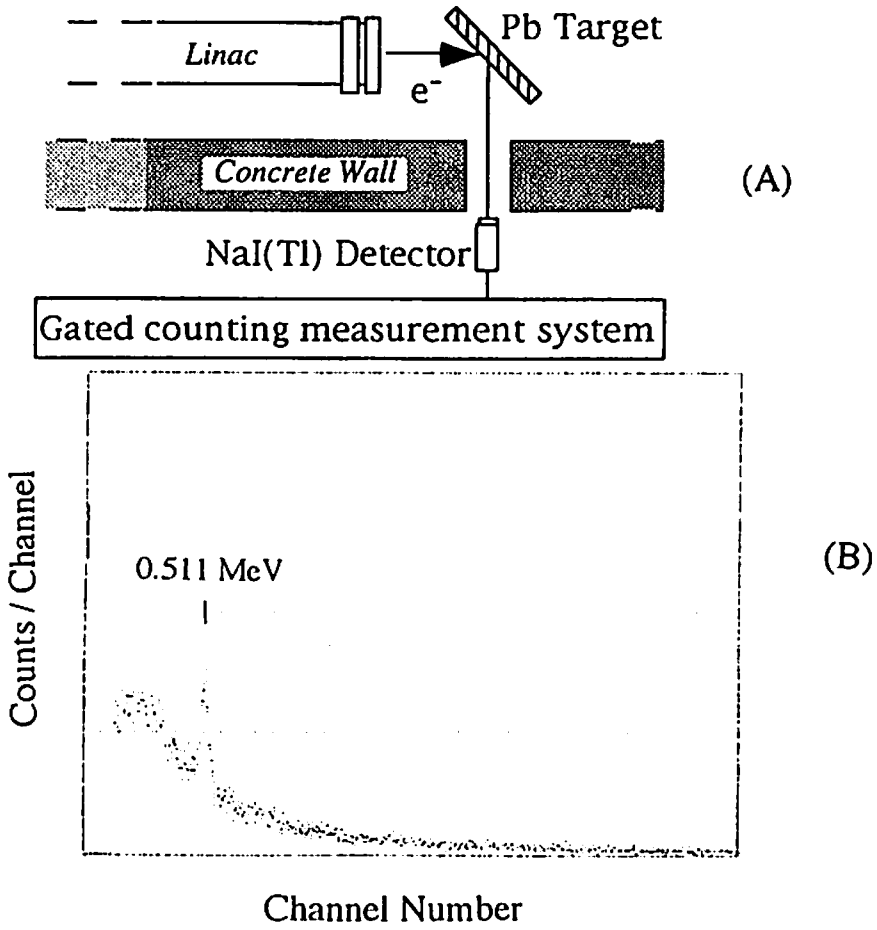

Fig. 5 (A) : Arrangement of the gated couting system for pulsed radiation
(B) : Pulse hight distribution obtained NaI(Tl) detector is the measurement of the pulsed radation

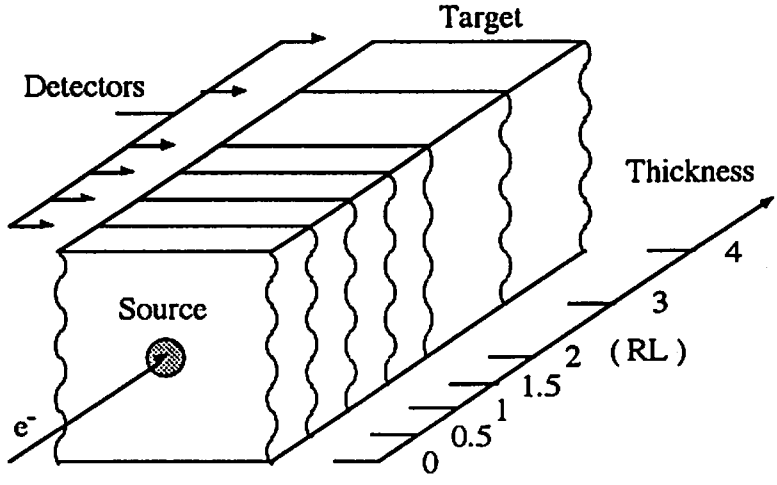

Fig. 6 Geometry of the Monte Carlo calculation of the positron yield

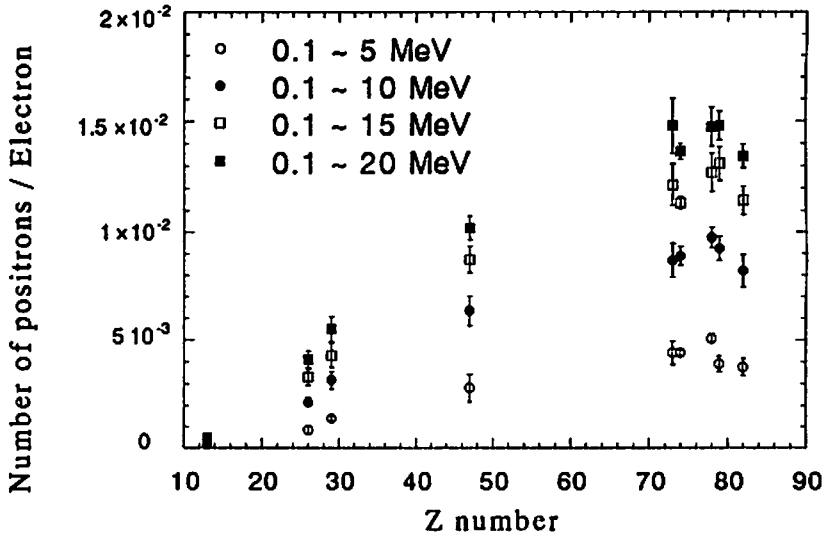

Fig. 7 Dependance of the positron yield on atomic number; the thickness of target is 1.5 radiation length, incident energy of electron is 45 MeV.

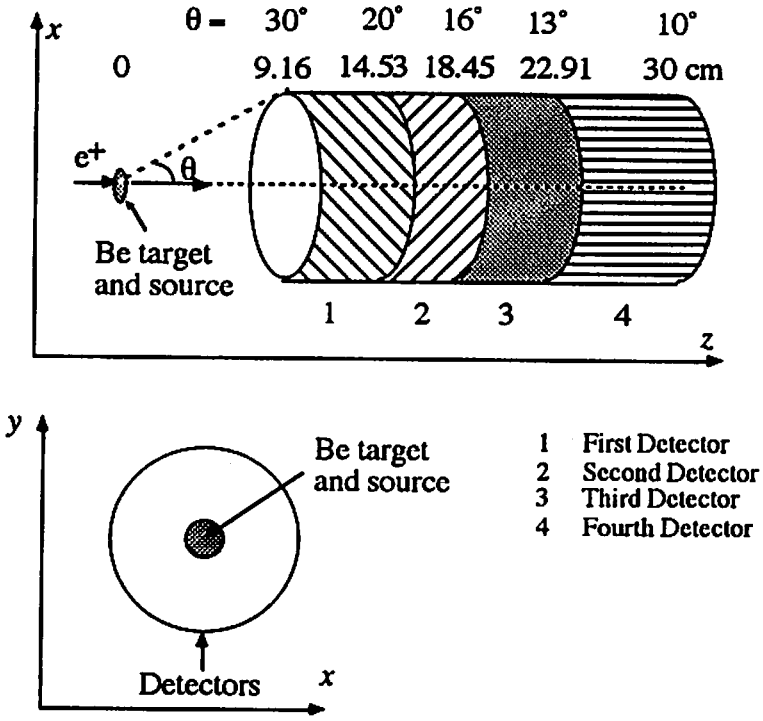

Figure. 8 Geometry of the Monte Carlo calculation of the photon produced by fast positron annihilation

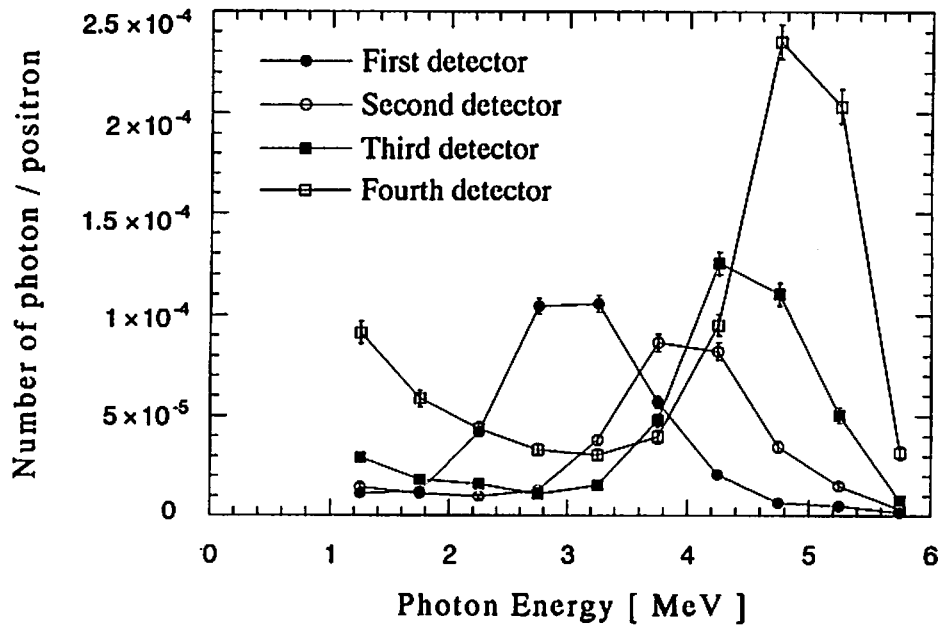

Fig. 9 Dependance of annihilation gamma yield on its angle; the thickness of Be target is 0.5 mm, incident energy of positron is 5 MeV.

RESPONSE OF A GM COUNTER TO HIGH-ENERGY PHOTONS CALCULATED BY THE EGS4/PRESTA CODE

K. KUDO, N. TAKEDA, K. SAKIHARA AND A. FUKUDA

Electrotechnical Laboratory
1-1-4, Umezono, Tsukuba, Ibaraki 305, Japan

H. Takahashi

CRC Research Institute, Inc.
1-3-D17, Nakase, Mihama-ku, Chiba-shi, Chiba 261-01, Japan

Abstract

A new type of ^{3}He-filtered GM counter to measure the dose of γ-rays existing in a thermal neutron field was investigated for its response to high-energy photons by using the EGS4/PRESTA Monte Carlo code by assuming a cylindrical model for the detector assembly. The energy distributions deposited in the GM gas region were calculated in the γ-ray energy range from 60 keV to 10 MeV. In order to determine the response curve of the GM counter up to 10 MeV, the effective threshold of the deposited energy, which means that the energy deposition over this threshold contributes to an output count, was determined as 27.1 eV by the least squares fit of the calculated response to the experimental one calibrated at the lower γ-ray energies of 60 keV, 662 keV and 1.25 MeV.

As a result, the γ-ray fluence and the effective dose equivalent have been determined by the experiments in the thermal neutron field together with the EGS4 calculations.

1. Introduction

It is often required in neutron calibration fields to determine the dose of γ-rays produced in a neutron source and in the surroundings, because some kinds of neutron detectors are sensitive both to neutrons and to γ-rays. In order to determine the γ-ray dose in the mixed field, many works have been done by using the energy compensated GM counters especially in fast neutron fields, because of its inherent low sensitivity for fast neutrons with some response to thermal neutrons [1-3]. The response of a GM counter to thermal

neutrons can be reduced with an additional shield of 6Li in thermal neutron fields. But, the handling of ^{6}Li metal or ^{6}LiF is not so easy and furthermore the optimum thickness for the thermal neutron absorption must be determined without perturbing the γ-ray intensity in the field.

For the precise measurement of γ-ray dose in the standard field of thermal neutrons, we have developed a new type of ^{3}He-filtered GM counter which consists of a commercially available GM counter surrounded by a ^{3}He gas filter to suppress the contribution of secondary γ-rays produced by thermal neutron captures in the GM counter itself.

The problem to be solved in the next step is the calibration method to high-energy photons. In our standard fields of exposure dose at ETL, the GM counter can be calibrated at conventional γ-ray energies using radioisotope sources of ^{241}Am, ^{137}Cs and ^{60}Co etc., but, over this energy range, high-energy photon fields have not been established.

The recent released electron photon shower code EGS4 [4] has been proved reliably to calculate the response functions of NaI, Ge and NE213 detectors for photon energies up to 15 MeV [5-7], and hence, in this report, the energy distribution deposited in the GM gas region was calculated by the EGS4/PRESTA code and the response of the GM counter was determined by integrating the deposited energy distribution above the effective threshold energy, which was determined by the least squares fit of the calculated response to the experimental one calibrated at the lower γ-ray energies of 60 keV, 662 keV and 1.25 MeV.

2. Measurements of γ-rays in a Thermal Neutron Field

The Electrotechnical Laboratory has established the standard field of thermal neutrons [8] in the outside of a graphite pile (2.3 m x 1.9 m x 1.9 m) for the calibration of personal dosimeters on a phantom, as illustrated in Fig.1. A ^{252}Cf neutron source(200 MBq) was positioned at the center of the pile and used to produce thermal neutrons. For the precise measurement of γ-ray dose in the standard field of thermal neutrons, we have developed a new type of ^{3}He-filtered GM counter which consists of a commercially available GM counter (type D3372-2 supplied by Hamamatsu Photonics K.K., Japan) surrounded by a cylindrical aluminum vessel (220.5 mm diameter and 163 mm height) filled with ^{3}He gas in the changeable pressure up to 6 atmospheres. The contribution of secondary γ-rays produced by thermal neutron captures in the GM counter itself can be excluded by increasing the gas pressure of ^{3}He. The count rate of the GM counter in the thermal neutron field is shown in Fig.2 as a function of the ^{3}He gas pressure. The dots indicate the experimental points and the solid line shows the calculated curve fitted to the experimental data. The count rate decreased with the increase of gas pressure and approached to the saturated value of 0.154 cps above the pressure of 4 atms. compared with the initial value of 0.297 cps at 0 atm. The net count rate for the γ-rays in the thermal neutron field after

subtracting the natural BG count rate from the gross count rate was obtained as 0.132 cps.

3. Monte Carlo Simulations with the EGS4 Code

The EGS4 (Electron Gamma Shower Version 4) is a general code for the Monte Carlo simulation of the coupled transport of photons, electrons and positrons in three dimensional geometry for energies above 10 keV for electrons and positrons and 1 keV for photons up to several TeV. The PRESTA (Parameter Reduced Electron-Step Transport Algorithm) routine was developed to minimize the dependence of the results on the step lengths in the electron transport simulation [9]. We therefore adopted the EGS4 code with the PRESTA routine to calculate the distribution of energy deposition in the gas region of the GM counter.

The geometry routines were written according to the models shown in Fig.3 by assuming a cylindrical model for the detector assembly. This assumption was valid for all parts, except for the outer wedge-shaped filter made of tin and lead alloy, which was approximated to be a combination of three different cylinders having increasing wall thicknesses of 0.2 mm, 0.8 mm and 1.4 mm step by step.

The source of incident photons was assumed to be a rectangular source having the same cross section as the plane containing the central axis of the GM counter, and was positioned at the outside of the detector assembly with an parallel angular distribution incident on the detector axis plane vertically in the energy range from 60 keV to 10 MeV.

The deposited energy distribution was calculated in the mixture gas region of helium (100 torr) and bromine (0.3 torr) of the GM counter as shown in Fig.4. It was found that the main deposited energy was distributed in the energy range below 100 eV.

4. Determination of the Response of a GM Counter

The response of the GM counter can be calculated by integrating the energy distribution in the deposited energy range from the lower limit to the upper limit. The lower limit of the deposited energy, that is, the effective threshold energy to produce an output count from the GM counter, must be obtained by other independent methods. In this paper, the threshold energy was assumed to be constant for any incident γ-rays having different energies, because all pulses produced from a GM tube are of the same amplitude regardless of the number of original ion pairs produced by primary electrons [10]. In order to determine the effective threshold energy for the detection, the GM counter was calibrated in the standard fields using RI sources at energies of 60 keV (^{241}Am), 662 keV (^{137}Cs) and 1.17 MeV +1.33 MeV (^{60}Co) and the response curve was obtained experimentally in the lower energy range. For the determination of the effective threshold, the calculated

response curve was fitted to the experimental one by changing the lower integration limit for the deposited energy distribution at three energy points and the effective threshold was obtained as 27.1 eV by the least squares fit. The response above the ^{60}Co energy was calculated by integrating the deposited energy distribution above 27.1 eV at each γ-ray energy. The response curve obtained by the EGS4 calculation with the calibration are shown in Fig.5. The experimental results are also shown as dotted data.

5. Results and Conclusion

The γ-ray energy distribution in the thermal neutron field shown in Fig.1, was calculated by the MCNP Monte Carlo code [11] by assuming three dimensional experimental assembly including the concrete floor in the experimental room. The distribution contained the high energy γ-rays above 3 MeV up to 10 MeV, as shown in Fig.6. As the informations on the energy spectrum of γ-rays and the response of the GM counter were known, the net response of the GM counter to the γ-rays in the thermal neutron field was calculated as 314 counts per fluence.

As a result, the effective dose equivalent of γ-rays contaminated in the thermal neutron field has been determined as $(1.7 \pm 0.3)\mu$Sv/h by using the conversion factor from fluence to effective dose equivalent.

The more precise calculation would be needed for the simulation of the outer wedge-shaped energy filter of the GM counter assembly for the EGS4 calculations and the calibration field of high energy photons would be also needed for the calibration purpose described in this paper.

References

[1] E .B .Wagner and G .S. Hurst, *Health Phys.*, 5 20(1961).

[2] J .H.Thorngate and D .R. Johnson, *Health Phys.*, **11**, 136(1965).

[3] S. Guldbakke, R. Jahr, H. Lesiecki and H. Schoelermann, *Health Phys.*, **39**, 963(1980).

[4] W. R. Nelson, H. Hirayama and D. W. O. Roger, *SLAC-Report-265* (1985).

[5] B. A. Faddegon, L. Van der Zwan, D. W. O. Rogers and C. K. Ross, *Nucl. Instr. and Meth.*, **A301**, 138(1991).

[6] D. W. O. Rogers, *Nucl. Instr. and Meth.*, **199**, 531(1982).

[7] L. Bueermann, S .Ding, S. Guldbakke, H. Klein, T. Novotny and M. Tichy, *Nucl. Instr. and Meth.*, **A332**, 483(1993).

[8] T. Michikawa, *Researches of the Electrotechnical Laboratory*, **No.746**(1974).

[9] A. F. Bielajew and D. W. O. Rogers, *Nucl. Instr. and Meth.*, **B18**, 165(1987).

[10] G. F. Knoll, "Radiation Detector and Measurement" Second edition, John Wiley & Sons, Inc.(1989).

[11] J. F. Briesmeister, Ed., *Los Alamos National Laboratory report La-12625* (1993).

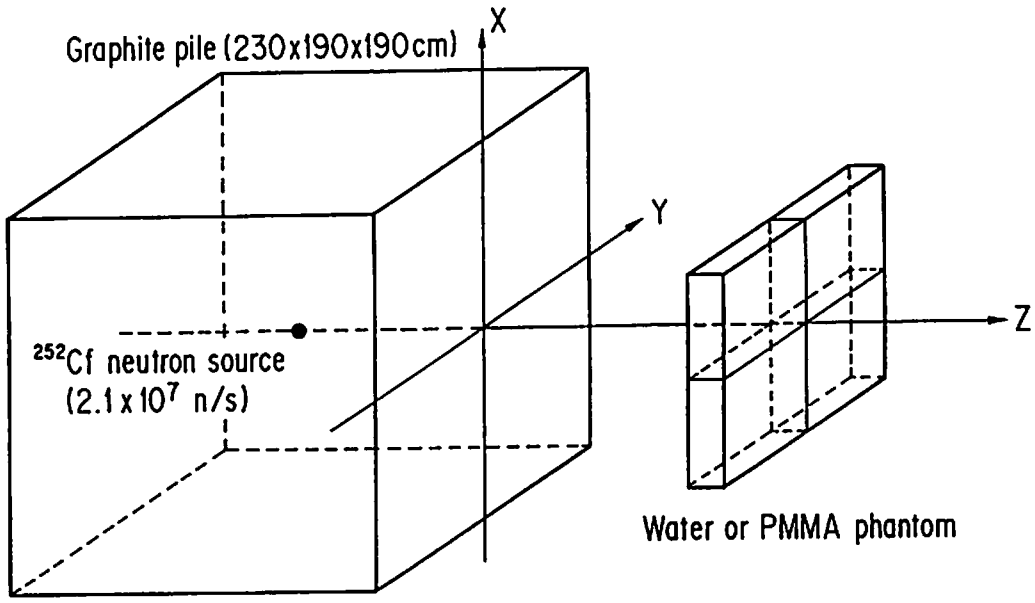

Fig.1 The standard field of thermal neutrons at the Electotechnical Laboratory

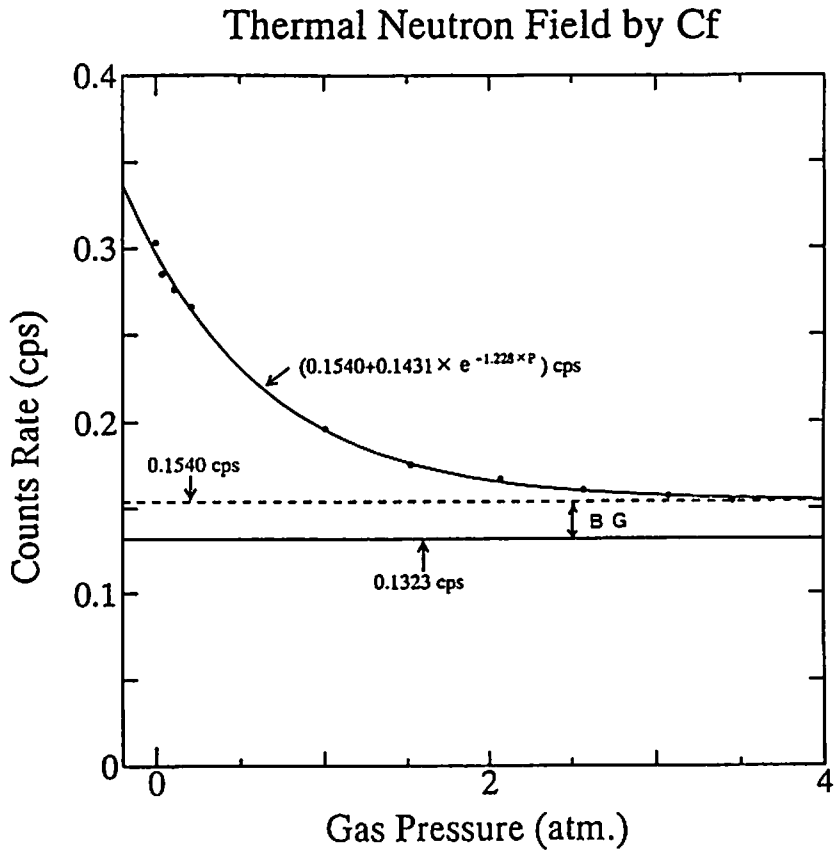

Fig.2 The count rate of the GM counter in the thermal neutron field as a function of the ^{3}He gas pressure. The dots indicate the experimental points and the solid line shows the least square curve fitted to the experimental data.

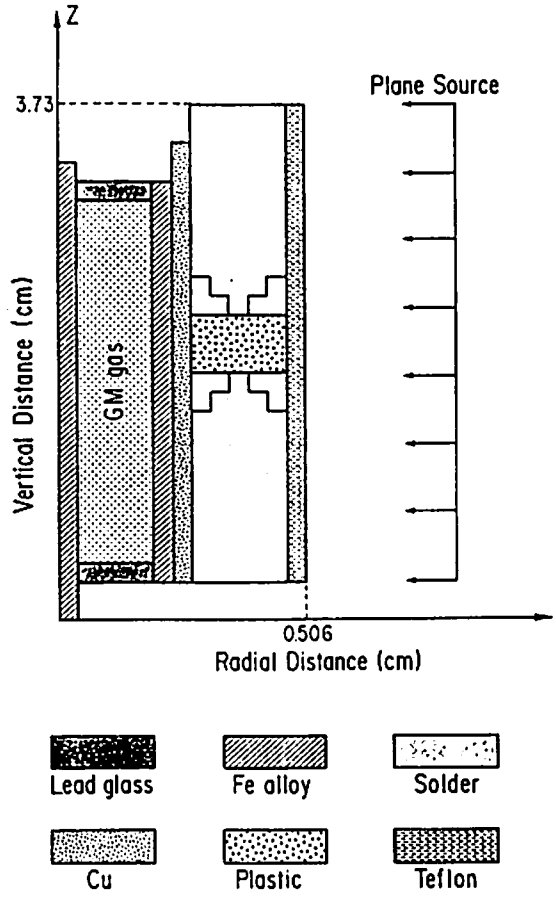

Fig.3 Calculation model of a GM counter

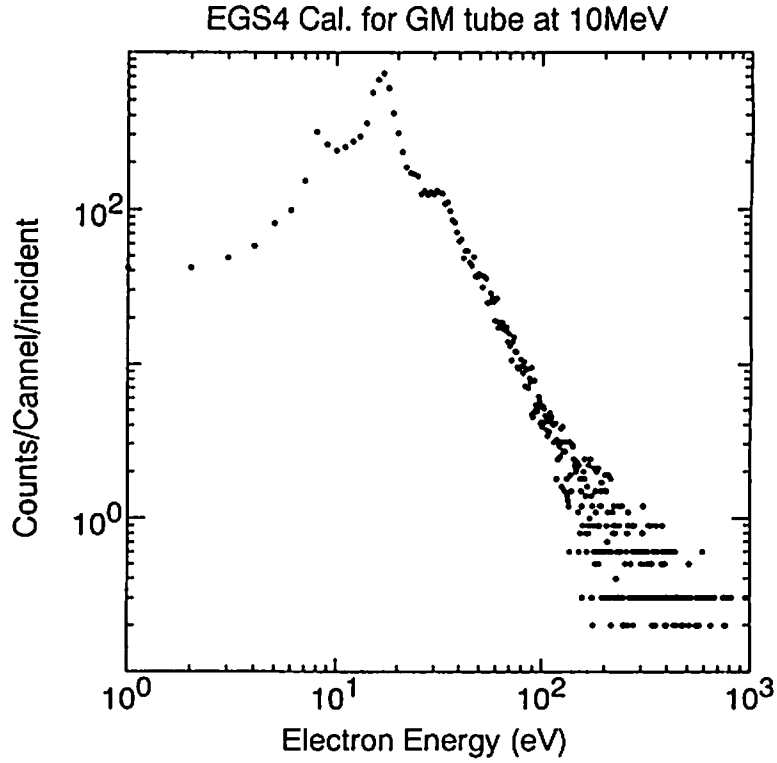

Fig.4 The distribution of deposited energy in the gas region of theGM counter calculated by the EGS4/PRESTA code

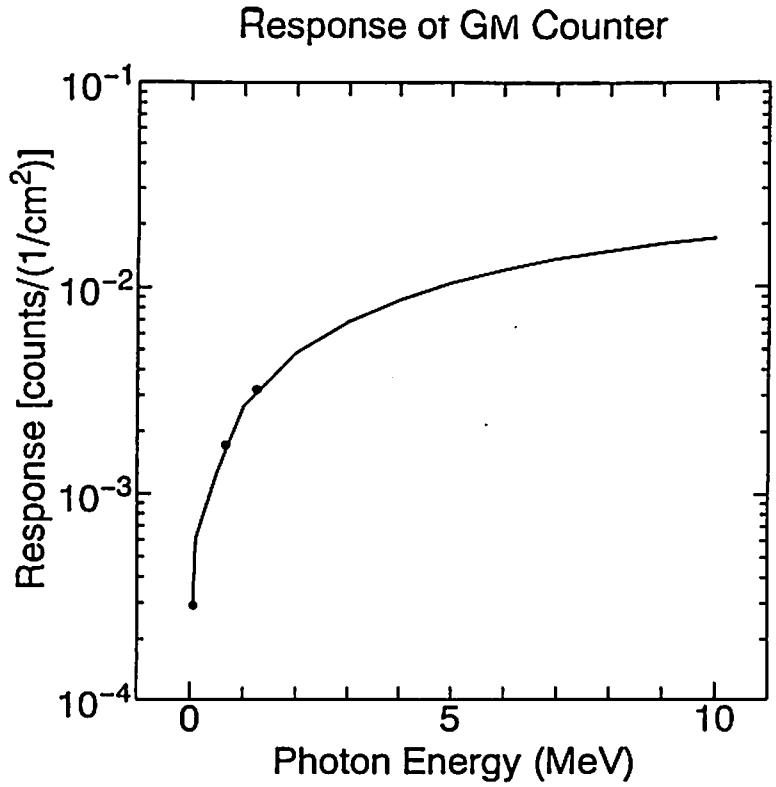

Fig.5 The response of the GM counter determined by the calculation (solid line) and the experiment (dots).

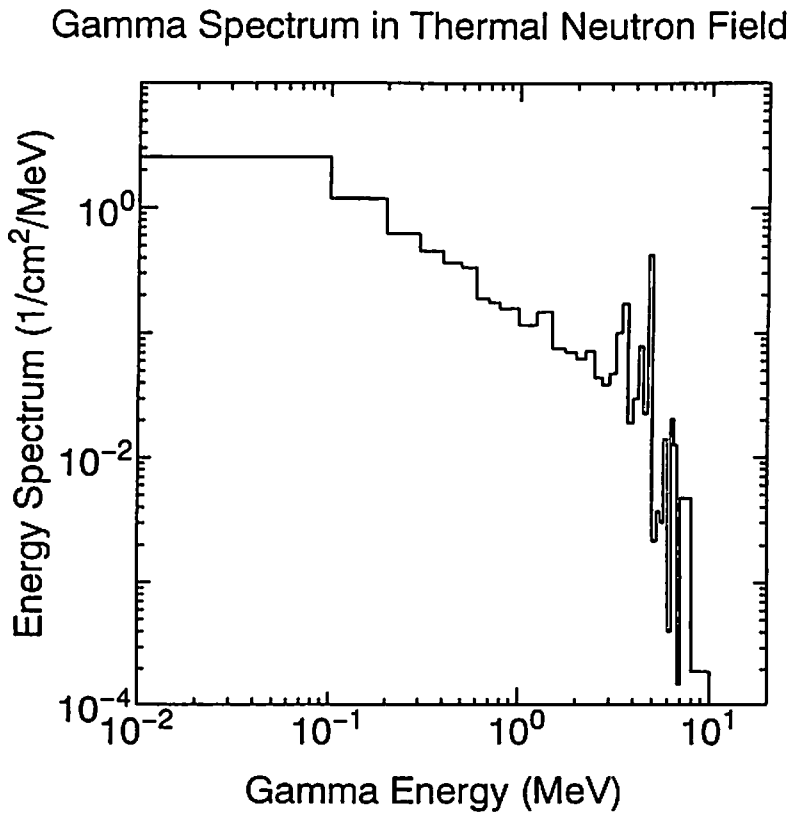

Fig.6 The γ-ray energy distribution in the thermal neutron filed calculated the MCNP Monte Carlo code.

A STUDY ON CALIBRATION METHOD FOR LIQUID EFFLUENT MONITOR

T. Torii, T. Sugita*, T. Hosono, K. Nomoto

Monju Construction Office,
Power Reactor and Nuclear Fuel Development Corporation
2-1 Shiraki, Tsuruga-shi, Fukui-ken 919-12, JAPAN

**Science System Laboratory*
1342-6 Sumiyoshi, Tomobe-machi, Ibaraki-ken 309-17, JAPAN

Abstract

The response of an effluent monitor for liquid radioactive waste has been calculated using the EGS4/PRESTA code. The calculated results agreed well with experimental ones using liquid standard sources and point sources. From the result for point sources, it suggests that the calibration method using only point sources can be applicable for other monitors of the same type.

1. Introduction

For the monitoring of the concentration of liquid radioactive waste, various radiation monitors are installed in nuclear facilities such as nuclear power plants. To evaluate the concentration, it is necessary to calibrate these monitors accurately. Effluent monitors for liquid radioactive waste generally employ sampling tanks with large capacity to enhance detection efficiency, so it is hard to calibrate them periodically with liquid radioactive sources. Even if it has been carried out, the process generates a large amount of unnecessary radioactive waste. Furthermore, because some nuclides that can be observed in nuclear facilities are not supplied as standard sources due to their short half-lives, it is impossible to perform the calibration for all of the observable nuclides.

For these reasons, we calculated the response of an effluent monitor to liquid radioactive sources by using the Monte Carlo calculation code EGS4/PRESTA[1,2], and compared them with the results from experiments using liquid radioactive standard sources. We also simulated the response of the monitor to a checking source modeled as a point source, in order to investigate the feasibility of a calibration method without using a liquid source.

2. Calculation Method

The subject of this simulation is an effluent monitor installed on the site of the prototype fast breeder reactor Monju, PNC. The monitor is employed as an NaI(Tl) scintillation detector (7/4"ϕ×2"L) located in the inner well of the sampling tank, as shown in Fig. 1. The effluent water is pumped continuously to the sampling tank with a volume of about 260 l, and the radioactivity in the water is measured by the detector.

A geometrical model of the effluent monitor composed the detector, the sampling tank and its shielding was created for the Monte Carlo calculation. Considering the shapes of the sampling tank, the well for the detector and the hole for checking source, the model of the monitor was constructed by the combinatorial geometry (CG) method using PRESTA-CG[3] code. For the liquid source simulation, gamma rays emitted randomly from nuclides in the sampling tank and the energies deposited in the scintillator are calculated. The responses of the monitor to four of the nuclides (^{40}K, ^{51}Cr, ^{60}Co, and ^{137}Cs) considered in the simulation have been measured experimentally. Other simulated nuclide sources included fission products (^{131}I, ^{134}Cs), corrosion products (^{54}Mn, ^{58}Co, ^{59}Fe), and ^{22}Na created in a fast breeder reactor. Since the discrimination level of the detector is set at the energy of 50 keV, only the number of particles which deposited energy greater than 50 keV in the scintillator are summed up. The history number is set from a hundred thousand to a million, taking account of statistical error. For the point source simulation, gamma rays are emitted to the $4pai$ direction from the hole for the checking source outside of the shielding (see Fig. 1).

The experiment with the standard liquid sources has used fresh water for dilution. However, the effluent water in the sampling tank is usually seawater. Therefore, for the four nuclides which have been measured experimentally, simulation has been done using both fresh water and seawater (density: 1.027 g/cm^3). For the other nuclides, only the case with seawater is calculated.

3. Results and discussion

Fig. 2 shows the results of the simulation with seawater and the experiment by liquid standard sources. The results of the simulation with fresh water are not plotted because the difference between the fresh water and seawater results is smaller than the statistical error (<10 %). As illustrated in Fig. 2, the results of simulation are in good agreement with those of the experiment, within 9 % for all nuclides experimented.

For the simulation using a point source, the sensitivity of the monitor is evaluated to be 1.303 cps/μCi for ^{137}Cs. It shows good agreement with the experimental data using ^{137}Cs (5, 80 μCi) with differences within 3 %.

From above results, the calculations simulated the experiment with sufficient accuracy.

It can be used to estimate the concentration of liquid radioactive waste even if the response is hard to obtain by experiment. Also, because of the good agreement for the point sources, it suggested that the calibration method using only point sources is applicable for other monitors of the same type.

References

[1] W. R. Nelson, H. Hirayama and D. W. O. Rogers, *The EGS4 Code System*, SLAC Report-265 (1985).

[2] A. F. Bielajew and D. W. O. Rogers, *Nucl. Instrum. Meth.* **B18** 165(1987).

[3] T. Sugita, T. Torii and H. Ando, KEK Proceedings 94-8, pp9-20 (1994).

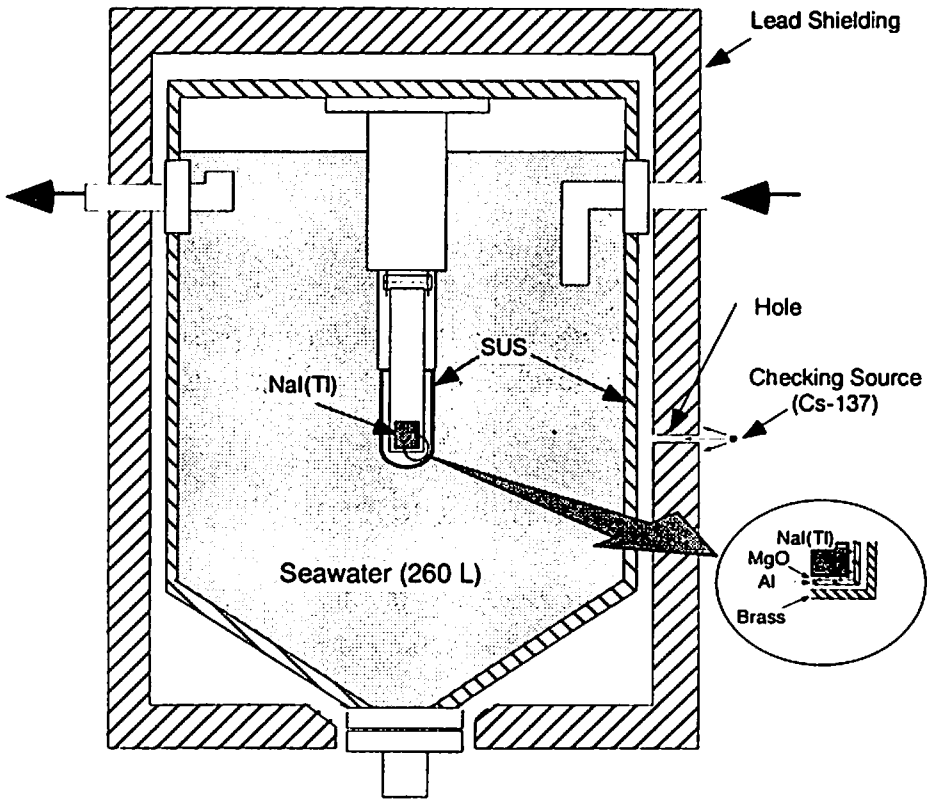

Fig. 1 Sectional View of Effluent Monitor

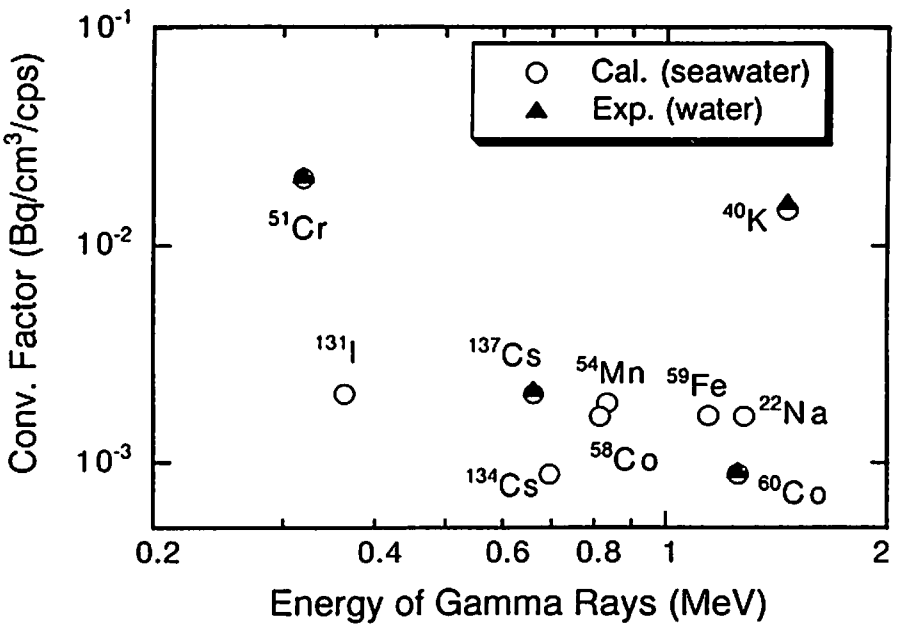

Fig. 2 Response of Effluent Monitor for Liquid Sources

PERFORMANCE SIMULATION OF LIQUID XENON IONIZATION DRIFT CHAMBER FOR DETECTING DOUBLE BETA DECAY OF ^{136}Xe

H. TAWARA, M. MIYAJIMA AND S. SASAKI

National Laboratory for High Energy Physics,
1-1 Oho, Tsukuba-shi, Ibaraki-ken, 305, Japan
and

A. G. PROKOPETS

The Graduate University for Advanced Studies,
1-1 Oho, Tsukuba-shi, Ibaraki-ken, 305, Japan

Abstract

An EGS4/PRESTA [1, 2] user code, UCLXE.MOR, is developing now to simulate the performance of a liquid xenon ionization drift chamber (LXeIDC) for detecting neutrinoless double beta ($0\nu\beta\beta$) decay of ^{136}Xe. The initial results on Monte Carlo calculation have been reported here. The "detector efficiency" of $0\nu\beta\beta$ decay events was computed 85 % for a prototype detector with 1 litter active volume. The trajectories of β-rays on $0\nu\beta\beta$ decay event, and also of 2.6 MeV gamma-ray from ^{208}Tl which is expected a dominant background source in an ^{136}Xe $0\nu\beta\beta$ decay experiment, have been calculated to develop various discrimination algorithm for improving background reduction capability of the detector.

1. Introduction

A nuclear double beta ($\beta\beta$) decay[3] experiment has been an extremely attractive attempt because it may probe grand unification scales far beyond present and future accelerator energies[4]. The neutrinoless double beta ($0\nu\beta\beta$) decay is one of the $\beta\beta$ decay modes predicted theoretically. It is a lepton non-conserving process and is forbidden in the Standard Model. This decay mode can take place only when the electron neutrino is a massive Majorana particle[5, 6, 7]. The neutrino mass plays a key role in modern theoretical particle physics and is one of the candidates for non-baryonic dark matter in the universe. The observation of $0\nu\beta\beta$ decay also gives us information on the structure of the weak interaction such as leptonic currents with a small right-handed component.

The Q value, i.e., the kinetic energy available to the leptons, is shared by two electrons in the case of $0\nu\beta\beta$ $[0^+ \rightarrow 0^+]$ transition of the two-nucleon mechanism, and consequently,

the sum-energy spectra of the two electrons exhibit a monochromatic peak at the Q value as illustrated in fig.1. The $0\nu\beta\beta$ decay may take place via other possible non-nucleonic mechanisms such as a process with the emission of a Majoron (X)[8, 9]. As shown in fig.1, the 0ν,$X\beta\beta$ mode displays a typical three-body decay spectrum peaked at approximately 80 % of the Q value. On the other hand, the $2\nu\beta\beta$ mode shows a four-body decay spectrum peaked at around 40 % of the Q value. The energies carried by the residual nucleus in the $\beta\beta$ decay modes are negligible.

We have developed a self-triggered liquid xenon ionization drift chamber with a multi-segmented collector electrode for the ^{136}Xe $0\nu\beta\beta$ decay experiment[10, 11]. Liquid xenon is one of the prominent materials for the $\beta\beta$ decay experiment. Nuclear energy level schemes for ^{134}Xe and ^{136}Xe are shown in fig.2. The Q value of ^{136}Xe, 2.479 MeV, is large compared to other candidate isotopes, and so a shorter half-life can be expected since a decay rate is proportional to the phase space which is proportional to some powers of the Q value. Furthermore, the background rate such as gamma-rays due to natural radioactive isotopes drops exponentially toward higher energy region. Liquid xenon is advantageous not only as a source of $\beta\beta$ decay (^{134}Xe,^{136}Xe) but also as a medium for a radiation detector as described in the section II.

However, the observation of $\beta\beta$ decays is extremely complicated because of their long half-lives. Recently, Gotthard group has reported the following 90 % C.L. half-life limits for $[0^+ \rightarrow 0^+]$ transition: 0.37×10^{24} years in the "mass mechanism" mode, and 0.28×10^{24} years in the "right-handed weak currents" mode[12]. Their enriched gaseous xenon TPC has around 30 % "detector efficiency", i.e., the probability that the kinetic energies of two electrons from $\beta\beta$ decay are completely deposited in the active volume[13]. There has been, however, no obvious evidence of $0\nu\beta\beta$ decay up to the present in any existing experiment. The future progress in the search for $\beta\beta$ decay strongly depends on further improvement of the signal to background ratio. The use of liquid xenon allows increasing the detection efficiency as well as the number of candidate isotope. Furthermore, massive liquid xenon itself is an effective shielding material to background, especially alpha particles or "single" beta-rays emitted from radioactive isotopes included in internal components of a detector. The higher sensitivity in the $\beta\beta$ decay experiment, therefore, can be achievable even after applying the background rejection method such as "fiducial volume cut" and signal analysis.

It is troublesome to experimentally assess the detector performance such as the detection efficiency and the capability of background reduction in the $\beta\beta$ decay experiment. The Monte Carlo electron-photon transport code with a Parameter Reduced Electron-Step Transport Algorithm, EGS4/PRESTA[1, 2], is useful to simulate physical processes caused by beta-ray and gamma-ray in liquid xenon. We are developing now EGS4/PRESTA user

code, UCLXE.MOR, in order to obtain information on the performance of a liquid xenon ionization drift chamber (LXeIDC) for the $\beta\beta$ decay experiments.

We report here some preliminary results on the calculation using UCLXE.MOR for the ^{136}Xe $0\nu\beta\beta$ decay experiment with the prototype detector: the detector efficiency, expected spectra of the $\beta\beta$ decay event as well as background gamma-ray from ^{208}Tl which is the most probable background source under typical laboratory condition. In addition, the trajectories of $0\nu\beta\beta$ decay events and gamma-ray events have been discussed in order to develop the method for rejecting background signals by analysing charge signals from a multi-segmented collector electrode.

2. Liquid Xenon Ionization Drift Chamber

The prototype LXeIDC has been constructed in National Laboratory for High Energy Physics (KEK). The superior properties of a liquid xenon detector for beta-ray and gamma-ray spectroscopy, namely for the $\beta\beta$ experiment are the following. The small W-value (15.6 eV)[14], the low diffusion coefficient (65 cm^2s^{-1})[15] and the large drift velocity (3×10^5 cms^{-1} at >3 kV/cm)[16, 17] for free electrons are good for an ionization chamber. The high yield ($> 1.5 \times 10^5$ photons at 2.5 MeV)[18, 19] and the fast decay (fast component 3 ns)[20] of scintillation light provide an excellent scintillation detector with the fast triggering capability. The high density (3.06 gcm^{-3} at -109 °C), high atomic number (Z=54), the nearly constant drift velocity above the 5 kV/cm electric field and the flexibility of liquid lead to a large-size position sensitive detector with an excellent detection efficiency.

Figure 3 is the cross-sectional view of the main part of apparatus. The prototype is a single gridded ionization chamber and scintillation detector equipped with four photo-multipliers. The detector system has been reported in detail[10, 11].

The detector has a cylindrical active volume of 1 litter between the cathode and the grid plane. The length of drift region is 4 cm. This kind of long-distance drift of free electrons can be achievable only in very high purity of liquid xenon which is obtained by using the rare gas purification system[21]. The natural abundance of ^{136}Xe is 8.87 %, giving a total of 1.2×10^{24} ^{136}Xe atoms in the active volume. The use of liquid xenon enriched up to 100 % of ^{136}Xe provides the candidate atoms of 1.3×10^{25} which is equivalent to that of the enriched gaseous TPC in the Gotthard experiment[12, 13]. One of the unique properties of the detector is the multi-segmented collector electrode as shown in fig.4. It contains 37 hexagonal segments with a side length of 14.5 mm and 6 irregular shape ones. This multi-segmented structure of the collector electrode allows the LXeIDC to work as an association of 43 "small ionization chambers", and then the energy measurement for each event is performed on those chambers independently due to the detected charge. The acquisition of charge signals from segments is triggered by corresponding scintillation

light. The position of a segment with a charge signal provides the spatial information of the energy deposition on an X-Y plane. The time evolution of a charge signal also gives information along a Z-direction.

This collector structure is intended to use an anti-coincidence method to identify background signal as discussed in the following section.

3. Monte Carlo Calculation

3.1 Model of LXeIDC

Figure 5 illustrates the model of the LXeIDC simplified for the Monte Carlo calculation. It consists of two materials for an initial examination: vacuum and liquid xenon which density is 3.06 gcm^{-3}. A liquid xenon region is divided into two regions: an active volume (drift region) and the dead volume enveloping the active volume. This geometry can be described with the combination of two coaxial cylinders and five parallel planes which are coded by using geometry Macros in EGS4 code. In the EGS4/PRESTA calculation, UCLXE.MOR scores the energy deposition and the X-, Y-, Z-coordinates of every step in the history of particle transportation, and then determines the position of segment including that scored point.

3.2 Source

The following two kinds of sources were used in the calculation.

a. $0\nu\beta\beta$ *decay* : The source to be distributed uniformly in a liquid xenon region is assumed. At any source, two electrons are generated and go to the opposite direction each other. The Q value of decay, 2.479 MeV, is shared by these electrons, but the ratio of kinetic energies carried by them is selected at random.

b. Background : A pulse height spectrum of background measured by a $2''\phi \times 2''$ NaI(Tl) scintillator in a concrete building is shown in fig.6[22]. It is indicated that the dominant background superimposed on the peak of $0\nu\beta\beta$ decay is gamma-ray from ^{208}Tl. For the first demonstration, 2.6MeV gamma-ray isotropically incident to the surface of the liquid xenon region from outside is assumed as a background source. The uniformity of the flux of gamma-ray is assured over the liquid xenon region.

4. Results and Discussion

4.1 Energy Spectra and Detector Efficiency

The spectra of $0\nu\beta\beta$ decay and gamma-ray from the LXeIDC has beem calculated as shown in fig.7. It is assumed that the energy resolution is 3.5 % in FWHM at 2.5 MeV

and be inversely proportional to the square root of energy[23]. These spectra predict that the peak of $0\nu\beta\beta$ decay event is situated in the trough between the Compton edge and the full-energy peak of 2.6 MeV gamma-rays. The signal to background ratio strongly depends on the energy resolution. Further calculation of the energy resolution dependence is performing now with background rejection algorithm as discussed in the following sections.

In the spectrum of gamma-ray, single- and double-escape peaks are evident. The existence of liquid xenon in a dead volume contributes to create a peak at 511 keV from annihilation photons and a backscatter peak around 250 keV due to Compton scattering.

The 3σ detector effeciencies were obtained to be 85 % for a 1 litter active volume, and 53 % for a small chamber which is segmented one with about 5.4 cm^3 volume, respectively. Liquid xenon chamber displays extremely high detection efficiency comparable to the Ge detector (about 90 %) for the $\beta\beta$ decay experiment[24].

4.2 Anti-coincidence Method by Multi-segmented Collector

A simulation of the spatial distribution of energy deposition in liquid xenon due to beta-ray and gamma-ray is quite helpful not only for the estimation of the detection efficiency, but also for the demonstration of charge and scintillation signals in order to develop the various discrimination algorithm which rejects background signals in off-line analysis, as well as in on-line one.

A $\beta\beta$ decay event in liquid xenon is observed as a continuous energy deposition, that is, a "single-site charge-blob" of which size is about 2 mm typically. On the other hand, the interaction of gamma-ray in liquid xenon (Z=54) is dominated by Compton scattering in the energy region from 300 keV to 6 MeV (see fig.8 taken from The Atomic Nucleus by R. D. Evans[25]). Therefore, gamma-rays in the MeV energy region give mainly rise to Compton scattering which generates multiple scattered energy deposition, that is, "multi-site charge-blob", in liquid xenon. Figures 9a and 9b show the trajectories on an X-Y plane of beta-rays emitted from ^{136}Xe (a), and of 2.6 MeV gamma-rays (b) displayed by using the EGS4 shower display system (EGS4PICT)[26]. The inside of an inner circle corresponds to the active volume of 1 litter.

The red lines shown in fig.10 demonstrate energy depositions on $0\nu\beta\beta$ decay events (a, b) and gamma-ray events (c) along Z-direction in seven neighboring segmented drift regions, respectively. The single-site charge-blobs due to beta-rays mostly generates a charge signal from only one segment (fig.10a), or those from two neighboring segments which appear at the same time (fig.10b). The coincidence of signals from three neighboring segments is also possible but the fraction is quite small. The multi-site charge-blobs of gamma-rays can generate the plural charge signals from more than three segments, or those not from neighboring segments (fig10c). It is also possible that an anti-coincidence

in time happens among them. Accordingly, some of multiple Compton scattering events can be distinguished from the $\beta\beta$ decay events by means of the anti-coincidence method using the multi-segmented collector. The rejection efficiency of 2.6 MeV gamma-ray events from the 3σ interval of the $0\nu\beta\beta$ peak is roughly 30 % with the present structure of the multi-segmented collector. This efficiency depends on the size of segment. The smaller segment size might be desirable but leads to the increase of the number of electronic parts.

4.3 Pulse Shape Analysis

In addition to the anti-coincidence method mentioned above, pulse shapes of charge signals from segments offer information along the Z-direction to identify gamma-ray event, even when a gamma-ray deposits the whole energy into one or two neighboring segments.

The charge-blobs of a gamma-ray event which are superimposed on the $0\nu\beta\beta$ decay peak splash along Z-direction up to 4 cm long as shown in fig.11a. This length is equivalent to those of the drift region. On the other hand, the $\beta\beta$ decay events are put in a compact space (fig.11b). The shapes of integrated energy deposition (the blue lines in fig.10) reflect on the time evolution of charge signal (typically on the rise time). The rise time of pulses from segments correspondent with the $\beta\beta$ event have shorter than those due to gamma-ray in many cases. For the more precise analysis of the pulse shape, it is necessary to take into consideration of the drift time between grid-collector region, the distribution of charges along Z-direction, the effect of shielding inefficiency of grid electrode and the diffusion of electrons etc.

5. Conclusion

Monte Carlo calculation predicts that a LXeIDC with the multi-segmented collector electrode has an excellent detection ability of the $\beta\beta$ decay event. The EGS4/PRESTA code can give us the useful information for the anti-coincidence method and for the pulse shape analysis intended to reject backgrounds. The anti-coincidence capability of the LXeIDC associated with a properly designed multi-segmented collector can be expected to greatly improve the signal to background ratio.

The results on the Monte Carlo calculation such as the detection efficiency should be assessed more carefully because many simplifications, for example, a geometry model of a detector, could cause large ambiguity [27]. In addition to ^{208}Tl, the backgrounds from other natural radioactive isotopes, cosmic rays, activation of instrument materials have to be taken into account. The precise pulse shape analysis of charge signals associated with scintillation signals is also needed.

The simulation of the $2\nu\beta\beta$ decay experiment is being planed. The user code UCLXE.MOR is intended to be continuously improved with the advancement of the ex-

periment.

References

[1] W. R. Nelson, H. Hirayama, and D. W. O. Rogers, SLAC-265 (Stanford University, Stanford 1985).

[2] A. F. Bielajew, and D. W. O. Rogers, Nucl. Instrum. and Meth. **B18**, 165 (1987).

[3] F. Boehm and P. Vogel, "Physics of Massive Neutrinos", 2nd ed., Cambridge University Press, Cambridge, England (1992).

[4] H. V. Klapdor-Kleingrothaus and A. Staudt, "Non-Accelerator Particle Physics", A. Hilger, Bristol, New York (1994).

[5] J. Schechter and J. W. F. Valle, Phys. Rev. **D25**, 2951 (1982).

[6] J. F. Nieves, Phys. Lett. **147B**, 375 (1984).

[7] E. Takasugi, Phys. Lett. **149B**, 372 (1984).

[8] G. B Gelmini, S. Nussinov, and M. Roncadelli, Nucl. Phys. **B209**, 157 (1982).

[9] H. M. Georgi, S. L. Glashow, and S. Nussinov, Nucl. Phys. **B193**, 297 (1981).

[10] A. G. Prokopets et al., KEK Proceedings **94-7**, 60 (1994).

[11] A. G. Prokopets et al., KEK Proceedings **95-1**, 183 (1995).

[12] V. Jörgens et al., Nucl. Phys. **B35**, 378 (1994).

[13] J. -C. Vuilleumier et al., Phys. Rev. **D48**, 1009 (1993).

[14] T. Takahashi et al., Phys. Rev. **A12**, 1771 (1975).

[15] E. Shibamura et al., Phys. Rev. **A20**, 2547 (1979).

[16] L. S. Miller, S. Howe, and W. E. Spear, Phys. Rev. **116**, 871 (1968).

[17] E. Shibamura et al., Nucl. Instr. and Meth. **131**, 249 (1975).

[18] M. Miyajima et al., IEEE Trans. Nucl. Silence, **NS39**, 536 (1992).

[19] T. Doke, K. Masuda, and E. Shibamura, Nucl. Instr. and Meth. **A291**, 617 (1990).

[20] S. Kubota et al., Nucl. Instr. and Meth. **196**, 101 (1982); S. Kubota et al., Nucl. Instr. and Meth. **A242**, 291 (1986); S. Kubota, M. Hishida, and J. Raun (Gen), J. Phys. **C11**, 2645 (1978).

[21] M. Miyajima et al., Nucl. Instr. and Meth. **134**, 403 (1976).

[22] M. Miyajima, Hoshasen, **15-1**, 45 (1988), in Japanese.

[23] E. Aprile, R. Mukherjee and M. Suzuki, Nucl. Instr. and Meth. **A302**, 177 (1991).

[24] F. Petry et al., Nucl. Instr. and Meth. **A332**, 107 (1993).

[25] R. D. Evans, "The Atomic Nucleus", MacGrow-Hill (1955).

[26] H. Hirayama et al., KEK Internal **94-10** (1994).

[27] H. S. Miley et al., Nucl. Phys. **B35**, 388 (1994).

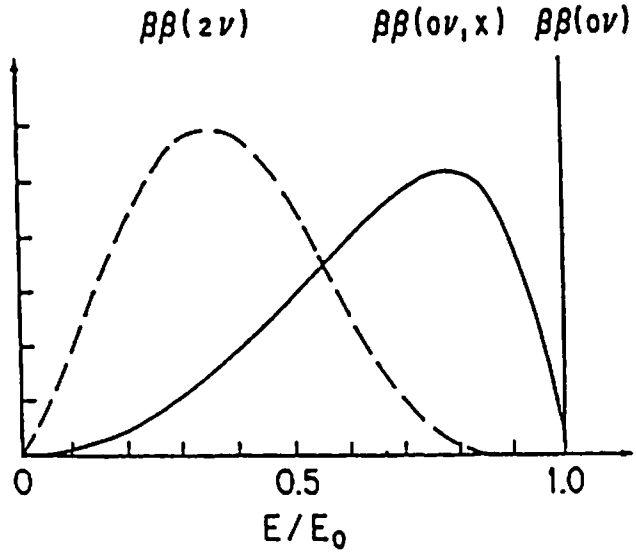

Fig. 1. Theoretically predicted sum-energy spectra of the two electrons emitted on the following decay modes: 2ν mode : $(A,Z) \rightarrow (A,Z+2) + 2e^- + 2\bar{\nu}$, 0ν mode : $(A,Z) \rightarrow (A,Z+2) + 2e^-$, and 0ν,X mode : $(A,Z) \rightarrow (A,Z+2) + 2e^- + X$.

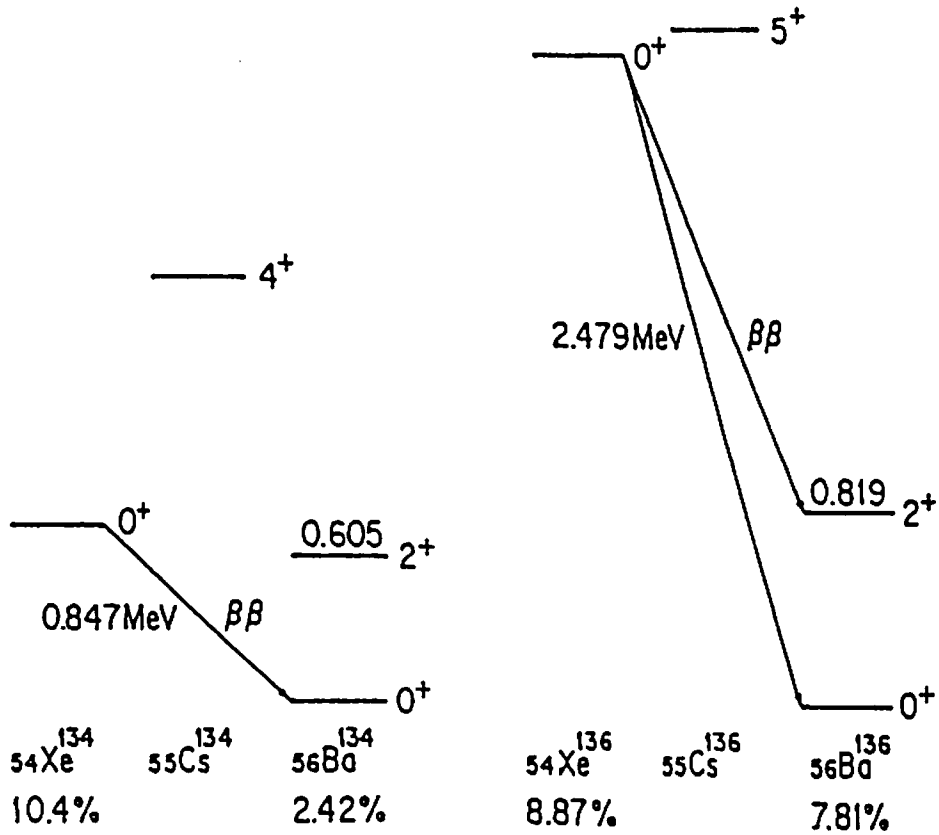

Fig. 2. Nuclear energy level schemes of ^{134}Xe, ^{136}Xe on $\beta\beta$ decay. Natural isotopic abundances are shown below isotopes concerning the decay.

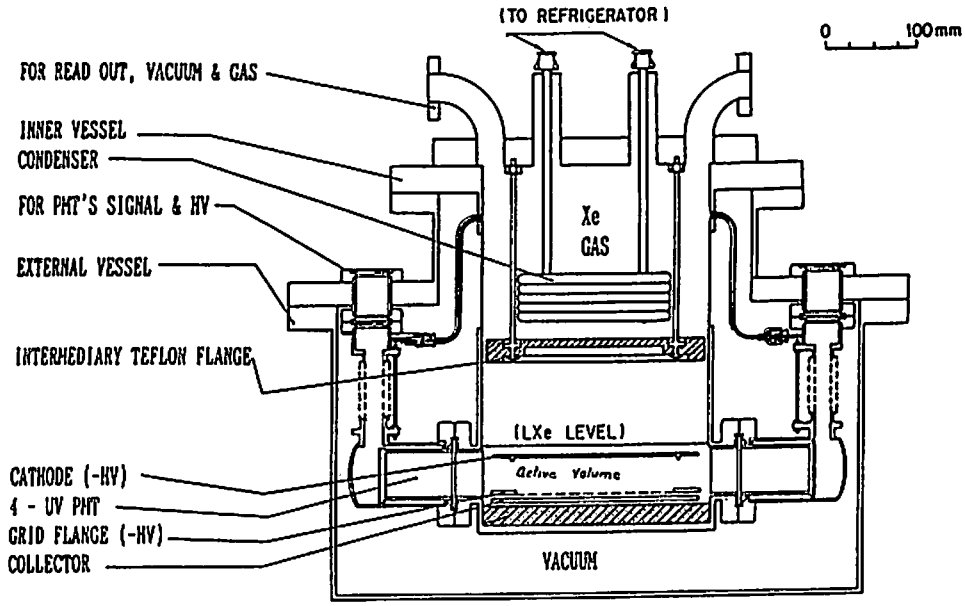

Fig. 3. Cross-sectional view of the self-triggered liquid xenon ionization drift chamber.

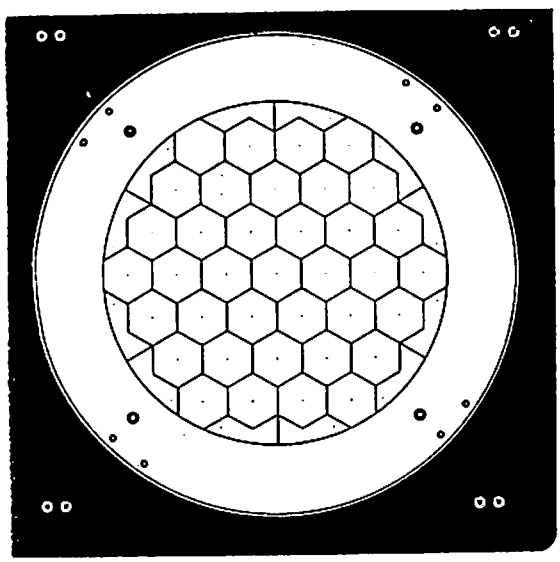

Fig. 4. Multi-segmented collector of the prototype detector.

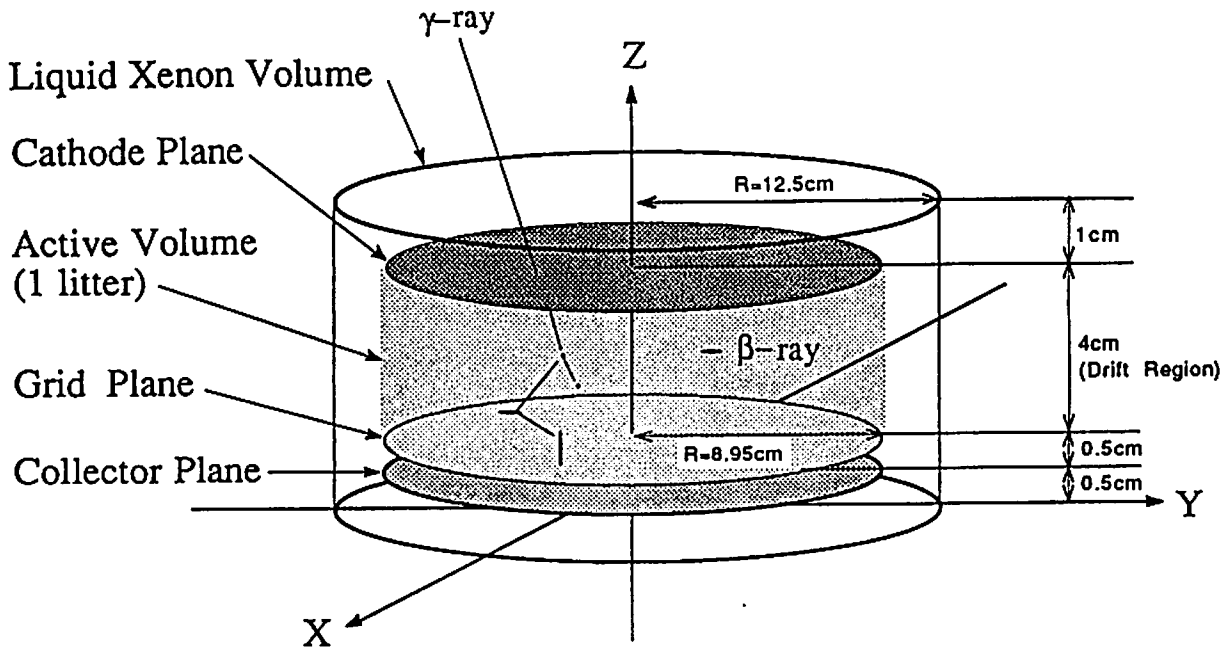

Fig. 5. Simplified model of LXeIDC for EGS4/PRESTA Monte Carlo calculation.

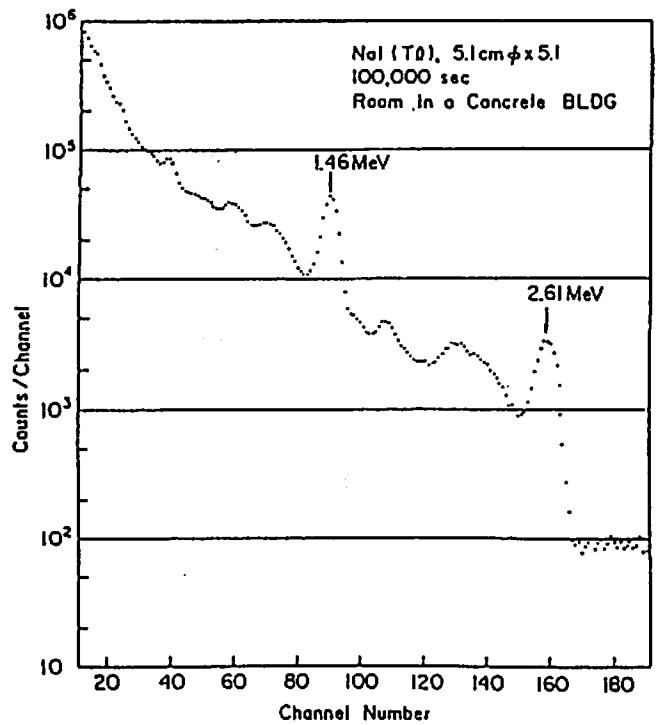

Fig. 6. Pulse height spectrum of backgrounds measured by a $2''\phi \times 2''$ NaI(Tl) scintillator in a concrete building.

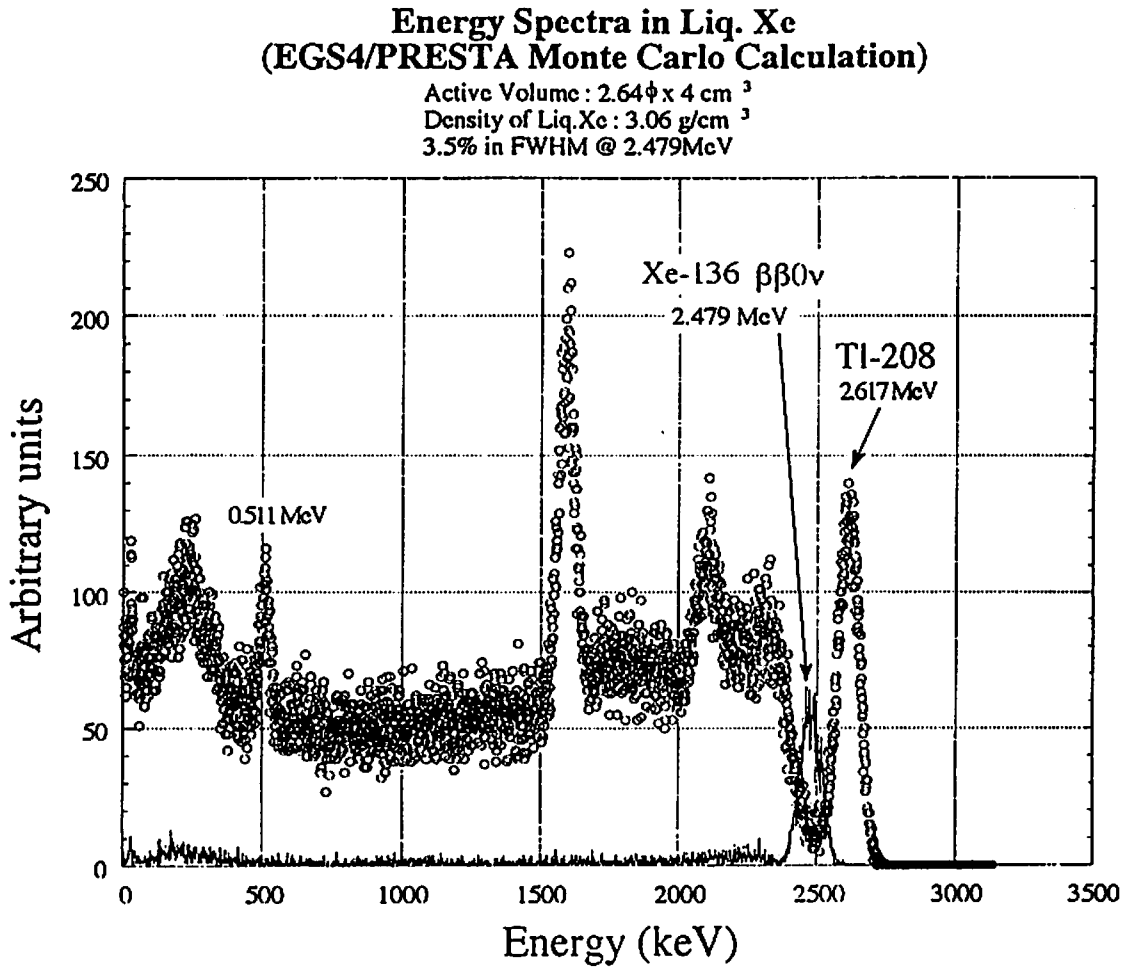

Fig. 7. Simulated spectra of ^{136}Xe $0\nu\beta\beta$ decay (solid line) and of 2.6 MeV gamma-ray (circles) from LXeIDC. The density of liquid xenon is assumed to be 3.06 gcm^{-3}.

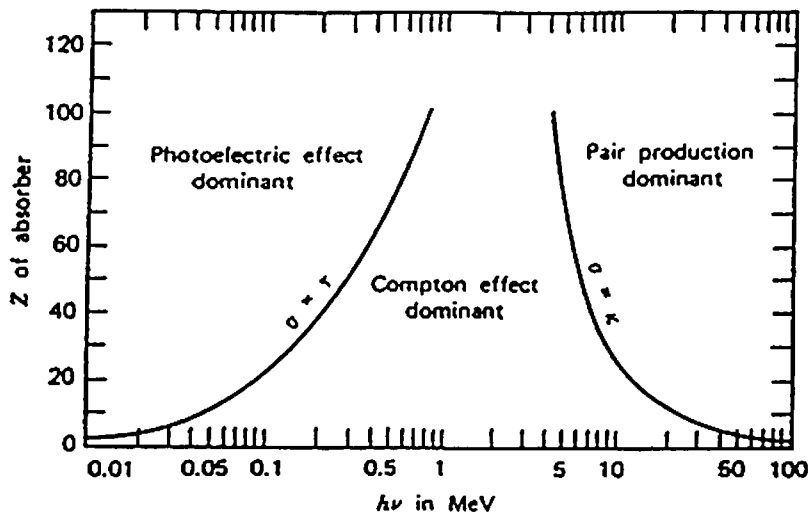

Fig. 8. Relative importance of the three principal types of gamma-ray interactions in matter, (From The Atomic Nucleus by R. D. Evans).

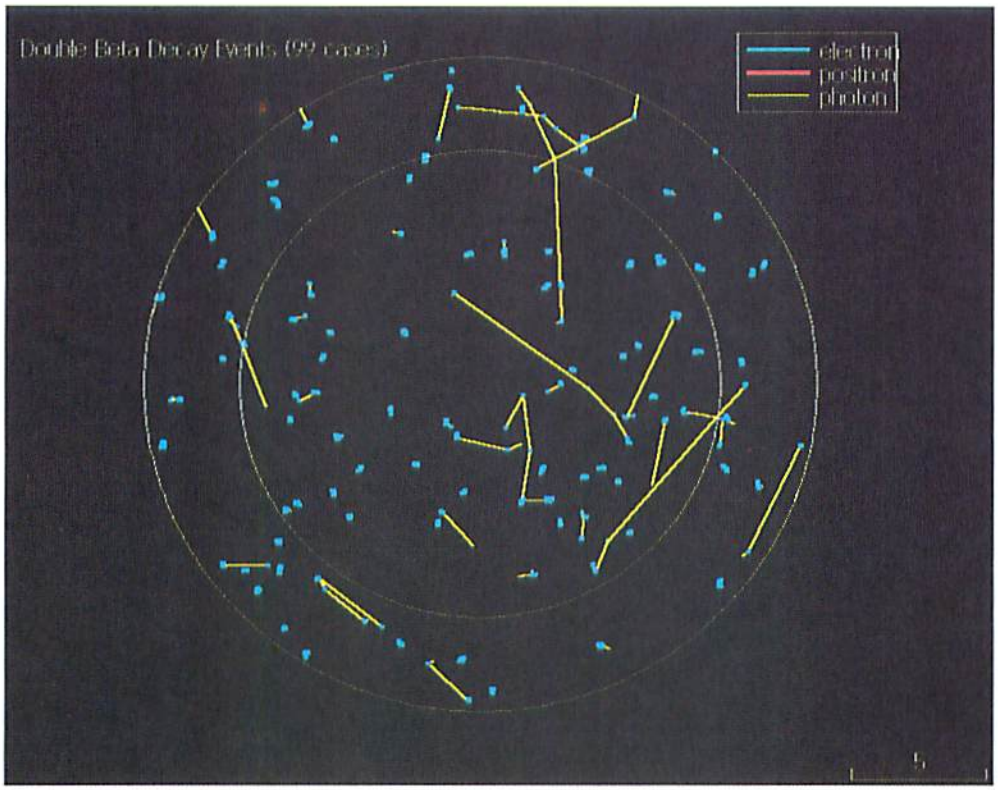

(a)

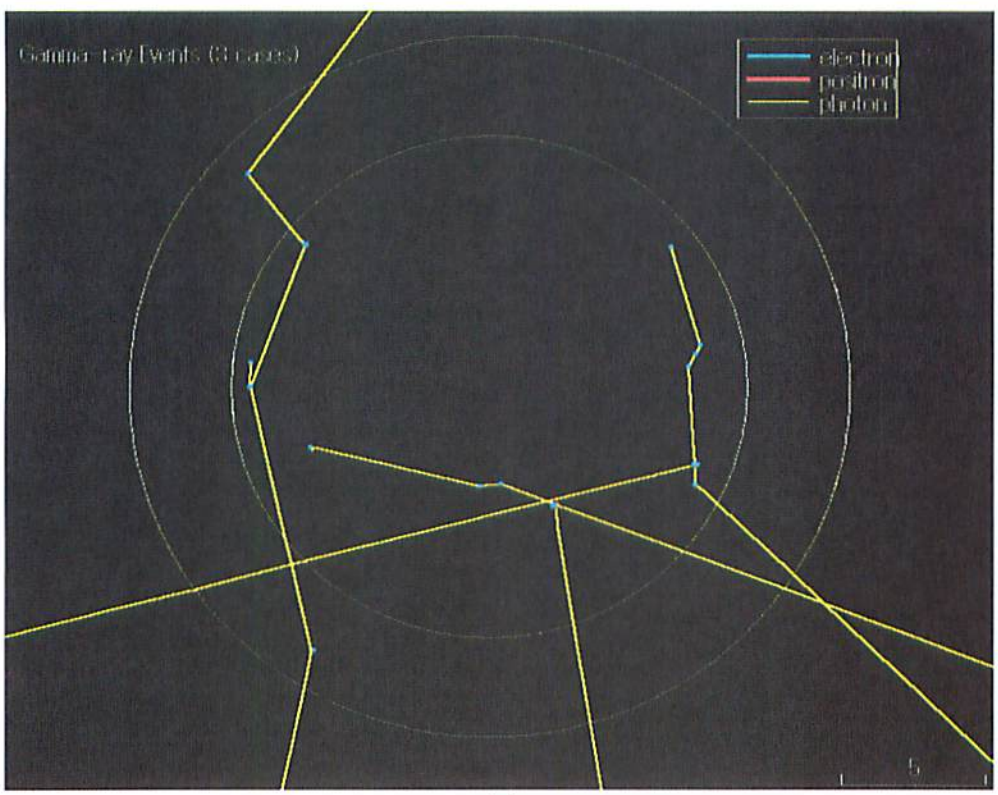

(b)

Fig. 9. Simulation of particle trajectories of electrons from $0\nu\beta\beta$ decay (a) and of 2.6 MeV gamma-rays (b). The X-Y projection are shown. The unit of scale on the right bottom is in cm.

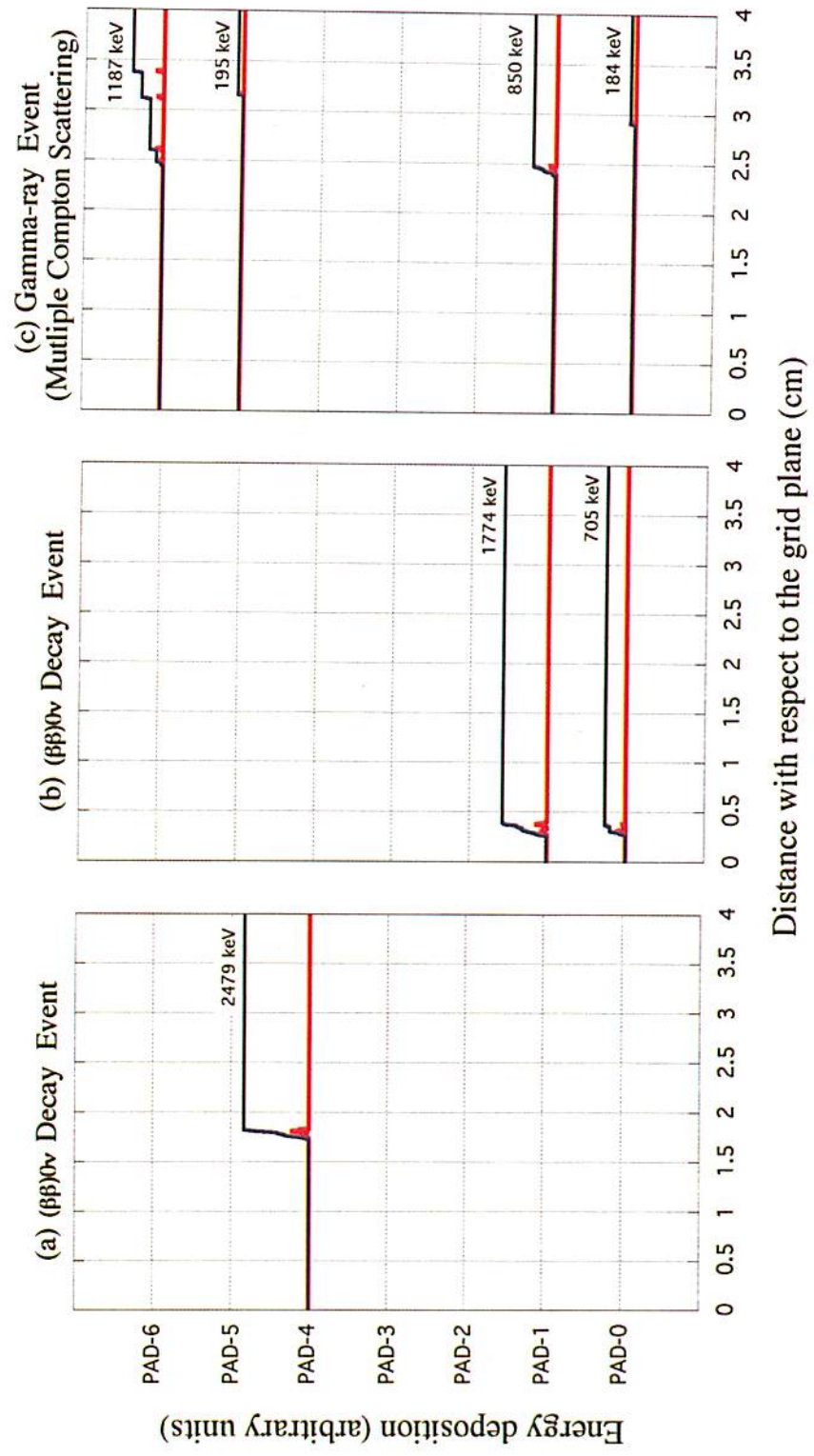

Fig. 10. Examples of calculated energy depositions in seven neighboring segmented drift regions (pad-0 to pad-6) due to $0\nu\beta\beta$ decay (a,b) and 2.6 MeV gamma-ray (c). Red and blue lines indicate the energy depositions and the integrated ones along Z-direction, respectively.

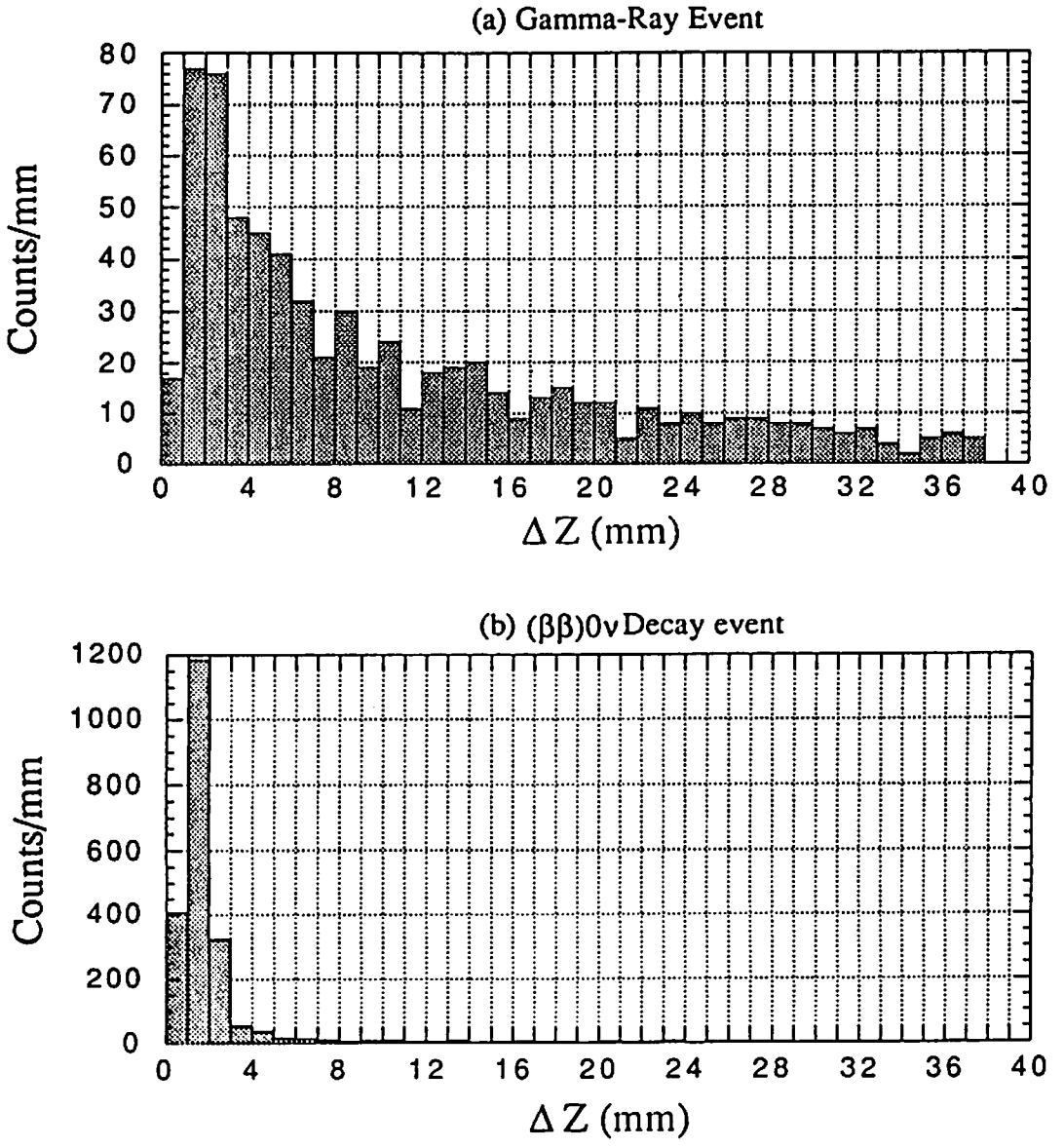

Fig. 11. Distribution of the interval along Z-direction, ΔZ, in which charge-blobs are generated due to gamma-ray event (a) or beta-ray event (b), and are contained only in one segmented drift region.

APPROXIMATING FORMULA FOR GAMMA-RAY MULTILAYER BUILDUP FACTORS

K. SHIN and H. HIRAYAMA†

Department of Nuclear Engineering, Kyoto University
Yoshida, Sakyo-ku, Kyoto 606, Japan
†National Laboratory for High Enery Physics
1-1, Oho, Tsukuba-shi, Ibaraki 305, Japan

1. Introduction

Gamma-ray buildup factors are key input for point kernel codes, which have been widely used as a practical tool for the gamma-ray shielding calculation. A set of standard gamma-ray point isotropic buildup factors and fitting parameters of the G-P function was already evaluated[1] for homogeneous materials.

However, there are still many problems in the buildup factor of multilayer shields, especially in the parameterization of the data. Although many efforts[2-10] have been devoted to establish a better empirical function, empirical functions obtained so far succeeded in reproducing the multilayer buildup factors for only specific combinations of shield materials in an energy range that is not wide.

We proposed a new approximating model[11] for multilayer buildup factors. The model is formulated using transmission and albedo matrices with empirical corrections based on the vector form of 4 groups to explicitly treat energy spectrum information in the model. The model was tested by data in plane and point isotropic geometries for shields of 10-mfp(mean free path) thickness, and the observed maximum error of the approximation was about 10%.

In this work, we test the model by the point isotropic buildup factor data of much thicker shields of 40 mfp. Since the new technique was developed by Hirayama[12] to calculate the buildup factor of very thick shields by the EGS4, it is now possible to use the EGS4 calculation to test the present model for these thick shields.

2. Approximating Model and Applications

We use the vector form to express the energy spectrum of gamma rays, dividing the energy range from 0 to the source energy E_0 into 4 discrete groups.

A multilayered spherical shield of thickness x of N materials, i.e. n_1-mfp-thick materi-

als 1, n_2-mfp-thick material 2, and so on, is considered.(See Fig.1.) This shield is followed by an infinite medium of material N. A point isotropic gamma-ray source is located at the center of the shield.

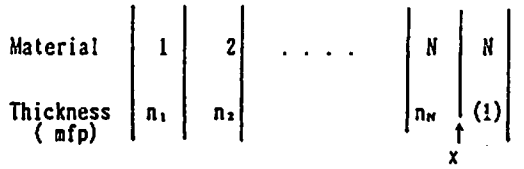

Figure 1 Material arrangement of multilayered shield.

The dose buildup factor B_D at the depth x is given by the expression (1):

$$B_D = \vec{C}(I + B_N)(\prod_{l=1}^{N} T_l^{n_l})\vec{S} \quad , \tag{7}$$

where $\vec{S}$ is a source intensity vector whose explicit expression is $\vec{S} = (1,0,0,0)$, T_l the transmission matrix of the material l, B_N the albedo matrix for the outside material N, I the unit matrix, and $\vec{C}$ the conversion vector from the energy fluence index to the dose index.

The materials assumed in the present test are water, iron and lead. And the buildup factor data calculated by the EGS4 at 0.1, 0.3, 0.6, 1, 3, 6 and 10 MeV are used as the reference data for the test of the present model.

We calculated the transmission matrix by the EGS4 code. A 1-mfp-radius sphere was used, assuming a source of unity intensity at its center. The estimated transmission matrix is multiplied by empirical factors to make corrections for not considering gamma-ray angular distributions, and to incorporate shell radius dependence of the transmission probability. The albedo calculation is also made by the EGS4 for a 1-mfp-thick shell with the inner radius of the 1-mfp length, where gamma rays were injected normally to the inner surface. Again empirical corrections are made to the estimated albedo matrix to incorporate the shell radius dependence.

We introduced 9 empirical parameters for the matrices of each material. These parameters are determined by the least-squares method at each energy so that the expression (1) may be simultaneously fitted to EGS4 calculated reference buildup factors of all single- and double-layered shields composed of materials considered. The material combinations of single- and double-layered shields considered are listed in Table 1. And the 1st and 2nd layer thicknesses assumed for each double-layered shield are showed in Table 2.

Table 1: Material Arrangement of Double-Lyered Shields

	1st Layer	2nd Layer
1	Water	Water
2	Iron	Iron
3	Lead	Lead
4	Water	Iron
5	Iron	Water
6	Iron	Lead
7	Lead	Iron
8	Water	Lead
9	Lead	Water

Table 2: Thickness of Double-Layered Shields

	Shield Thickness (mfp)		
	1st Layer	2nd Layer	Total
1	5	35	40
2	10	30	40
3	20	20	40

3. Results of Application

The gamma-ray linear attenuation coefficient shows generally different characteristics depending on the gamma-ray energy, which is typically classified into three regions, i.e., low, intermedaite and high energies. Correspondingly, the behavior of the buildup factor is different in the above three energy regions. The results of the application test of the present model is discussed for each of the energy ranges: low energy range (0.1 and 0.3 MeV), intermediate energy range (0.6, 1 and 3 MeV), and high energy range (6 and 10 MeV).

3.1. Intermediate Energy Range

The energy range from 0.5 MeV up to 3.5 MeV is the most important for the application of the point kernel method, where major gamma-ray sources are included. The Compton scattering dominates the gamma-ray reaction in this energy range, and the linear attenuation coefficient decreases with the gamma-ray energy.

Typical results of the present model of this energy range are showed in Fig.2 for the double-layered shields composed of water and iron at 1 MeV. The present model shows very good reproducibility of the buildup factor in this energy range.

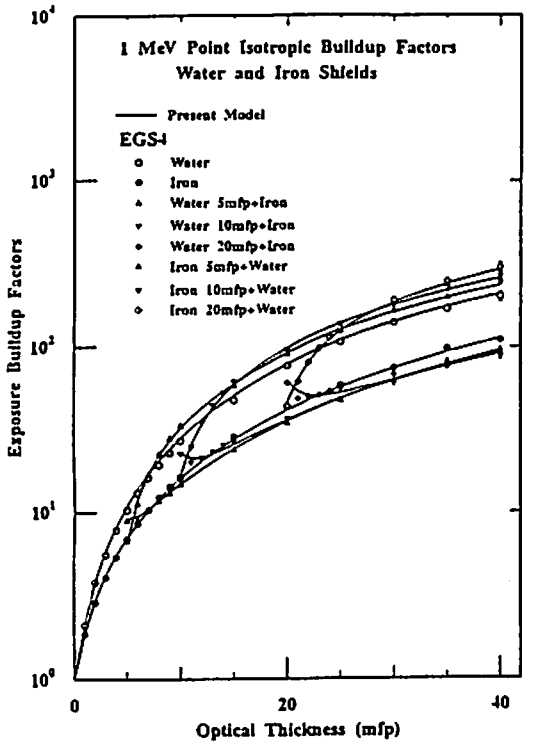

Figure 2 Point isotropic buildup factors at 1 MeV for single- and double-layered shields of iron and water.

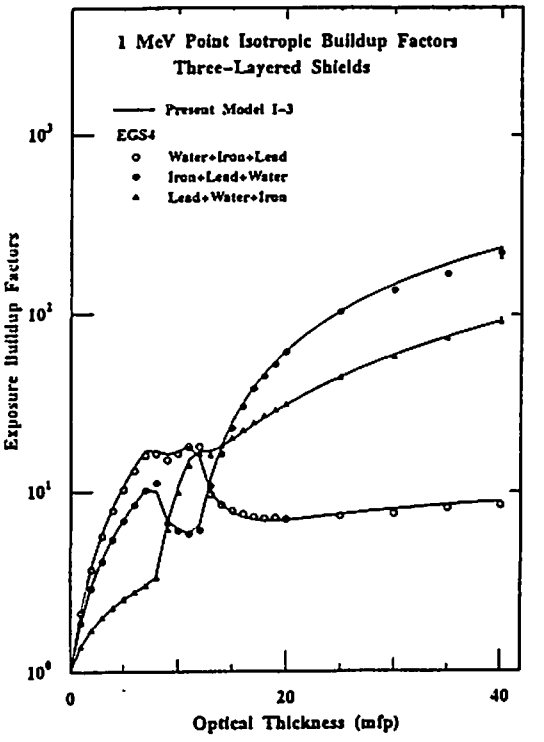

Figure 3 Point isotropic buildup factors at 1 MeV for three-layereds of water, iron and lead.

The buildup factors of three-layered shields are also very well reproduced by the present model as showed in Fig.3 with the empirical parameters determined for the double-layered shields. The error of the approximation of the model is within 15% in this energy range.

3.2. High Energy Range

In the high energy range, the linear attenuation coefficient of heavy materials like lead increases with gamma-ray energy. Therefore, photons at the Compton minimum energy have more probability of penetration through shields than those at the source energy. Moreover, the bremsstrahlung production cros section is fairy large in lead, which increases the number of photons near the Compton minimum energy. Consequently, the buildup factor in lead becomes very large at deep locations. Generally, the buildup factor

is larger in the order of the atomic number of the material.

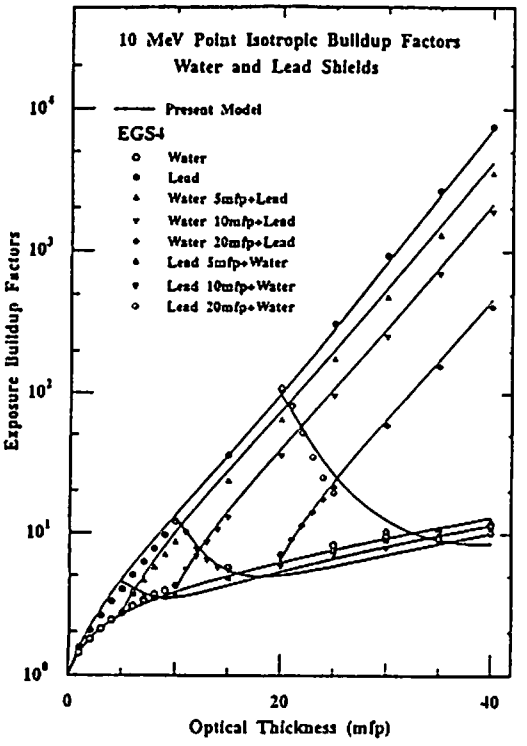

Figure 4 Point isotropic buildup factors at 10 MeV for single- and double-layered shields of water and lead.

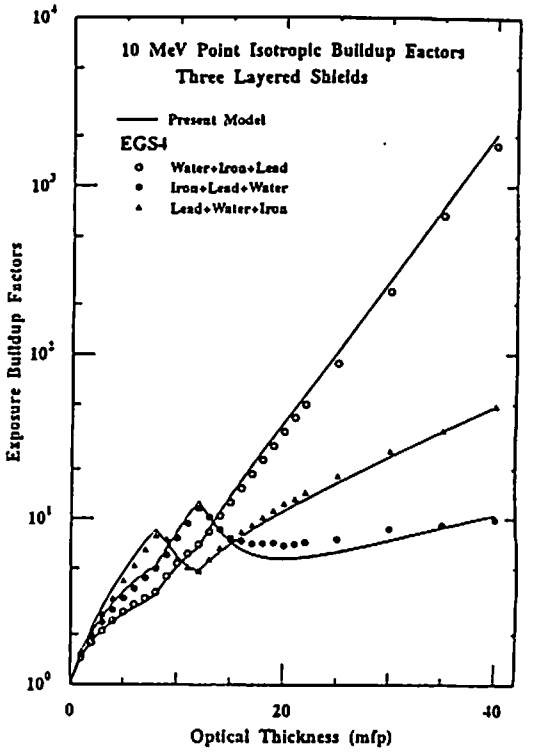

Figure 5 Point isotropic buildup factors at 10 MeV for three-layered shields of water, iron and lead.

An example of buildup factors at 10 MeV are showed in Fig.4 for the double-layered shields composed of water and lead. The above mentioned behavior of the lead buildup factor is quite well reproduced by the present model. However, the buildup factor in the water shield of double-layered shields of lead followed by watrer, is underestimated by about 30%, which is about twice as large as the corresponding one in the intermediate energy range. The quick spectrum change of gamma-rays from lead to water may not be very well reproduced by the present model due to the small number group approximation.

The buildup factors of the three-layered shields in Fig.5 are reproduced by the present model fairly well. Again, it is pointed out a similar underestimation of about 30% is made by the present model in the water shield.

3.3. Low Energy Range

In the low energy range, the absorption cross section is generally very large except for light materials. This causes hardening of the gamma-ray sepctrum in the shields, and almost no gamma rays exist in the 4th group. On the other hand, in the water shield, low energy gamma rays buildup in the 4th group very quickly, which results in large values

of buildup factor at deep locations. The behavior of the buildup factor differs very much, depending on the material. These extreme conditions causes a little bit larger error of the approximation of ~35% for the present model at 0.3 MeV.

For the 0.1 MeV source energy, the stepwise drop of absorption cross section at the K-edge and the production of K X-rays give rise a very steep increse in the buildup factor in the lead shield. This causes a relatively large error of about a factor of 3 for the present approximating model.

An example of the extreme behaviors of the buildup factor at 0.1 MeV is showed in Fig.6, for the double-layered shields composed of water and lead. The lead buildup factor becomes as much as 10^{11} at 40 mfp, while the buildup factor of water goes up to 10^4 at the same location. Generally, the buildup factors in these shields are quite well reproduced by the present model, although about a factor of 3 underestimation is seen at 40 mfp for the shield of 5-mfp water followed by lead.

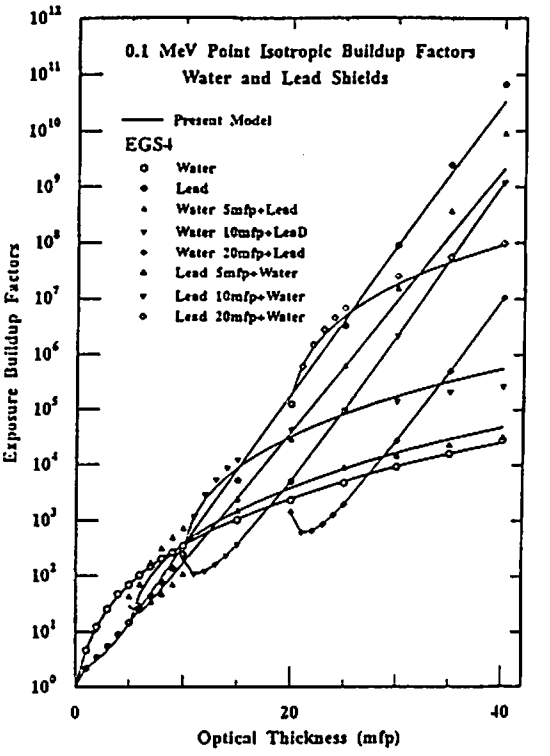

Figure 6 Point isotropic buildup factors at 0.1 MeV for single- and double-layered shields of water and lead.

4. Conclusion

Our approximating model of multilayer gamma-ray buildup factor was tested by the reference buildup factor data estimated by the EGS4 for the very thick shields up to 40 mfp.

As a conclusion of the tests, it is said that the present approximating model generally has a very good capability in reproducing the multilayer buildup factors even in the very thick shields. The observed error was within 15% in the intermediate energy range, about 30% in the higher energy range, and 35% at 0.3 MeV.

At the very small energy of 0.1 MeV, the error of the approximation reaches a factor of 3 in some cases. However, this error is acceptable as an approximating formula of the buildup factor, considering very large change of $\sim 10^{11}$ in the buildup factor.

References

[1] D. K. Trubey, *New Gamma-Ray Buildup Factor Data for Point Kernel Calculations; ANS-6.4.3 Standard Reference Data*, NUREG/CR-5740m U.S. Nuclear Regulation Commission(1991).

[2] M. F. Su and S. H. Jiang, *Gamma-Ray Buildup Factors for a Point Isotropic Source in Stratified Spherical Shields*, Nucl. Sci. Eng., **102**, 64 (1989).

[3] Y. Harima and H. Hirayama, *Detailed Behavior of Exposure Dose Buildup Factor in Stratified Shields for Plane-Normal and Point Isotropic Sources, Including the Effects of Bremsstrahlung and Fluorescent Radiation*, Nucl. Sci. Eng., **113**, 367(1993).

[4] M. Kitazume, *Some Considerations of Buildup Factors in Gamma Ray Penetration for Multilayers*, Nippon Genshiryoku Gakkaishi, **7**, 496(1965). (in Japanese)

[5] Y. Harima and Y. Nishiwaki, *An Approximate Transmission Dose Buildup Factor for Stratified Slabs*, J. Nucl. Sci. Technol., **6**, 711(1969).

[6] L. A. Bowman and D. K. Trubey, *Monte Carlo Calculation of Gamma-Ray Dose-Rate Buildup Factors for Lead and Water Shields and Monte Carlo Calculation of the Deposition of Gamma-Ray Heating in Stratified Lead and Water Slabs*, ORNL-2609, Oak Ridge National Laboratory (1958).

[7] M. H. Kalos, quoted in H. Goldstein, *Fundamental Aspect of Reactor Shielding*, p.225, Addison-Wesley Publishing Co. Inc., Reading, Massachusetts (1959).

[8] D. L. Broder, Yu. P. Kayurin and A. A. Kutrezov, Sov. At. Energy, **12**, 26(1962).(English Translation)

[9] H. Penkuhn, *A Parametric Representation of Gamma Ray Attenuation in Two-Layer Shields*, Nucl. Sci. Technol., *1*, 809(1979).

[10] Y. Harima, H. Hirayama, S. Tanaka and M. Sugiyama, *The Behavior of Gamma-Ray Buildup Factors in Stratified Shields, Proc. Topl. Mtg. New Horizons in Radiation Shielding, Pasco, Washington, April 26-May 1, 1992, P. 473, American Nuclear Society* (1992).

[11] K. Shin and H. Hirayama, *A New Approximating Model for Gamma-Ray Buildup Factors of Stratified Shields*, to be published in Nucl. Sci. Eng.(1994).

[12] H. Hirayama, private communication.

CALCULATION OF ABSORBED DOSE FOR SKYSHINE RADIATION FROM A 45MeV ELECTRON LINAC

M. HORI, N. NIIKAWA, M. KITAICHI, and S. SAWAMURA

Department of Nuclear Engineering, Hokkaido University
North 13, West 8, Kita-ku Sapporo, 060, Japan

I. NOJIRI

Power Reactor and Nuclear Fuel Development Corporation
Tokai-mura, Naka-gun, Ibaraki 319-11, Japan

Abstract

We calculated skyshine dose from a Hokkaido University 45MeV linear accelerator using the general purpose user's version of the EGS4 Monte Carlo Code. In the simulation we obtained values up to 700 meters from the linac. However, it has been clear from the results of the simulation that to accurately compare the calculated value with the measurement data, it is necessary to use the actual source spectrum of the leakage photon and the detailed modeling of the source.

1. Introduction

Dose evaluation for direct and scatterd radiation from nuclear fuel or other radiation facilities is carried out by using some shielding calculation codes. However, because of the lack of benchmark data for evaluation of these facilities, those calculations have to be performed very conservatively. The purpose of this study is to investigate and verify application of EGS4 Monte Carlo Code[1] to skyshine (the term is usually used to describe the gamma radiation emitted by sources on the ground and backscattered by the air) by comparing with the experimental data of skyshine dose obtained around a 45MeV linear accelerator installed at Hokkaido University.

To obtain skyshine benchmark data, we made the gated counting system using pulsed source[2], and we measured the leakage radiation from 45MeV linac.

We used the general purpose user's version of the EGS4[3] as the calculation code, and by using it we could easily simulate the model of the 45MeV linac and calculated the skyshin e dose rate due to the bremsstrahlung from the target and the target room.

2. Skyshine from 45MeV Linac

Figure 1 is the ground plan and the side view of the 45MeV linear accelerator which shows shielding condition of it. The accelerator room and the target room have 47 meters in total length, 6 meters in height, and about 6 meters in width. The target which produces bremsstrahlung is placed at 1.5 meters above the floor. These rooms is surrounded by concrete, and more soil is put in around these wall. By the ground-level in the vertical section, it sees that the accelerator is placed under the ground, and the air-duct is put in the target room which conducts to the stack.

From the previously gained experimental data, we have had the most intense dose rate around the stack[4], so photon leaks from the duct is considered as the skyshine source energy in this calculation.

3. Calculated Models and Methods

3.1 Energy Distribution Calculation of Photon in the Air-Duct

Figure 2 shows the simulation model by EGS4 of accelerator room in the 45MeV electron linac. A 45MeV electron source is put in the center of this model. The room is filled with air-gas and is surrounded by concrete walls. The electron source is a disc source (annular source with an inner radius of zero) with a radius of 0.25 cm, and target is a lead with a radius of 5 cm, a thickness of one radiation length. In this calculation, leakage of photon by bremsstrahlung emitted from a Pb target is considered. Because of shortening the time of calculation, photon transport only in a front half of the accelerator room is simulated.

The number of history of electron is 9,000,000 in this calculation. Table 1 shows the energy spectrum of skyshine source in the air-duct. It is necessary to calculate more actual spectrum in the duct in the future.

3.2 Skyshine Dose Rate Calculation

Skyshine source energy was determined by Table 1, and cross sectional view of calculated skyshine model around 45MeV linac is shown in Fig.3. As radiation field of photon, the region of air-gas is horizontally 700 meters, upwardly 1000 meters from the source. And the region of soil is downwardly 1 meter. The source is placed at 4.5 meters above ground and photon emission is directed upward into 17.6 degrees as a conical beam from the size of the air-duct and the target room. The vertical angle of this conical beam is

derived from the size and the position of the air-duct in the target room.

To calculate energy distribution of photons, annular surface crossing detectors around the source were put at 1 meter above ground. The photon flux was calculated and absorbed dose rate in air was derived from it.

The number of history is about 16,000,000 in skyshine dose rate calculation. The result is shown in Fig.4, where it is fitted by the curve which is the approximation of the flux intensity derived from the single scattering of photon in air (build-up factor is not multiplied). Figure 4 shows absorbed dose rate per linac pulse of 10^{-8} coulomb in air against the horizontal distance from the source. Table 2 compares the result of the calculation with experimental data[4]. Parameter μ is a total linear absorption coefficient in air.

4. Results and Analysis

1) Energy distribution of photon leaks from 45MeV linac is less than 600keV in Table 1 compared with 45MeV of primary electron beam energy to target. This distribution relatively agrees with past measurement data.

2) Compared the calculated values with fitted curve in Fig.4, it is thought that this calculation includes effects of multiple scattering of photons in air as to be far from the source. Less than 200 meters, the calculation agrees with the curve, and effects of multiple scattering see further than 400 meters.

3) Experimental value of μ was 0.0087m^{-1} on Table 2, which was corresponding to 115m in mean free path of a 600keV photon. However, calculated value was 0.018m^{-1} and 56m of a 100keV photon.

4) Above this, it is necessary to consider more actual source spectrum and the detailed modeling of the source to accurately compare the calculation with the experimental data.

Acknowledgment

We would like to thank to Dr. Y. Sakamoto in Japan Atomic Energy Research Institute for his useful discussion and Prof. H .Hirayama in National Laboratory for High Energy Physics for his kind help and advice.

References

[1] W.R.Nelson, H.Hirayama and D.W.O.Rogers, *The EGS4 Code System*, SLAC-Report-265(1985).

[2] Y.Ozawa, et al., *Nihon-Genshiryoku-Gakkai shi (J. At. E nergy. Soc. Japan)*, 5[3], 190(1963) [in Japanese].

[3] O.Narita, I.Nojiri and T.Momose, *The Development of a G eneral Purpose User's Version of the EGS4 Code System(II).*

[4] T.Sawamura, I.Murai, H.Tanida, K.Inoda and Y.Ozawa, *Nih on-Genshiryoku-Gakkai shi (J. At. Energy. Soc. Japan)*, **22**[10], 725sin732 (1980) [in Japanese].

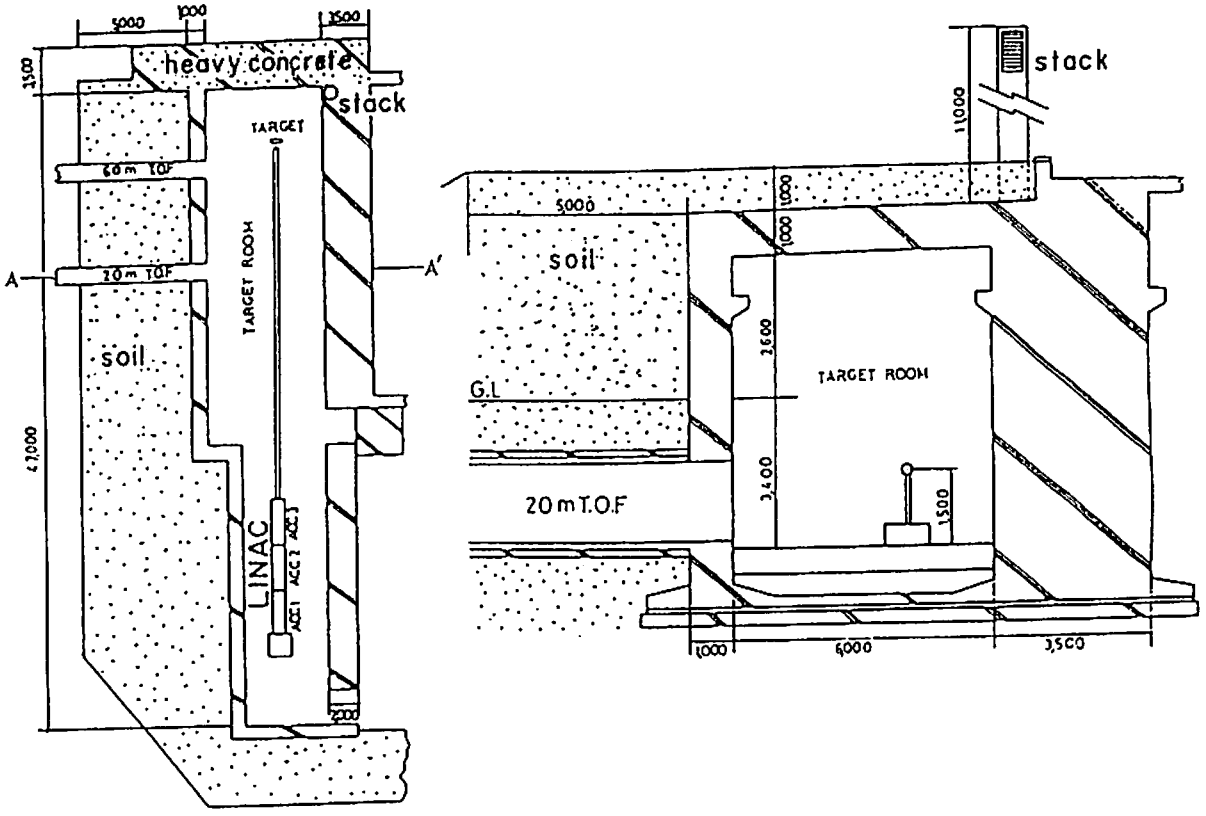

Fig.1 Grand Plan and Side View of Accelerator Room

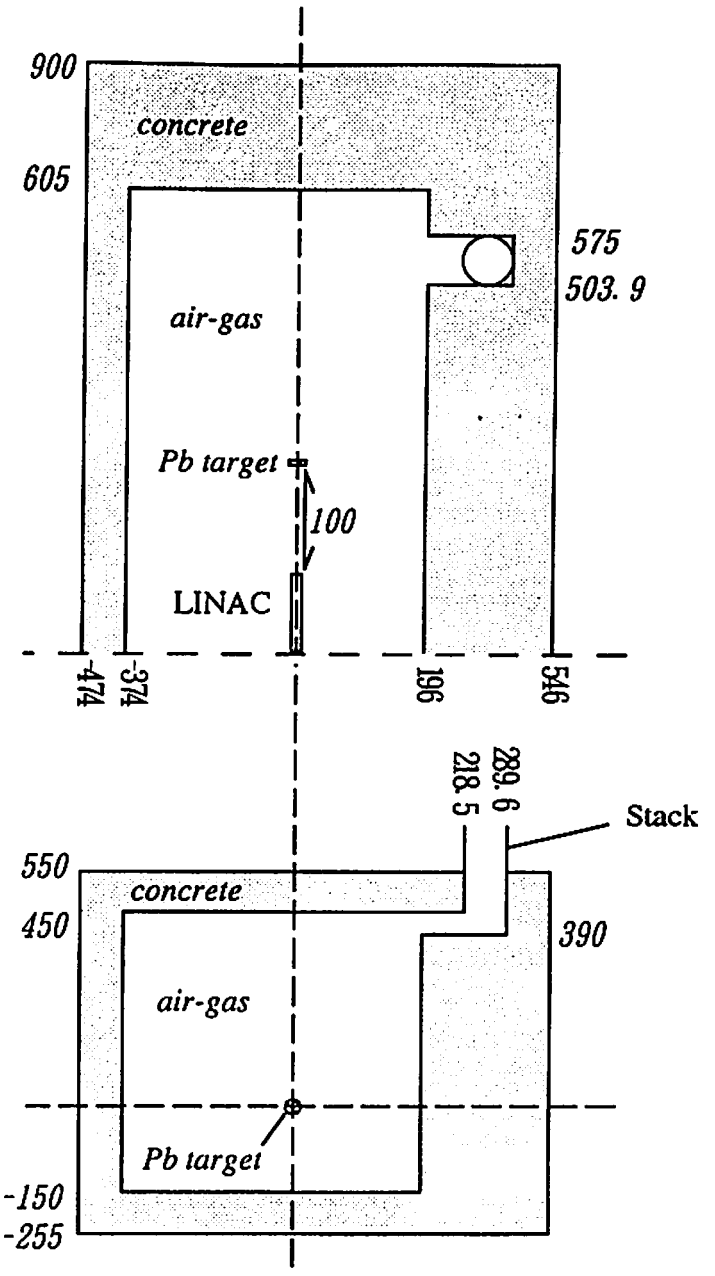

Fig.2 Calculation Model of the Accelerator Room (unit:cm)

Table 1 Skyshine Source Energy Spectrum

No	Energy (MeV)	Intensity
1	0.05~0.075	0.11
2	0.075~0.1	0.33
3	0.1~0.2	0.47
4	0.3~0.4	0.05
5	0.5~0.6	0.04

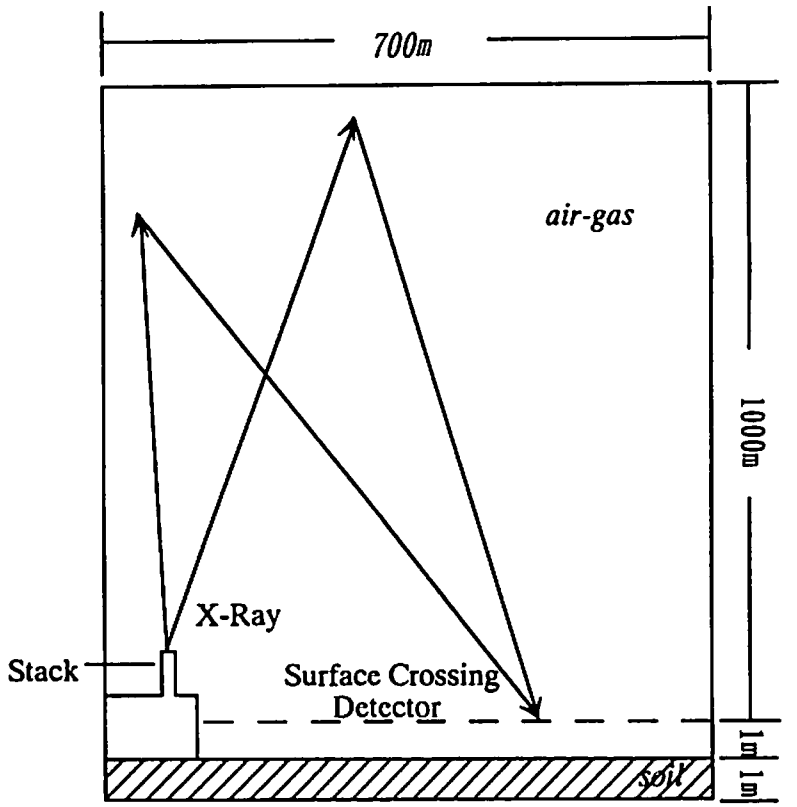

Fig.3 Calculation Model of Skyshine

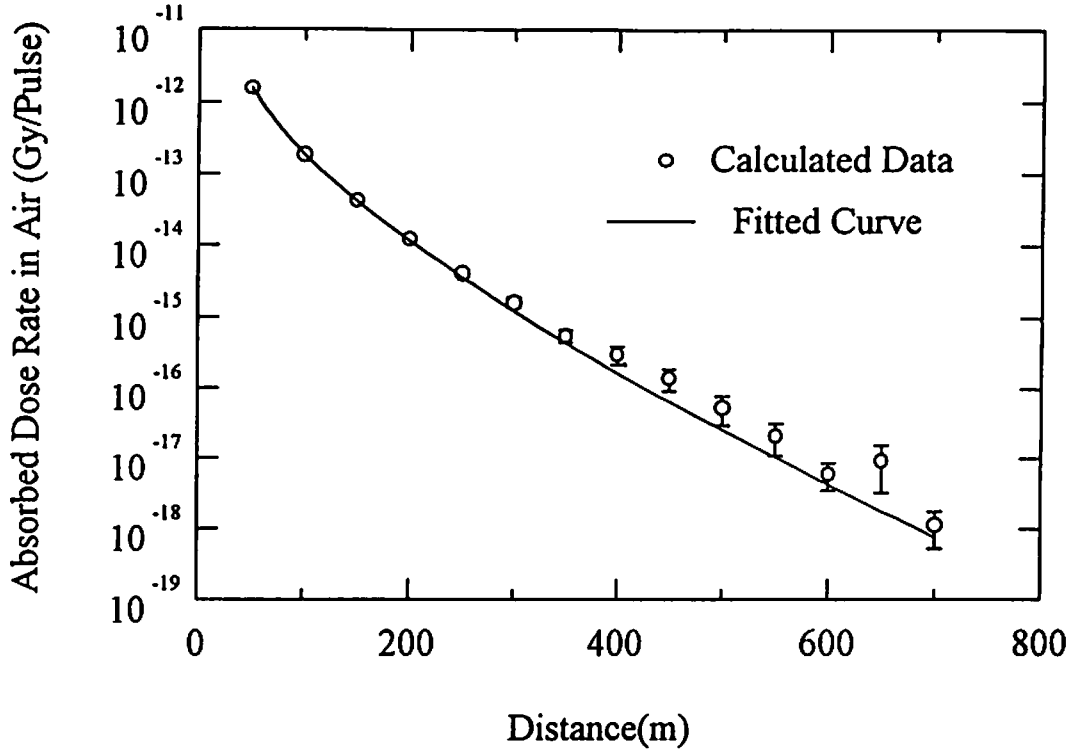

Fig.4 Absorbed Dose Rate for Skyshine

Table 2 Comparison between Experimentally Obtained and Calculated Parameter μ

	μ (m^{-1})
Experiment	0.0087
Calculation	0.018

CALCULATIONS OF BREMSSTRAHLUNG PHOTON SPECTRUM FROM BETA-RAY RADIOISOTOPE (II)

Y. SAKAMOTO, Y. NAKANE

Applied Radiation Laboratory,
Japan Atomic Energy Research Institute
Tokai-mura, Naka-gun, Ibaraki-ken, 319-11, Japan
and

S. TANAKA

Office of Planning,
Japan Atomic Energy Research Institute
Uchisaiwai-cho, 2-2-2, Chiyoda-ku, Tokyo, 100, Japan

1. Introduction

Electrons and positrons emitted from beta-ray radioisotope can be easily shielded by thin metals. In the case of beta-ray radioisotope with no emission of gamma-ray, we need to estimate the photon spectrum strength of bremsstrahlung emitted by the energy loss of beta-ray and evaluate the dose outside of shields. But it is not easy to estimate the photon spectrum of bremsstrahlung emitted from various targets.

There are calculation codes of bremsstrahlung photon spectrum such as BREMRAD[1] and BREMCALC[2] which are not available easily. Tanaka et al. introduced the new analytical formula for bremsstrahlung photon spectrum and evaluated the accuracy of the formula systematically by the comparison with EGS4 calculations[3,4]. Nakane et al. added the calculating function of the internal bremsstrahlung photon spectrum to BETABREM code which was based on the Tanaka's analytical formula, and revised the integration method to obtain the group-wise spectrum of bremsstrahlung photon[5].

In this paper, we compare the bremsstrahlung photon spectra obtained by BETABREM with those calculated by the NRCC version of EGS4 code and the ACCEPT code in ITS3 code system, and from ORIGEN2 data libraries.

2. BETABREM Code

In the BETABREM code, the photon intensity N(k) of bremsstrahlung from beta-ray

radioisotope in the thick target of atomic number Z with the photon energy between k and k+dk is approximately expressed as follows:

$$N(k) = \bar{T} \int_{T=k}^{T_0} \frac{TP(T)}{\int TP(T)dT} \frac{\omega(Z,T)}{1.25T} \left[4(1-\frac{k}{T}) + \frac{3k}{T} \ln \frac{k}{T}\right] \frac{1}{k} dk \tag{8}$$

where T and $\bar{T}$ are the kinetic energy of electrons and average energy of beta-ray, $P(T)$ is the energy distribution of beta-ray from allowed and unique first forbidden transition of which maximum energy is T0, is given by

$$P(T) = k_0 C(T) F(Z', W) pW(T_o - T)^2 \tag{9}$$

where $W, p, Z', C(T), F(Z', W)$ and k_0 are the total energy of beta-ray, the momentum of beta-ray, the atomic number of daughter isotope after beta-decay, the correction factor for transition, Fermi function and arbitrary constant, respectively. ω is the fraction from beta-ray to bremsstrahlung photon and is given by

$$\omega(Z,T) = \frac{aZT^b}{1+cZT^b} \tag{10}$$

where a, b and c are the constants given by the function of Z. BETABREM code calculate the external and internal bremsstrahlung photon spectrum in the point energies and the group structure energies.

3. Comparison of Bremsstrahlung Photon Spectra by BETABREM with Those by EGS4 and ACCEPT Code

The bremsstrahlung photon spectra from the point source of beta-ray radioisotope were compared with those by the NRCC version of EGS4 code[6] and ACCEPT in the ITS3 code system[7]. The electron cross sections used in EGS4 code were obtained by PEGS4 code with the options of IAPRIM=1, which denoted to use the data by Berger & Seltzer[8]. The cross section data of electrons in ACCEPT code were also same source data. In the calculations of bremsstrahlung photon spectra, the splitting technique of bremsstrahlung photon was used in two codes.

Figure 1 shows the bremsstrahlung photon spectrum of ^{90}Sr-^{90}Y source having 2.2 MeV maximum beta-ray energy surrounded by 0.05cm-thick lead target. Figures 2, 3 and 4 show the bremsstrahlung photon spectra of ^{85}Kr source with 0.687 MeV maximum energy surrounded by 0.042cm-thick titanium target, of ^{147}Pm source with 0.225 MeV maximum energy surrounded by 0.02cm-thick aluminum target and of ^{63}Ni source with 0.0659 MeV maximum energy surrounded by 1.7x10-4cm-thick gold target, respectively. The target radius is correspond to the CSDA (Continuous Slowing Down Approximation) range. In each figures, the point-wise spectra of external and internal bremsstrahlung photon, and

the group-wise spectrum of total bremsstrahlung photon by BETABREM with those calculated by EGS4 and ACCEPT codes. The calculated spectra by EGS4 and ACCEPT code are corresponding to the external bremsstrahlung photon. The bremsstrahlung photon spectra by BETABREM code are same degree or overestimated to those by EGS4 and ACCEPT codes with an exception of ^{63}Ni source surrounded 1.7x10-4cm-thick gold target.

4. Comparison of Bremsstrahlung Photon Spectra by BETABREM with ORIGEN2 Photon Data Library

ORIGEN2 photon data library[9,10,11] contains the 18-energy-group photon spectra including the effects of bremsstrahlung photon in uranium oxide and water medium with the original gamma-ray and X-ray data. Figure 5 shows the comparison of the bremsstrahlung photon spectra of 90Sr-90Y source surrounded by uranium oxide or water medium obtained by BETABREM code and ORIGEN2 data library. Figure 6 shows the ratio of bremsstrahlung photon spectra obtained by BETABREM code to ORIGEN2 photon data. The ratios of bremsstrahlung photon spectrum in the energy range from 0.8 MeV to 2 MeV are about 1.8 in the case of uranium oxide medium and about 1.2 in the case of water medium. Although photon spectra obtained by BETABREM are overestimated to those by ORIGEN2 data above 2 MeV energy, the absolute intensity is very small and the effect of overestimation to photon dose is negligible. Table 1 shows the ratios of bremsstrahlung photon spectra in the uranium oxide and water medium from beta-ray radioisotope incorporated in ORIGEN2 photon library, the values are same degree and the differences between two data are negligible in practical use. Bremsstrahlung photon spectrum data in ORIGEN2 are limited t_β two target materials of uranium oxide and water, and the number of the photon energy groups is fixed to 18. On the other hand, BETABREM can calculate the bremsstrahlung photon spectrum from desired target materials composed of the mixture of elements and for desired energy group structure.

5. Bremsstrahlung Photon Dose Outside the Shield

Bremsstrahlung photon dose outside the shield surrounding the point source of the beta-ray radioisotope was calculated by point kernel code QAD-CGGP212) with the source strength obtained by BETABREM and was compared with those which were obtained bremsstrahlung photon spectrum outside the shield by EGS4 and ACCEPT multiplied with dose conversion factors. Figures 7 and 8 show the attenuation of absorbed dose of air at 1 m from a point source of 90Sr-90Y isotope surrounded by aluminum and lead with thickness, respectively. Bremsstrahlung photon dose by BETABREM and QAD-CGGP2 is overestimated to the results of EGS4 and ACCEPT as a result of overestimation of

bremsstrahlung photon spectrum by BETABREM. The usage of buildup factors for infinite medium, which represent the multiplication of dose by scattered photons, is the another cause of overestimation in QAD-CGGP2. As the back scattering effect of photons by materials outside the evaluated point is remarkable in light elements such as aluminum, buildup factors for infinite medium is larger than those for finite medium. Maximum dose equivalent used by ANSI maximum dose conversion factors and ambient dose equivalents can be obtained in QAD-CGGP2 by absorbed dose of air multiplied with effective conversion factors from exposure dose to maximum dose equivalent and ambient dose equivalents. Attenuation behaviour of maximum dose equivalent and ambient dose equivalents is similar with absorbed dose of air.

We can also calculate the bremsstrahlung photon dose outside the shield from the spatially distributed beta-ray isotope in QAD-CGGP2 by the treatment of photon source as the assembly of point source.

6. BETASHIELD Code

We developed BETASHIELD code for the bremsstrahlung photon shielding calculation of beta-ray radioisotope by NEC personal computer coupled with BETABREM for estimation of bremsstrahlung photon spectrum and QAD-CGGP2 for dose attenuation calculation outside the shield. Data for the specification of beta-ray radioisotope, source strength, source spatial distribution, target materials surrounding beta-ray isotope and thickness of shield are inputted by dialogue type. The bremsstrahlung photon dose equivalents can be obtained at desired points. The distribution along the line and the contour map on the plane of bremsstrahlung photon dose can be also get. The display is represented by Japanese.

7. Conclusion and Future Work

BETABREM code was developed to calculate the bremsstrahlung photon spectrum of beta-ray radioisotope. The bremsstrahlung photon spectra by BETABREM were compared with those calculated by EGS4 and ACCEPT of ITS3, and the spectra are same degree or slightly large than those by two codes. As a result from comparison of spectra with those by ORIGEN2 photon data libraries, it was proved that BETABREM can calculate bremsstrahlung photon spectrum with same degree to ORIGEN2 data. BETABREM code have an advantage in the points of flexibility in the targets materials and photon energy structure.

Dose equivalents of bremsstrahlung photon outside shield obtained by BETABREM for the estimation of the photon source spectrum and by QAD-CGGP2 for shielding calculation are larger than those calculated by EGS4 and ACCEPT as a result of overesti-

mation of photon source spectra and usage of buildup factors for infinite medium. BETASHIELD code for personal computer was also developed to calculate dose equivalents of bremsstrahlung photon outside shield coupled with BETABREM and QAD-CGGP2.

BETABREM calculates bremsstrahlung photon spectrum of beta-ray isotope by the analytic formula for radiation yields and differential brems-strahlung photon spectrum, now. As ITS3 code system contains the differential photon spectrum data for bremsstrahlung, we will introduce differential photon spectrum data and stopping power data for electrons in EPSTAR library[13] to BETABREM.

References

[1] H. H. Van Tuyl, *BREMRAD - A Computer Code for External and Internal Bremsstrahlung Calculations*, HW-83784 (1964).

[2] P. D. Rittmann, *BREMCALC - A Computer Program for Calculating Electrons and Positron Bremsstrahlung*, ANS Topical Meeting, p.323 (1992).

[3] *Practical Manual of shielding calculations for radiation treatment facility, No.2*, Nuclear Safety Technical Center (1990), (In Japanese).

[4] S. Tanaka, *Calculations of Bremsstrahlung Photon Spectrum from Beta-ray Radioisotope*, Proceeding of the First EGS4 User's Meeting in Japan, KEK Proceedings 91-14, p.22 (1991) (In Japanese).

[5] Y. Nakane Y., et al., *Development of A Calculation Code BETABREM for Bremsstrahlung Spectrum from Beta-Ray Radioisotopes*, Proc. Annual Meet. of Atomic Energy Society of Japan in Nagoya Univ., K61 (1992), (In Japanese).

[6] W. R. Nelson, H. Hirayama and D. W. O. Rogers, *The EGS4 Code System*, SLAC-265 (1985).

[7] J. A. Halbleib, R. P. Kensek, T. A. Mehlhorn, G. D. Valdez, S. M. Seltzer and M. J. Berger, *ITS Version 3.0: The Integrated TIGER Series of Coupled Electron/photon Monte Carlo Transport Codes*, SAND91-1634 (1992).

[8] M. J. Berger and S. M. Seltzer, *Stopping Powers and Ranges of Electrons and Positrons (2nd Ed.)*, NBSIR 82-2550-A (1983).

[9] A. G. Croff, *ORIGEN2 - A Revised and Updated Version of The Oak Ridge Isotope Generation and Depletion Code*, ORNL-5621 (1980).

[10] A. G. Croff, *A User's Manual for The ORIGEN2 Computer Code*, ORNL/TM-7175(1980).

[11] A. G. Croff, R. L. Haese and N. B. Gove, *Updated Decay and Photon Libraries for The ORIGEN Code*, ORNL/TM-6055 (1979).

[12] Y. Sakamoto and S. Tanaka, *QAD-CGGP2 and G33-GP2: Revised Versions of QAD-CGGP and G33-GP (Codes with the COnversion Factors from Exposure to Ambient and Maximum Dose Equivalents)*, JAERI-M 90-110 (1990).

[13] NIST Standard Reference Data Base 7: *NIST Electron and Positron Stopping Powers of Materials Database Version 2.0*, National Institute of Standards and Technology (1989).

Table 1

Bremsstrahlung Photon Energy (MeV)

	0.0	0.02	0.03	0.045	0.07	0.1	0.15	0.3	0.45	0.7	1	1.5	2	2.5	3	4	6	8
Beta	①	②	③	④	⑤	⑥	⑦	⑧	⑨	⑩	⑪	⑫	⑬	⑭	⑮	⑯	⑰	
Isotope	0.01*2	0.025	0.0375	0.0575	0.085	0.125	0.225	0.375	0.575	0.85	1.25	1.75	2.25	2.75	3.50	5.0	7.0	
H 3	1.13*3																	
0.0186*1	1.79*4																	
C 14	0.90	0.72	0.92	0.56	0.72	0.83	0.78											
0.1565	0.96	0.80	1.06	0.67	0.93	1.13	0.91											
P 32	0.72	0.67	0.97	0.68	0.82	1.25	1.14	1.03	1.34	1.75	1.86	2.12						
1.711	0.61	0.57	0.81	0.56	0.67	1.01	0.91	0.81	0.99	1.22	1.22	1.27						
S 35	0.88	0.72	0.93	0.57	0.72	0.82	0.30											
0.1675	0.94	0.79	1.05	0.67	0.91	1.09	0.39											
Ca 45	0.93	0.81	1.10	0.72	0.89	1.18	0.78											
0.2659	0.93	0.82	1.13	0.76	0.99	1.35	0.92											
Ni 63	0.85	0.57	0.61	0.24														
0.0659	1.08	0.77	0.87	0.36														
Kr 85	0.84	0.78	1.12	0.77	0.94	1.37	1.13	0.88	1.04									
0.687	0.74	0.68	0.97	0.67	0.82	1.20	0.99	0.78	0.91									
Sr 90	0.87	0.80	1.13	0.79	0.94	1.35	1.04	0.68	0.94									
0.546	0.78	0.72	1.02	0.70	0.85	1.23	0.97	0.64	0.73									
Y 90	0.66	0.62	0.89	0.62	0.75	1.14	1.07	0.98	1.26	1.66	1.81	1.79	77.3					
2.279	0.57	0.52	0.75	0.52	0.62	0.93	0.86	0.77	0.95	1.20	1.25	1.15	45.8					
Rh106	0.59	0.55	0.79	0.55	0.66	1.00	0.95	0.86	1.11	1.42	1.56	1.41	1.83	1.23	0.45			
3.54	0.52	0.47	0.68	0.47	0.56	0.84	0.78	0.69	0.96	1.08	1.21	1.00	1.29	0.89	0.31			
Pm147	0.84	0.75	0.99	0.63	0.77	0.81	0.48											
0.2247	0.90	0.78	1.06	0.69	0.89	1.13	0.60											
Bi210	0.79	0.74	1.06	0.74	0.90	1.33	1.18	1.04	1.36	1.85	2.48							
1.161	0.68	0.63	0.90	0.62	0.75	1.11	0.96	0.83	1.01	1.25	1.44							

*1:Maximum energy of beta-ray, *2:Average photon energy in a group

*3,*4:Ratios of bremsstarhlung photon spectra by BETABREM to those by ORIGEN2 data in an uranium oxide and a water target.

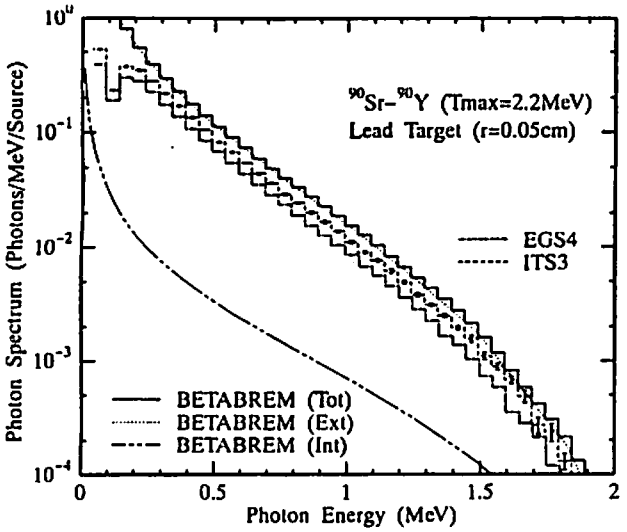

Fig.1 Bremsstrahlung photon spectrum from ^{90}Sr-^{90}Y in a lead target

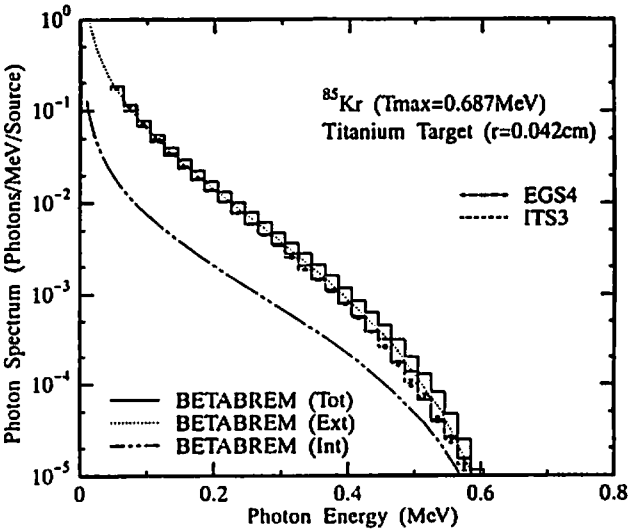

Fig.2 Bremsstrahlung photon spectrum from ^{85}Kr in a lead target

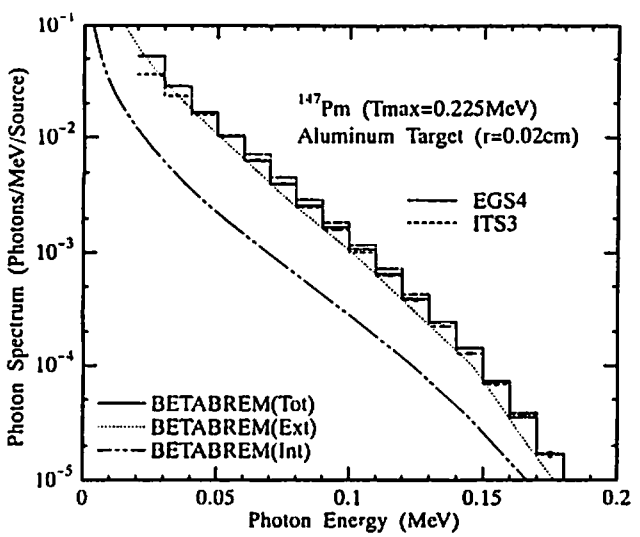

Fig.3 Bremsstrahlung photon spectrum from ^{147}Pm in an aluminum target

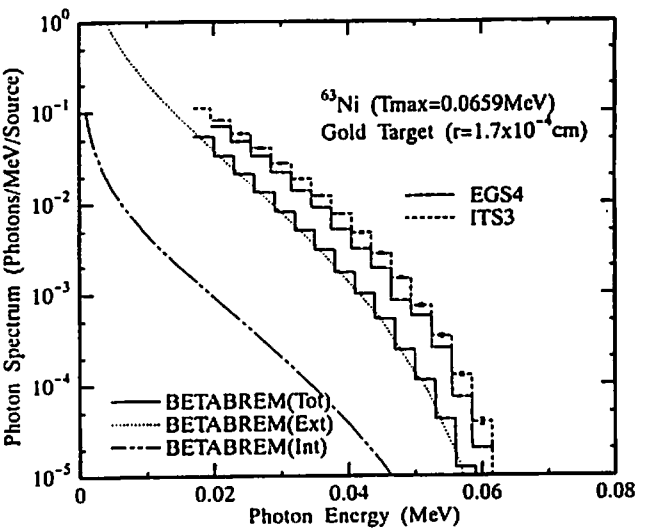

Fig.4 Bremsstrahlung photon spectrum ^{63}Ni in agold target

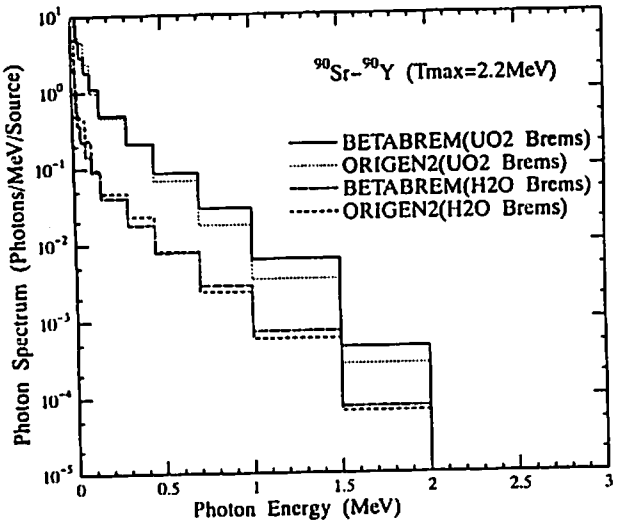

Fig.5 Bremsstrahlung photon spectrum from ^{90}Sr-^{90}Y in a uranium oxide and a water target

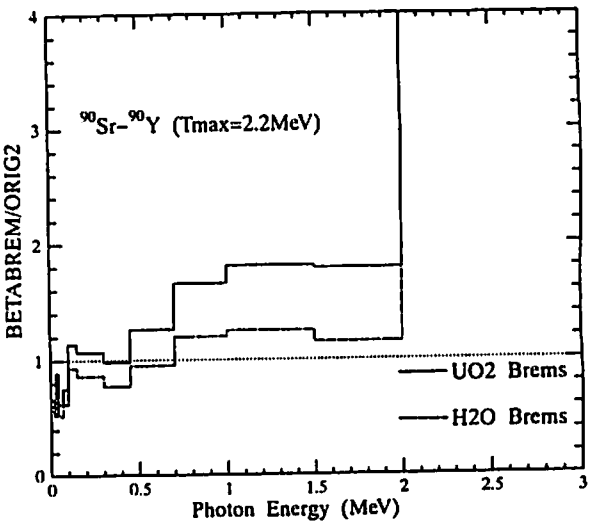

Fig.6 Ratios of bremsstrahlung pho spectrum from ^{90}YSr-^{90}Y in an uraniumn oxide and a water target by BETABREM and ORIGEN2

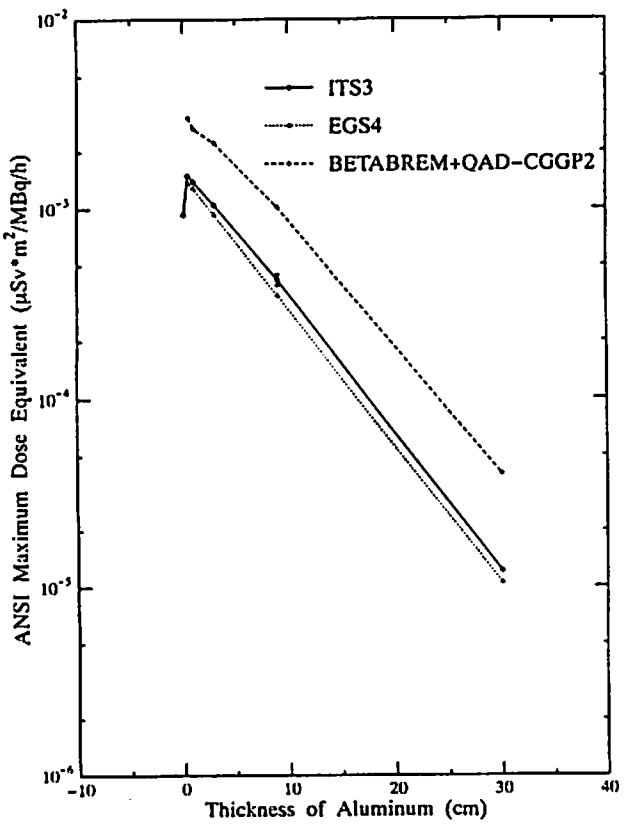

Fig.7 Absorbed dose of air from bremsstrahlung photon from ^{90}Sr-^{90}Y in an aluminum target

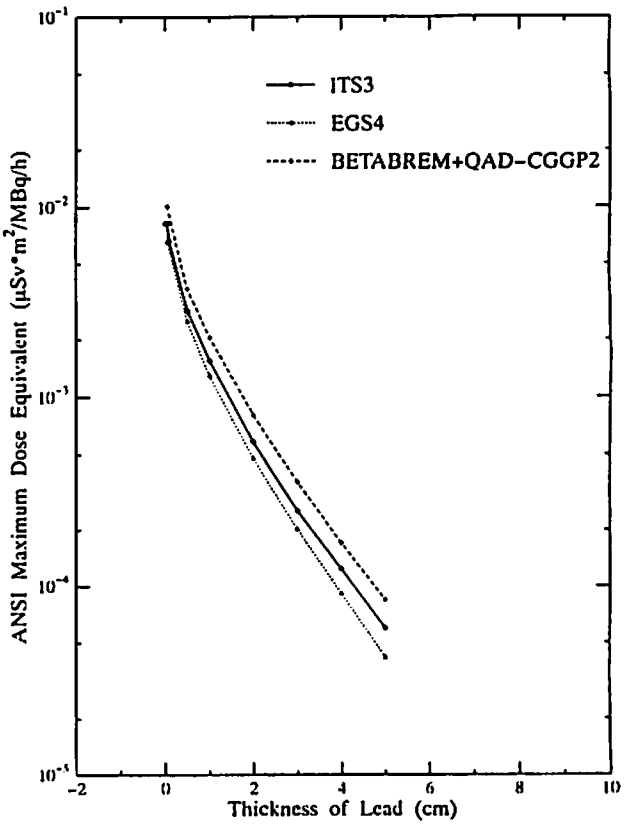

Fig.8 Absorbed dose of air from bremsstrahlung photon from ^{90}Sr-^{90}Y in a lead target